Dissertation

submitted to the

Combined Faculty of Natural Sciences and Mathematics

of Heidelberg University, Germany

for the degree of

Doctor of Natural Sciences

Put forward by

M.Sc. Marcel Haas

born in: Mannheim

Oral examination: 24 May 2023

Non-linear Dynamics of Two-Level Systems in Non-equilibrium

Referees: Prof. Dr. Christian Enss
Prof. Dr. Heinz Horner

Non-linear Dynamics of Two-Level Systems in Non-equilibrium

The dielectric loss of amorphous materials along with noise and decoherence are the major limiting factors for many applications at low temperatures like superconducting circuits, Josephson junctions and quantum computing. These effects are nowadays understood as the consequence of an ensemble of quantum mechanical two-level systems (TLSs), which are described as additional broadly distributed low-energy excitations in the sample. In this context, the thesis at hand presents a unique property of an amorphous material when two pump-tones are applied. In this limit the utilized LC-resonator is emitting at the intermediate frequency of the two off-resonant driving fields. The underlying mechanism can be explained by a non-linear interaction of the rf-field with the TLSs and the resonator, which creates additional lines in the frequency spectrum and thereby a self-biasing effect. The corresponding measurements also define a specific set of parameters for the occurrence of this emission limit, which is well described by a phenomenological approach in the context of the Landau-Zener-Stückelberg formalism. The obtained results thus complement the bigger picture of TLSs and open up a new approach for further investigations.

Nichtlineare Dynamik von Zwei-Niveau-Systemen im Nichtgleichgewicht

Der dielektrische Verlust von amorphen Materialien ist zusammen mit Rauschen und Dekohärenz einer der größten limitierenden Faktoren für viele Tieftemperaturanwendungen wie supraleitenden Schaltungen, Josephson-Kontakte und Quantencomputing. Diese Effekte sind heutzutage erklärbar als das Resultat eines Ensembles von quantenmechanischen Zwei-Niveau-Systemen, die als zusätzliche und breitverteilte Niedrigenergieanregungen beschreibbar sind. In diesem Kontext stellt die vorliegende Arbeit eine einzigartige Eigenschaft eines amorphen Materials vor, die auftritt, wenn an dieses zwei Pumptöne angelegt werden. In diesem Limit emittiert der verwendete LC-Resonator auf der Mittelfrequenz der zwei Felder. Der zugrundeliegende Mechanismus kann durch eine nichtlineare Wechselwirkung des Hochfrequenzfeldes mit den Zwei-Niveau-Systemen und dem Resonator erklärt werden, was zusätliche Linien im Frequenzspektrum bildet und somit zu einem Selbst-Bias Effekt führt. Die entsprechenden Messungen zeigen außerdem, dass das Emissionslimit in einem bestimmten Systemparameterraum auftrit, welcher gut mit einem phänomenologischen Ansatz im Kontext des Landau-Zener-Stückelberg Formalismus beschrieben werden konnte. Die Ergebnisse ergänzen somit die Erkenntnisse von Zwei-Niveau-Systemen und eröffnen einen neuen Ansatz für weitere Untersuchungen.

Contents

1. Introduction

The presence or absence of order in many-particle systems significantly determines the observed physical properties of the corresponding material because of its direct connection to the symmetry of the system. The distinction between crystalline and amorphous structures therefore follows naturally from the missing long-range order of the latter. Crystals are thus by definition highly ordered systems with a lattice structure on the basis of a unit cell, whereas amorphous materials only posses a short-range order and lack a periodic arrangement of their constituents. The emergence of disorder, however, also correlates with the occurrence of additional *two-level systems* (TLSs), which play a significant role for the material properties, in particular at low temperatures.

This discrepancy between a crystalline structure and its amorphous counterpart was observed for the first time by Zeller and Pohl [Zel71]. Their measurements showed an anomalous behaviour for the thermal properties of a quartz glass at low temperatures, which could not be explained by the Debye model [Deb12] as for the case of crystalline quartz. Measurements in the following years confirmed these findings also for other amorphous samples and the observed effects could be understood by the presence of additional low-energy excitations in these materials. A phenomenological model, which was proposed by Anderson *et al.* [And72] and simultaneously by Phillips [Phi72], assumed these systems as a particle in a double-well potential. For low temperatures the energy barrier between the individual wells can thereby only be overcome by quantum mechanical tunneling, which is why this formalism is generally referred to as the *standard tunneling model* (STM). It has proven to be a successful tool to describe the low temperature properties of many amorphous samples by the impact of these intrinsic systems. Measurements in subsequent years on further samples, however, showed more and more deviations from the predictions of the STM and hence required several extensions to the model. These extension consist of different approaches to include, for example, a change in the underlying distribution function [Dou80, Ens89] or the interactions between individual tunneling systems [Bla77, Bur95, Ens97]. Further measurements also revealed a significant dependency of the dielectric function [Str98, Woh01] and the polarisation echo amplitude [Lud02, Lud03] on magnetic field excitations. This effect could be attributed to constituents carrying a nuclear electric quadrupole moment, which modifies the behaviour of the associated TLS [Wür02, Nag04, Baz08, Bar13]. In recent years TLSs were also identified as the main source of noise [Gao07, Nei13, Bur14b, Pal14] and decoherence [Mar05, Ku05, Mül19] in superconducting quantum devices. Due to their appearance in metal oxide films, in isolation layer materials or as defects

[Lis19], they are almost unavoidable in modern day micro-electronic fabrication. This shed new light on the investigation, especially for the interaction of individual systems with each other [Lis15] or with the micro-electronic setup [Sar16, Bre17]. Experiments on superconducting high-quality LC-resonators with additionally applied bias fields furthermore allowed to control the dielectric loss of the sample material [Kha14, Ros16, Mat19, Fre21] and for the case of [Ros16] even produce a gain.
This thesis ties in with these measurements and presents the investigation of a thin film amorphous material by means of a superconducting LC-resonator with a bridge-type capacitor design. This geometry is well established and provides an additional electronic branch, which is separated from the readout chain of the resonator and is therefore suitable for bias or pump signals. Of particular interest thereby is the response of the TLS-ensemble to the application of two pump-tones. With regard to other measurements on quantum devices, it would be favourable to reduce the TLS-loss contribution as much as possible or even use their properties to enhance the corresponding quantity. Having said this, the investigated device shows a limit under certain conditions, in which the resonator emits a peak with a narrow bandwidth at resonance frequency. These observations raised the need to study the non-linear behaviour of the system in more detail and to characterise the observed limit. The final goal would thereby be a theoretical description of the occurring effect to further understand the behaviour of the TLSs in amorphous materials.

This thesis is structured as follows: Chapter 2 presents an overview of the fundamental theory necessary to understand the physical context. It begins with a general introduction of amorphous structures and their low temperature properties, followed by a section dedicated to explain all relevant properties of two-level systems. Subsequently, different mechanisms for relaxation are discussed, which are necessary to derive relations for the entire system. Afterwards, a short section is devoted to the effect of stimulated emission in disordered media and the chapter closes with the treatment of different resonator types under multiple field excitations. The 3rd chapter shows the employed experimental setup from the micro-structured resonator over the measurement electronics to the creation of temperatures in the millikelvin regime. Chapter 4 presents the experimental results and starts with some standard measurements to characterise the sample. These sections are followed by various pump-tone measurements and the characterisation of the non-linear behaviour of the resonator. The last section is dedicated to evaluate and describe the observed emission limit. In the end, the thesis closes with a summary in chapter 5 of the obtained results.

2. Theoretical background

This chapter presents the theoretical foundation to understand the utilized physical concepts for the evaluation of the experimental and simulated results in this thesis. The subsequent first section gives a short introduction to the structure of amorphous materials followed by the description of their thermal properties in section 2.2. The theory to explain the low temperature properties of these substances is introduced in section 2.3 with the *standard tunneling model*. It continues with the description of the therein defined tunneling systems and their behaviour under external electric field excitations. The next section 2.4 introduces relaxation time scales for the intrinsic systems, followed by section 2.5, which derives relations to describe the properties of the entire ensemble. Section 2.7 introduces the idea of stimulated emission effects on disordered media and afterwards the chapter closes with the discussion of different types of resonators.

2.1 Structure of amorphous materials

The very basic definition of an amorphous material is that of a solid without long range order. This criteria distinguishes these compounds from the highly ordered material class of crystals. The term *amorphous material* was in the past often used synonymously with *glass* and partially still is, but other structures exist that fulfil the conditions for example amorphous polymers.
A glass is manufactured from a rapidly cooled liquid melt of the raw materials. The cooling rate is thereby crucial for the formation of the microscopic structure. If the melt is cooled below the melting point very slowly, the system can form the thermodynamically favoured crystalline state by nucleation and crystallisation. This occurs via a first order phase transition. For faster cooling rates, on the other hand, atoms have no time to arrange and thus solidify in a highly disordered structure. Amorphous materials are also often referenced as "frozen liquids" or "super-cooled liquids", partly because first x-ray diffraction experiments showed similar results to measurements on liquid samples. These terms can, however, be misleading, since amorphous materials exhibit with an infinite viscosity and rigidity the properties of a normal solid. Typical areas for applications are nowadays diverse, from glass as a construction material, as an additive in cosmetic, food or pharmaceutical industry to the utilisation for microelectronics as an isolation or dielectric layer. Amorphous silicon dioxide (SiO_2) thereby belongs to a large group of silicate glasses and is used in the following sections as a basic example to explain the fundamental properties of these materials.

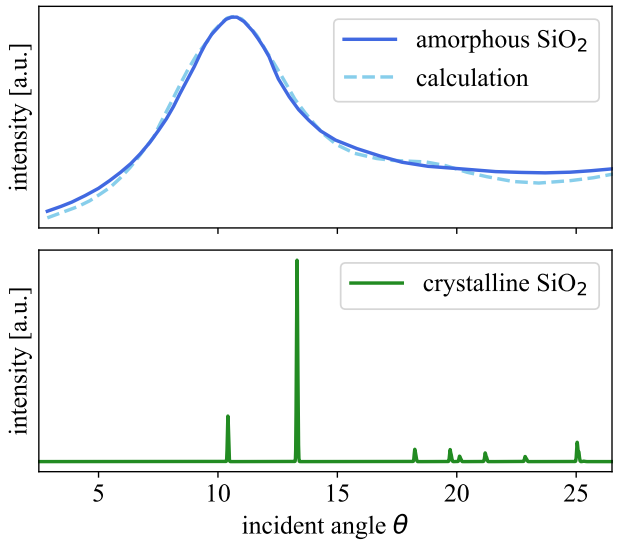

Figure 2.1: X-ray diffraction measurement of amorphous (**top**) and crystalline (**bottom**) SiO_2 in dependence of the incident angle θ. While the crystal shows distinct peaks, the diffraction pattern of the amorphous sample is broadly distributed. The data is adapted from [War34] for the amorphous material and from [Laf15][1] for the crystalline.

As already mentioned, x-ray diffraction measurements of an amorphous material showed a broad distribution of the intensity over the incident angle θ. In figure 2.1 an exemplary measurement of amorphous SiO_2 by Warren [War34] is compared to the results obtained from the crystalline counterpart [Laf15][1]. Although both samples contain the same nuclear components, the measurements differ significantly from one another. The theoretical description of the intensities of the amorphous SiO_2 utilized the same method as for the diffraction in liquids [Zer27]. The atoms are thereby allowed to occupy all available orientations for the calculation of the scattering amplitude. This description showed good agreement with the obtained data and led to the conclusion that the atomic constituents form a random network. Silicon atoms, which are tetrahedrally surrounded by four oxygen atoms, serve as the building blocks of this structure [War33]. The corresponding average atomic distance for the silicon-oxygen bond can thereby be calculated to 1.60 Å [War34]. In the crystalline counterpart the tetrahedrons are arranged in a regular lattice and fulfil the condition for diffraction only for discrete incident angles. The corresponding measurement shows vanishing intensities apart from the expected reflexes indicating a highly ordered underlying structure.
The ideas to interpret this data partly originate from the considerations of Zachariasen [Zac32], which is why this concept is sometimes referred to as the Zachariasen-Warren network hypothesis. In his work he compared the energy content of a glass structure with that of the corresponding crystal network. Since the potential energies are comparable, he concluded that both materials are structured by the same polyhedral components. The amorphous network is arranged in random orientations and hence misses the periodicity and symmetry, which are essential for the crystal

[1] x-ray powder diffraction data from W.W. Pinch. RRUFF ID:R100134

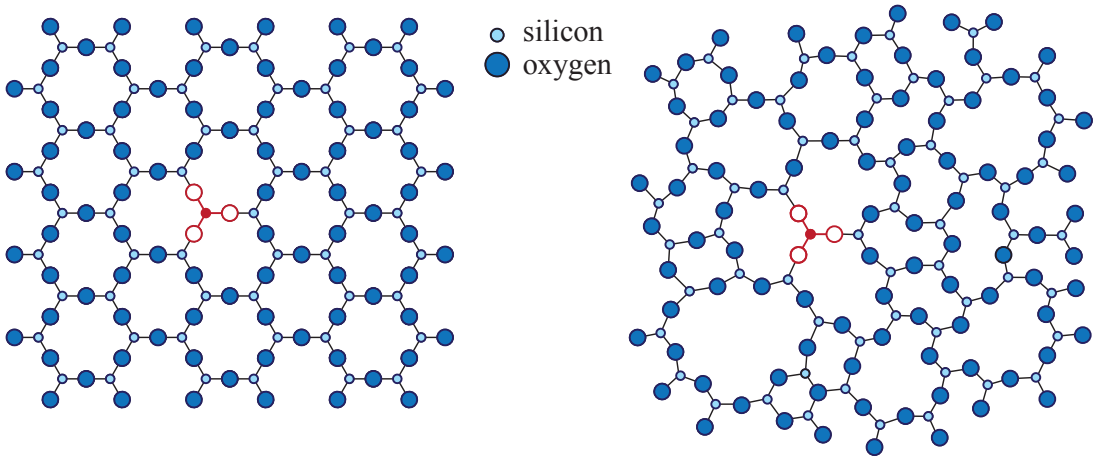

Figure 2.2: Schematic illustration of crystalline (**left**) and amorphous (**right**) structure. The picture is inspired by [Zac32] and shows a simplified two-dimensional representation of the complex structure.

lattice. The resulting isotropy is accompanied by the absence of a long-range order in the amorphous material. Correspondingly the binding angles and binding lengths are broadly distributed over the parameter space. A schematic illustration of the crystalline and the amorphous structure of SiO_2 is depicted in figure 2.2 as a simplified two-dimensional representation. For the real structure every silicon atom is additionally connected to a fourth oxygen atom, which is either in- or out-of-plane in this schematic. The left illustration in figure 2.2 shows the periodicity and the symmetry of the crystalline structure with the tetrahedral building block (red). The picture on the right hand side represents the amorphous solid with its highly disordered structure, but with the same atomic components. Both illustrations should provide a general understanding on the structural difference for this simple example, however, the actual composition is often much more complex and depends strongly on the manufacturing process.

The random network hypothesis was confirmed for two-dimensional systems by the investigation of vitreous and crystalline SiO_2 thin films through noncontact atomic force microscopy and scanning tunneling microscopy [Lic12]. The samples were prepared on a Ru(0001) single crystal, but similar results were found for SiO_2 on a graphene support by scanning transmission electron microscopy [Hua12]. The results show astonishing agreements with the illustration of Zachariasen from figure 2.2. The scanning tunneling microscopy measurement of an interface from the crystalline to the amorphous phase [Fre17] is depicted on the left in figure 2.3. The picture on the right shows a visualisation of the obtained data with colourized atoms for silicon (red) and oxygen (green). The crystalline phase shows the expected periodicity and symmetry with exclusively hexagonal surfaces (magenta). Deeper in the

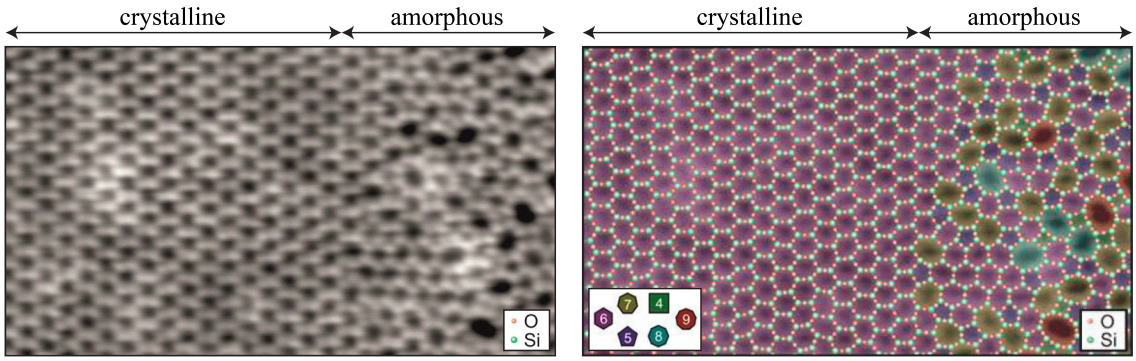

Figure 2.3: Interface from the crystalline to the amorphous structure. **Left**: scanning tunneling microscope picture of a silica thin film on a Ru(0001) single crystal surface. **Right**: visualisation of the analysed structure with colour coded polygons for different ring sizes. Adapted from [Fre17].

section of the amorphous phase pentagonal (yellow) and heptagonal (purple) surfaces start to form, until all kinds of polygonal shapes arise in the vitreous structure. Similar measurements have been conducted for other two-dimensional systems on surface layers of ice [Mai16] and copper oxide [Yan11].
Most glasses usually consist of more than a single oxide component. The different building blocks are grouped by their network developing properties into three categories. Some compounds weaken the amorphous network when inserted in the structure. Instead of covalent bonds, they develop ionic bonds to the negatively charged oxygen atoms. Glass containing these compounds usually exhibits a reduced melting point and a higher electric conductivity, which can be attributed to the weakened bonding and the therefore increased mobility of the constituents. They are classified as network modifiers and have mostly coordinate numbers of six or higher. Network formers, like SiO_2, lead to the emergence of an amorphous network and have usually coordinate numbers of three or four. Some compounds can act as either network modifiers or as network formers and are therefore defined as intermediate oxides. They normally carry coordinate numbers from four to six. This description is known as the network theory, which has many additions and extensions. A detailed discussion of this topic can be found in [Vog92].

2.2 Low temperature properties of glasses

This section discusses the consequence of the above described structural differences, which are not only relevant for the microscopic understanding of amorphous materials. Moreover, order and disorder are fundamental properties of a many-body system and heavily influence the observed macroscopic quantities. The first measurements, which revealed clear deviations from the crystalline behaviour and led to an independent phenomenological description for amorphous materials, are therefore presented in this section. It starts with the temperature dependent experiments conducted on the specific heat and the thermal conductivity, followed by the observations for saturation and absorption experiments.

2.2.1 Specific heat capacity and thermal conductivity

A crystalline material is well described by the definition of a unit cell due to its periodic structure. The arising long-range order allows the quantisation of the vibrational excitations in the crystal lattice as phonon modes. The derived phononic density of states forms the basis for the Debye model proposed in 1912 [Deb12], which predicts the low temperature properties of insulating crystalline solids very well. The specific heat capacity C_v is thereby expected to follow a cubic temperature dependence. Amorphous materials on the other hand lack the necessary long-range order to use the same formalism. The definition of phonons would only be sensible for larger wavelengths, for which the underlying disordered structure can be approximated as a continuum. Amorphous materials were therefore expected to follow the Debye model only for very low temperatures.
The measurements of Zeller and Pohl [Zel71] in 1971 showed, however, that these considerations could not describe the observed behaviour. Their results contained comparative measurements for the specific heat capacity and the thermal conductivity of amorphous and crystalline quartz (SiO_2), which are shown on the left and right hand side of figure 2.4 with complementary data from [Las75]. While the crystalline sample follows the T^3-dependency predicted by the Debye model, the specific heat of the amorphous material is orders of magnitude higher and is better described below $\sim$0.5 K using a $T^{1.3}$-dependency. In contrast to that, the thermal conductivity κ of vitreous quartz is orders of magnitude smaller than for its crystalline counterpart. Due to the definition of the thermal conductivity in the low temperature limit

$$\kappa = \frac{1}{3} C_\mathrm{v} v l, \tag{2.1}$$

the quartz crystal follows a T^3-dependency. Here v describes the Debye sound velocity and l the mean free path of the phonons, which can be approximated by a

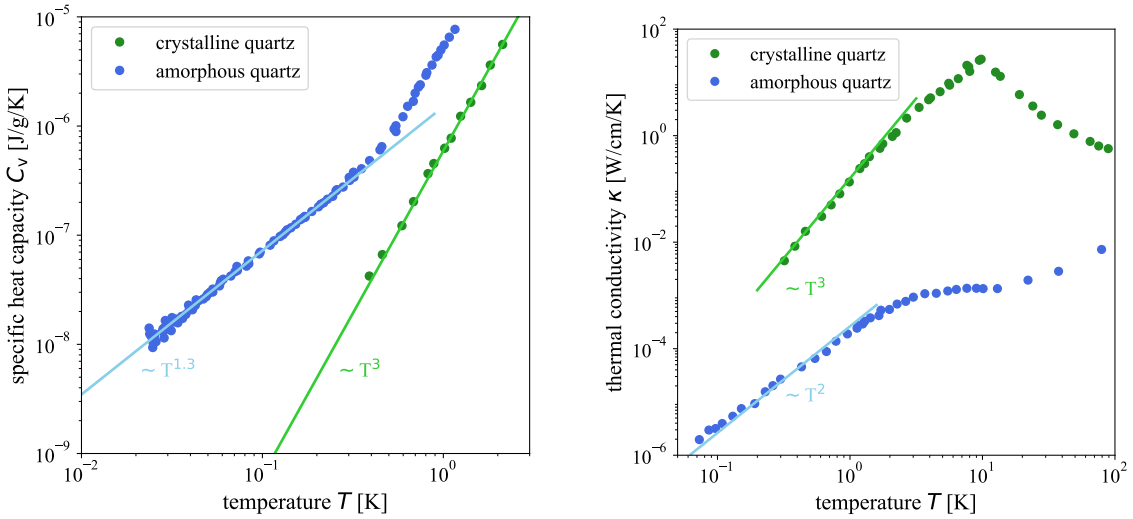

Figure 2.4: Measurements of Zeller and Pohl [Zel71] with complementary data from Lasjaunias *et al.* [Las75]. **Left:** specific heat capacity C_v of amorphous and crystalline quartz. Below ∼0.5 K the amorphous material follows a $T^{1.3}$-dependency instead of the predicted T^3-dependency as shown by the crystalline sample. **Right:** thermal conductivity κ of amorphous and crystalline quartz. The glass is approximated with a T^2-dependency, while the crystalline counterpart can be described by the low temperature limit given by the Debye model.

constant in the order of the sample size (Casimir regime). For the amorphous quartz, a T^2-dependency can be found in this temperature regime. The measurements indicates the existence of additional low energy excitations arising from the amorphous structure. Such systems act as scattering sites for phonons and therefore decrease the thermal conductivity according to the reduced mean free path. The specific heat of the sample is increased, since additional energy excitations correspond to an enhanced capacity for storing heat. These aspects inspired Anderson *et al.* [And72] and Phillips [Phi72] to independently come up with a phenomenological description for these intrinsic systems, called the *standard tunneling model*.

2.2.2 Saturation and absorption

The newly revealed deviations from the expected behaviour opened an unexplored field for the investigation of these low energy excitations. Their strong coupling to phonons was further affirmed by many experiments [Hun72, Hun73, Gol73]. Some measurements observed a saturation effect of the ultrasonic absorption, which led to the conclusion that the underlying systems can be understood as highly anharmonic oscillators or respectively as two-level systems (TLS). Additionally, experiments with electric field excitations showed an analogous coupling to the photon field via exter-

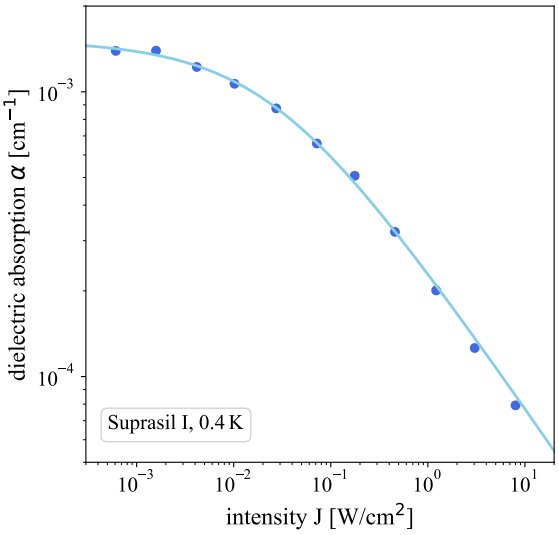

Figure 2.5: Dielectric saturation measurement conducted on Suprasil I. The dielectric absorption coefficient decreases with increasing intensity. The light-blue line describes the theoretical model from [Hun76]. The experimental data is adapted from [vS77].

nal electric excitations. A saturation measurement [vS77] of the dielectric absorption coefficient α is depicted in figure 2.5 in dependence of the field intensity J. The investigated material was a vitreous silica sample containing 1200 ppm of OH^- (Suprasil I). It displays the decrease of the dielectric absorption with an increase of the applied intensity, which is well described by the theory (light-blue line) derived in [Hun76]. The measurements can be interpreted by the influence of the intrinsic two-level systems. For low intensities they cause an additional dielectric absorption through their corresponding energy scale. For very high intensities nearly all of these two-level systems are saturated and therefore can not contribute to the absorption, which results in an increased transparency of the sample.
Another important observation was made by the so called *hole burning* experiments. Since the two-level systems are assumed to be broadly distributed over their energy scale, excitations with different frequencies of the external field should be possible. The measurements thereby revealed a broad "saturation hole" in the distribution function of the two-level systems for the application of a strong excitation pulse. A corresponding measurement [Arn78] on vitreous silica is shown in figure 2.6. The experiment used a variable frequency for the strong saturation pulse and a fixed frequency for the weak probing pulse of 780 MHz in order to measure the variation of the resonant absorption coefficient [Hun82]. The pulse duration was changed for the two separate measurements in figure 2.6 from 0.7 µs to 1.2 µs. The results show a large spectral width over several MHz, which was rather surprising since the frequency uncertainty of the saturation pulse was orders of magnitude smaller. The broadening was linked to the interaction of the two-level systems with random fluctuations of the surrounding strain field as described by the theory of *spectral diffusion* [Bla77]. The energy of the saturation pulse can thereby diffuse in frequency space over time through interactions with the ensemble of two-level systems. The

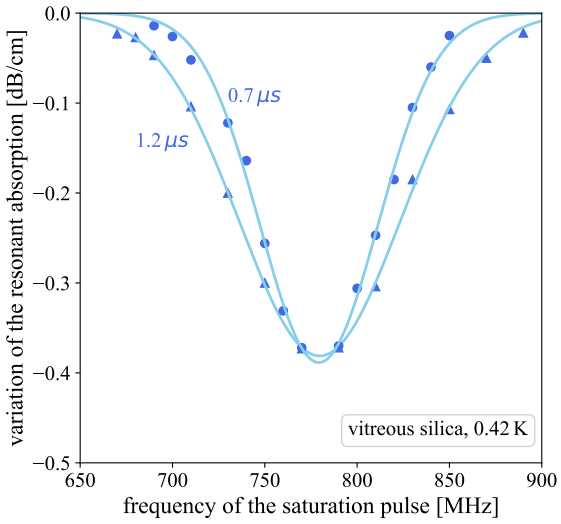

Figure 2.6: Variation of the resonant absorption for a weak probe pulse with a frequency of 780 MHz and a variable frequency for the strong saturation pulse. The plot shows two measurements for pulse durations of 0.7 µs and 1.2 µs. The data is adapted from [Arn78].

two measurements in figure 2.6 were the first evidence to show this broadening over time. Similar measurement were made with a variation of the field intensity of the saturation pulse [Arn75]. Their results showed a deeper hole for higher intensities, which is reasonable when compared to the relation plotted in figure 2.5.

Generally it should be noted, that an understanding of the intrinsic two-level systems, which are characteristic for amorphous materials, is essential for a description of the microscopic processes. The following section is therefore dedicated to give a detailed overview of the theoretical definition and possible interactions.

2.3 Two level systems

A two-level system is defined as a quantum mechanical object consisting of two independent quantum states. The coupling between these two states yields a set of eigenstates as a superposition of the initial single state solutions. The system can absorb a quantum of energy to perform a transition between its energy levels via resonant absorption, stimulated or spontaneous emission. In general, such a system is connected to a measurable physical property for example spin 1/2-particles like electrons. The underlying formalism to describe a two-level system is important for many fields in physics like quantum optics, quantum computing, (nuclear) magnetic resonance and condensed matter.
The additional low energy excitations which are characteristic for amorphous materials can also be attributed to two-level systems. This section outlines how these systems can be described, how they are distributed over their characterizing parameters and how they interact with external field excitations.

2.3.1 Standard tunneling model

The measurements of Zeller and Pohl [Zel71] revealed an additional low temperature contribution to the specific heat and the thermal conductivity. These measurements prompted Anderson *et al.* [And72] and Phillips [Phi72] to come up with a phenomenological model, the *standard tunneling model* (STM), without any specific microscopic assumptions. The basic idea is that the amorphous structure of the material, more than the atomic composition, is the crucial factor responsible for the low temperature properties of these materials. Due to their inherent property of a broad distribution of binding length and binding angles, the disordered structure contains sites where single atoms or groups of atoms can occupy two positions very similar in energy. This characteristic can be modelled by a double-well potential separated by a potential barrier of hight V as pictured in figure 2.7. The parameter d describes an abstract distance in configuration space, which combines possible translations as well as rotations. The asymmetry energy Δ quantifies the energy difference between the two minima. The two sites a and b can each be approximated by a single harmonic potential with a corresponding ground state wave function [Nol13] of

$$\Psi_{\mathrm{a/b}} = \left(\frac{m\Omega}{\pi\hbar}\right)^{\frac{1}{4}} \exp\left(-\frac{m\Omega}{2\hbar}\left(x \pm \frac{d}{2}\right)^2\right). \tag{2.2}$$

The participating atoms can thereby be described as a quasiparticle of mass m. The frequency of oscillation Ω in a single well yields a ground state energy of

$$E_0 = \frac{\hbar\Omega}{2}. \tag{2.3}$$

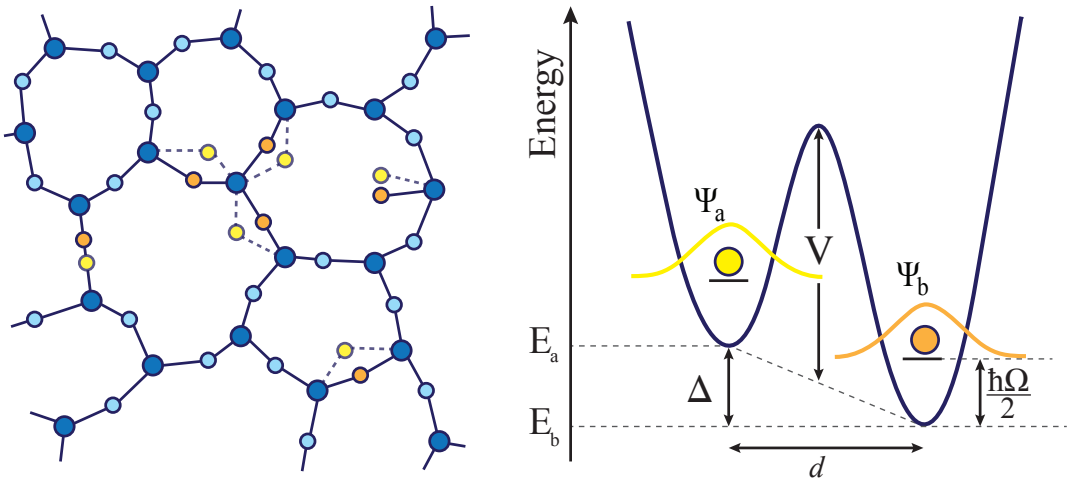

Figure 2.7: Schematic illustration of the tunneling sites. **Left:** structural rearrangement of atoms or groups of atoms from position a (yellow) to position b (orange). The illustration is based on a 2D-version of a Si_2O_3-lattice. **Right:** potential well of a tunneling system. The two sites can be described by a harmonic potential with the corresponding ground states Ψ_a (yellow) and Ψ_b (orange).

A typical value for the excitation frequency of such a single well is of the order of $\hbar\Omega/k_B \sim 100\,\mathrm{K}$. For the description of these systems below 1 K it is sufficient to neglect higher excitations of the single wells. The only possibility for the particle to change position is therefore to tunnel between the two sites trough the potential barrier.
In order to establish a Hamiltonian for the double-well potential, the overlap of the single wave functions E_{ab} and E_{ba} respectively is estimated with the WKB[2] approximation. This method uses a given potential but since the specific microscopic picture of the tunneling process is unclear, the energy overlap is described by a simplified expression with an exponential dependency

$$E_{ab} = E_{ba} = -\frac{\hbar\Omega_0}{2}\exp(-\lambda). \tag{2.4}$$

The energy $\frac{\hbar\Omega_0}{2}$ is of the order of the zero-point energy and the tunneling parameter is approximated as

$$\lambda \approx \sqrt{\frac{2mV}{\hbar^2}}d. \tag{2.5}$$

The coupling of the two states can then be described by a Hamiltonian [Phi87] for the double-well potential of the form

$$H_0 = \begin{pmatrix} E_a + \frac{\hbar\Omega}{2} & E_{ab} \\ E_{ba} & E_b + \frac{\hbar\Omega}{2} \end{pmatrix}. \tag{2.6}$$

[2]named after G. Wentzel, H. A. Kramers and L. Brillouin [Wen26, Kra26, Bri26]

Here E_a and E_b are the local minimal energies of the double-well potential as depicted in figure 2.7. The above defined tunneling parameter λ has limits for which the STM meets its assumptions. The lower limit for the tunneling parameter λ_min can be understood as a measure so that only photon-assisted tunneling occurs [And72]. In this case the next available level of the single well is not accessible for the system in this energy range and the wells are sufficiently separated by the tunneling barrier. Otherwise the single well can not be approximated by a ground state of a harmonic potential since higher orders in the double well polynomial would become relevant. The STM picture can then be supplemented by anharmonic oscillations in a so-called *soft potential*. In this case there are additional localized modes, which are responsible for the higher temperature properties of glasses. The soft-potential model [Kar83, Kar87, Par93] is only relevant at several Kelvin and therefore not further discussed here.
The upper limit for the tunneling parameter λ_max corresponds to the maximum barrier height, mass of the tunneling particle or distance between the tunneling sites, for which the coupling of the two single wells is not strong enough to form a tunneling system. In most cases the duration of the experiment is the limiting factor for the minimal accessible tunneling parameter since the tunneling relaxation time of such systems is longer than the experimental time scale.
The Hamiltonian in equation 2.6 can be simplified by redefining the zero point of the energy as the mean of the two ground state energies of the single harmonic potentials

$$\mathcal{H}_0 = \frac{1}{2}\begin{pmatrix} \Delta & -\Delta_0 \\ -\Delta_0 & -\Delta \end{pmatrix}. \tag{2.7}$$

The hereby defined tunneling splitting

$$\Delta_0 = \hbar\Omega_0 \exp(-\lambda) \tag{2.8}$$

depends on the tunneling parameter λ and is therefore also restricted by the same limits as mentioned above. The obtained Hamiltonian can now be transformed into the eigenbasis of the coupled system resulting in

$$\hat{\mathcal{H}}_0 = \frac{1}{2}\begin{pmatrix} E & 0 \\ 0 & -E \end{pmatrix} \tag{2.9}$$

with an energy splitting of the eigenstates

$$E = \sqrt{\Delta^2 + \Delta_0^2}. \tag{2.10}$$

The transformation from the single well basis into the eigenbasis of the coupled states is achieved via the rotation by an angle ϕ through

$$\hat{\mathcal{H}}_0 = \mathcal{T}_\phi \mathcal{H} \mathcal{T}_\phi^{-1} \tag{2.11}$$

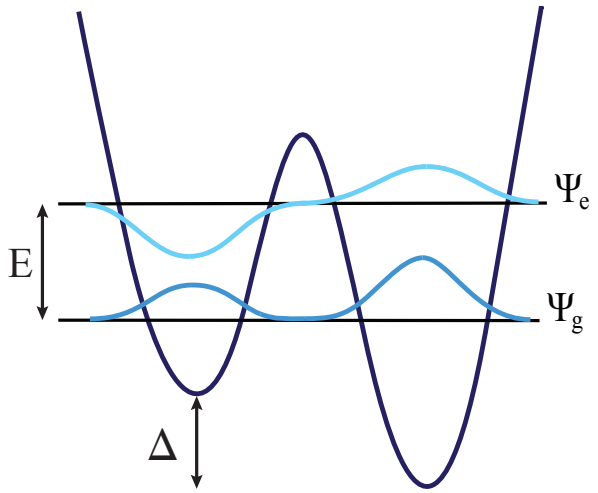

Figure 2.8: Schematic illustration for the wave function of the ground state Ψ_g (dark blue) and the excited state Ψ_e (light blue). The two states are separated by the energy splitting E and the local minima of the double well potential differ by the asymmetry energy Δ.

with the rotation matrices

$$\mathcal{T}_\phi = \begin{pmatrix} \cos(\phi) & -\sin(\phi) \\ \sin(\phi) & \cos(\phi) \end{pmatrix} \quad \text{and} \quad \mathcal{T}_\phi^{-1} = \begin{pmatrix} \cos(\phi) & \sin(\phi) \\ -\sin(\phi) & \cos(\phi) \end{pmatrix} \tag{2.12}$$

and the rotation angle $\phi = \frac{1}{2}\arctan(\frac{\Delta_0}{\Delta})$. The corresponding wave functions of the eigenstates can be derived by the inverse rotation of the ground state Ψ_g and the excited state Ψ_e into the basis of the single wells

$$\Psi_g = \quad \cos(\phi)\Psi_a + \sin(\phi)\Psi_b \tag{2.13}$$

$$\Psi_e = -\sin(\phi)\Psi_a + \cos(\phi)\Psi_b. \tag{2.14}$$

The obtained wave functions are schematically depicted in figure 2.8 with a symmetric ground state Ψ_g and an asymmetric excited state Ψ_e. A tunneling particle is therefore delocalized in both of the coupled states. Higher values of the asymmetry energy Δ only increase the probability to find a tunneling particle in the lower well in its ground state. The regime where $\Delta_0/\Delta \ll 1$ is referred to as weak coupling. In this case the eigenstates Ψ_g and Ψ_e become nearly localized except for a phase factor and correspond to the single well solutions Ψ_a and Ψ_b. When the condition $\Delta_0/\Delta \gg 1$ is fulfilled on the other hand, complete mixing of the single well solutions respectively a delocalisation of the states is achieved.

2.3.2 Distribution function

With the obtained description for a single TLS, the macroscopic properties of the amorphous material can be derived by an integration over all contributing systems.

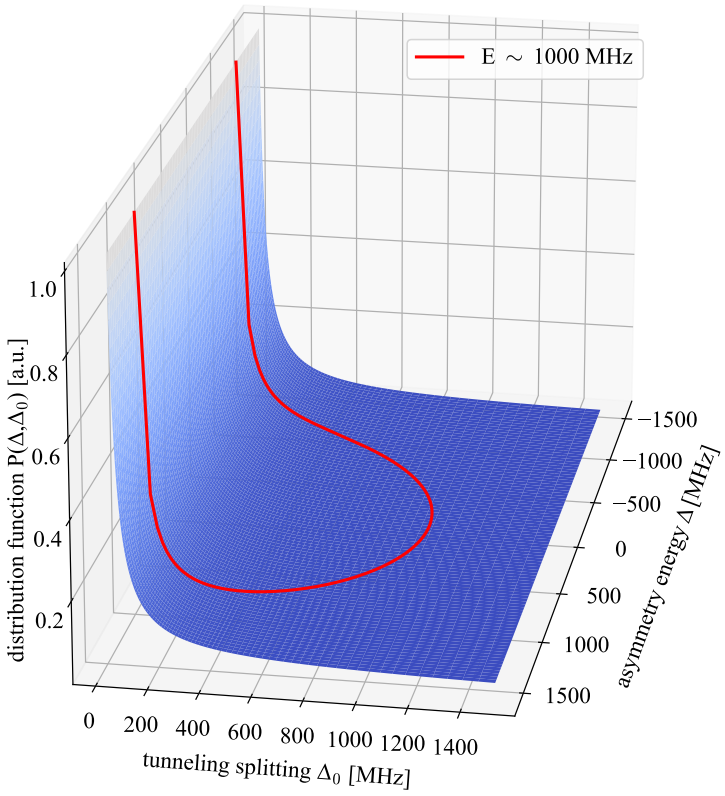

Figure 2.9: Graphical illustration of the distribution function $P(\Delta, \Delta_0)$ as a function of the asymmetry energy Δ and the tunneling splitting Δ_0. Since P_0 was chosen as $\Delta_{0,\mathrm{min}}$ the distribution function is not normalized and plotted in arbitrary units. A constant energy of E/h =1000 MHz was drawn on the surface plot for reference.

This requires a distribution function of the two defining parameters, the asymmetry energy Δ and the tunneling parameter λ. The inherent disorder causes a broad distribution over the parameter space. For the standard tunneling model the assumption was made that the distribution function $P(\Delta, \lambda)$ varies only slightly over Δ and λ. The distribution function can therefore be written as

$$P(\Delta, \lambda)\,\mathrm{d}\Delta\,\mathrm{d}\lambda = P_0\,\mathrm{d}\Delta\,\mathrm{d}\lambda \tag{2.15}$$

with the constant parameter P_0. This value is dependent on the investigated material and has to be determined by the experiment. Further discussion will mostly use Δ and Δ_0 as the set of parameters to describe the TLS properties. The distribution function can therefore be transformed with relation 2.8 to read

$$P(\Delta, \Delta_0)\,\mathrm{d}\Delta\,\mathrm{d}\Delta_0 = P_0 \left|\frac{\partial\lambda}{\partial\Delta_0}\right| \mathrm{d}\Delta\,\mathrm{d}\Delta_0 = \frac{P_0}{\Delta_0}\,\mathrm{d}\Delta\,\mathrm{d}\Delta_0. \tag{2.16}$$

The corresponding plot can be seen in figure 2.9. A constant energy of 1000 MHz$\cdot h$ for reference is drawn as a red line. According to equation 2.10 constant energies take the form of half-circles in this representation. For further calculations, especially when integrating over the distribution function, it is convenient to express the asymmetry energy Δ in terms of the energy splitting E. Equation 2.16 therefore takes the form

of

$$P(E,\Delta_0)\,\mathrm{d}E\,\mathrm{d}\Delta_0 = P(\Delta,\Delta_0)\left|\frac{\partial\Delta}{\partial E}\right|\,\mathrm{d}E\,\mathrm{d}\Delta_0 = P_0\frac{E}{\Delta_0}\frac{1}{\sqrt{E^2-\Delta_0^2}}\,\mathrm{d}E\,\mathrm{d}\Delta_0. \quad (2.17)$$

In order to avoid the divergence of the integration it is necessary to choose a lower limit for the tunneling splitting $\Delta_{0,\mathrm{min}}$. Similar to the argument for the tunnel parameter λ a minimal tunneling splitting can be understood as the limit for the minimal coupling between the two single wells. Below this value the system is more likely to act as two isolated wells instead of a double well potential since the tunneling probability is vanishingly small. The second divergence of equation 2.17 at $E = \Delta_0$ can be integrated and therefore does not need an upper limit for the integration.

2.3.3 Thermal equilibrium and occupation difference

At finite temperatures an ensemble of N non-interacting two-level systems aims towards thermal equilibrium. The accessible thermal energy at a specific temperature thereby saturates matching energy states. The occupation difference ΔN of the ground state ($E_\mathrm{g} \equiv 0$) and the excited state ($E_\mathrm{e} \equiv E$) can be derived with methods from statistical physics. The partition function at a certain temperature T of the micro states can be expressed by

$$Z = \sum_{i=\mathrm{g,e}} \exp\left(-\frac{E_i}{k_\mathrm{B}T}\right) = 1 + \exp\left(-\frac{E}{k_\mathrm{B}T}\right) \quad (2.18)$$

with the Boltzmann constant k_B. The occupation probabilities for the ground state

$$p_\mathrm{g} = \frac{1}{Z}\exp\left(-\frac{E_\mathrm{g}}{k_\mathrm{B}T}\right) = \frac{1}{1+\exp\left(-\frac{E}{k_\mathrm{B}T}\right)} \quad (2.19)$$

and the exited state

$$p_\mathrm{e} = \frac{1}{Z}\exp\left(-\frac{E_\mathrm{e}}{k_\mathrm{B}T}\right) = \frac{\exp\left(-\frac{E}{k_\mathrm{B}T}\right)}{1+\exp\left(-\frac{E}{k_\mathrm{B}T}\right)} \quad (2.20)$$

follow directly from equation 2.18 and the Boltzmann factor of the corresponding micro state. The difference in occupation probability in thermal equilibrium

$$\Delta p = p_\mathrm{g} - p_\mathrm{e} = \tanh\left(\frac{E}{2k_\mathrm{B}T}\right) \quad (2.21)$$

is connected to the occupation difference by the number of systems N and therefore simply reads

$$\Delta N = N\,\Delta p = N\tanh\left(\frac{E}{2k_\mathrm{B}T}\right). \quad (2.22)$$

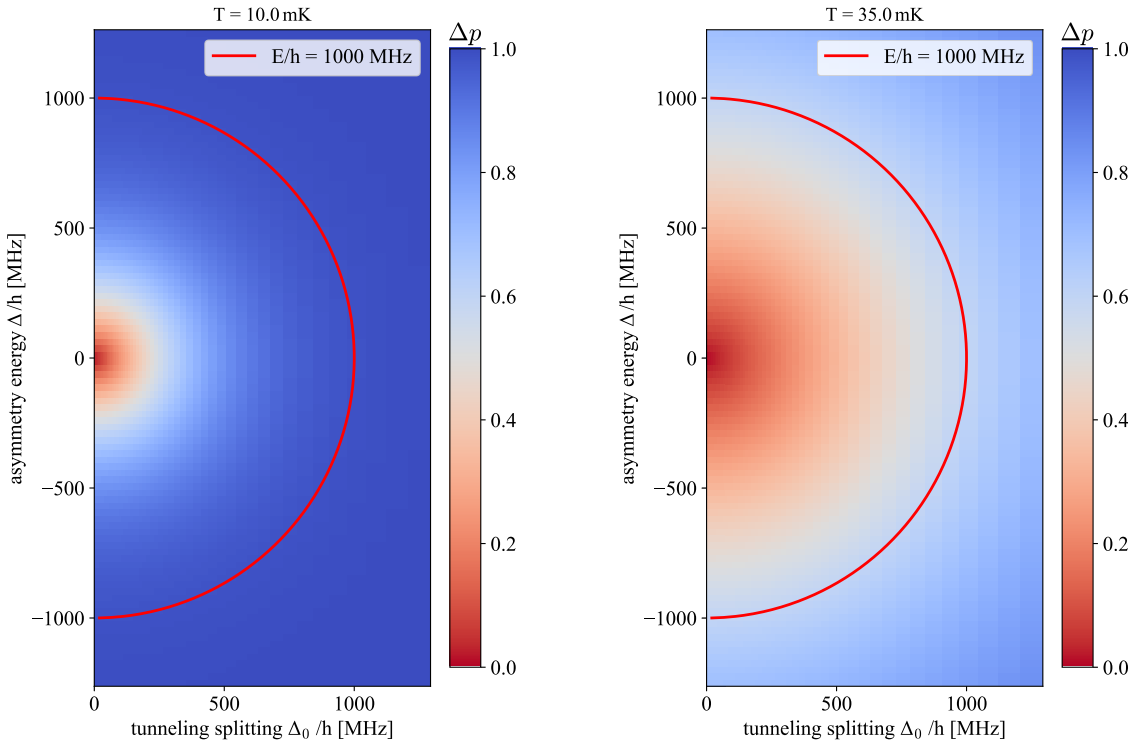

Figure 2.10: Illustration of the difference in occupation probability as a function over the asymmetry energy Δ and the tunneling splitting Δ_0 for 10 mK (**left**) and 35 mK (**right**). A constant energy of E/h =1000 MHz is drawn as a red line for reference.

Figure 2.10 shows equation 2.21 and therefore the functional relation of the occupation difference over the two defining parameters Δ and Δ_0 at temperatures of 10 mK and 35 mK. Since the equation is solely dependent on E, the plot shows radial symmetry. For an increased temperature less systems are in the ground state and the occupation difference converges towards zero.

2.3.4 Polarisation and the dielectric function

A dielectric material contains intrinsic dipole moments p_i, which can be reoriented under the influence of an external electric field $F(t)$. The resulting macroscopic polarisation $P(t)$ can be described by a sum over all microscopic dipole moments in the given volume V as

$$P(t) = \frac{1}{V} \sum_i p_i. \tag{2.23}$$

For the most general case, the polarisation is expressed in dependence of the electric field [Boy20] by

$$P(t) = P^{(0)} + \varepsilon_0 \chi^{(1)} F(t) + \varepsilon_0 \chi^{(2)} F^2(t) + \varepsilon_0 \chi^{(3)} F^3(t) + ... \tag{2.24}$$

where ε_0 is the permittivity of free space. The constant polarisation $P^{(0)}$ can be understood as a built in polarisation and is only non-zero for ferroelectric materials. The second term contains the linear susceptibility $\chi^{(1)}$ for which the induced polarisation is directly proportional to the external electric field. The parameters $\chi^{(2)}$ and $\chi^{(3)}$ represent the second- and third order non-linear susceptibilities. Second order effects only occur in systems without centrosymmetry. Since gases, liquids, amorphous materials and some crystals show inversion symmetry due to their isotropy the second order effects disappear in these systems. Third order non-linear effects on the other hand can be present in both types of media. For disordered solids like glasses linear and third order effects are therefore mostly relevant. Generally, F and P are vectors with susceptibilities as different ranked tensors. Due to the isotropy, it is sufficient for simplicity to treat both quantities as scalars.
The entire field in the material caused by free and bound charges can be expressed by the electric displacement field

$$D = \varepsilon_0 E + P = \varepsilon_0(1+\chi)F = \varepsilon F. \tag{2.25}$$

The here defined dielectric function $\varepsilon = \varepsilon_0(1+\chi)$ can be generalized for alternating electric fields of frequency ω as a complex function of the form

$$\varepsilon(\omega) = \varepsilon'(\omega) + i\varepsilon''(\omega). \tag{2.26}$$

In this representation the real part ε' can be understood as the energy conserving mechanisms, which are in phase with the external fields and the imaginary part ε'' as the out-of-phase dissipative processes. An often used definition is the dielectric loss

$$\tan(\delta) = \frac{\varepsilon''}{\varepsilon'} \tag{2.27}$$

as the ratio of imaginary and real part of the dielectric function. Generally, there are other mechanisms that cause additional effects like ionic, electronic or atomic contributions to the polarisation of a material, but the discussion will focus on TLS as the most relevant contribution at low temperatures.

2.3.5 Interaction of TLS with electric fields

In section 2.3.1 the *standard tunneling model* gave the basic description of a single TLS present in an amorphous material. In order to describe the interaction of the associated dipole moments p of these systems with an external field and to derive the individual contributions to the macroscopically measurable quantities, the Hamiltonian from equation 2.7 has to be extended by a perturbation Hamiltonian

$$\mathcal{H} = \mathcal{H}_0 + \mathcal{H}_{\text{per}} = \frac{1}{2}\begin{pmatrix} \Delta & -\Delta_0 \\ -\Delta_0 & -\Delta \end{pmatrix} + \frac{1}{2}\begin{pmatrix} \delta\Delta & \delta\Delta_0 \\ \delta\Delta_0 & -\delta\Delta \end{pmatrix}. \tag{2.28}$$

Usually the variation in tunneling splitting $\delta\Delta_0$ can be neglected [Ens05]. In [Phi81] Phillips stated that the wavelength of an external field is much larger than the dimension of a tunneling site. The local variation of potential energy therefore does not influence the tunneling barrier drastically. Different orientations of the dipoles in their individual wells and the related change in asymmetry energy is much more significant. Experiments with strain fields [Lis15, Bre17] and electric fields [Sar16] show good agreement with a theory based on this assumption. The change in asymmetry energy under the influence of an electric field then reads

$$\delta\Delta(t) = 2p_{\mathrm{eff}}F(t) = 2p_{\mathrm{eff}}F_{\mathrm{ac}}\cos(\omega t) \tag{2.29}$$

with the amplitude of the external electric field F_{ac} and the corresponding angular frequency ω. Note that not the full dipole moment contributes to the variation in energy since only the difference in the vector components parallel to the field vector add to the effective dipole moment p_{eff}. For acoustic measurements the dipole moment is replaced with the deformation potential γ and the electric field by the mechanical strain e [Ens05].
The full Hamiltonian of equation 2.28 can be transformed into the eigenbasis of Ψ_{g} and Ψ_{e} with the relation 2.12 of the rotation matrices. The perturbed Hamiltonian can be expressed as

$$\hat{\mathcal{H}} = \hat{\mathcal{H}}_0 + \hat{\mathcal{H}}_{\mathrm{per}} = \frac{1}{2}\begin{pmatrix} E & 0 \\ 0 & -E \end{pmatrix} + \frac{1}{E}\begin{pmatrix} \Delta & \Delta_0 \\ \Delta_0 & -\Delta \end{pmatrix} p_{\mathrm{eff}}F_{\mathrm{ac}}\cos(\omega t). \tag{2.30}$$

An external electric field therefore modifies the diagonal terms of the Hamiltonian and accordingly the energy splitting of the two-level system by

$$\delta E_{\mathrm{dia}} = 2\frac{\Delta}{E}\, p_{\mathrm{eff}}F(t). \tag{2.31}$$

The off-diagonal terms

$$\delta E_{\mathrm{off}} = \frac{\Delta_0}{E} p_{\mathrm{eff}}F(t) \tag{2.32}$$

on the other hand are responsible for additionally induced transitions between the ground state Ψ_{g} and the excited state Ψ_{e}. This equation is directly linked to the Rabi frequency as will be discussed later in section 2.3.6.
In order to describe the behaviour of the tunneling systems under the influence of the electric field, the density matrix formalism is used in the following. This method is a powerful tool to understand individual systems as well as an entire ensemble. The density operator hereby is a generalization of the description of pure quantum states by their eigenvectors and wave functions. It uses a statistical mixture of pure states (mixed state) to characterize the observed ensemble by probabilities p_i to find an arbitrarily selected system in the corresponding pure state Ψ_i. This formalism is

crucial in order to include relaxation and decoherence times of the tunneling systems since their quantities are defined as an average value of the ensemble. The density operator is generally expressed by

$$\hat{\rho} = \sum_i p_i \left|\Psi_i\right\rangle \left\langle\Psi_i\right| \tag{2.33}$$

as a sum over all possible pure states. For the tunneling system the pure states can be written as a linear combination of the ground and the excited state

$$\left|\Psi_i\right\rangle = a_i \left|\Psi_\mathrm{e}\right\rangle + b_i \left|\Psi_\mathrm{g}\right\rangle \tag{2.34}$$

weighted with the corresponding probability amplitudes. The density matrix is a positive semi-definite matrix, which in the basis of the ground state Ψ_g and the excited state Ψ_e takes the form of

$$\hat{\rho} = \begin{pmatrix} \rho_\mathrm{ee} & \rho_\mathrm{eg} \\ \rho_\mathrm{ge} & \rho_\mathrm{gg} \end{pmatrix}. \tag{2.35}$$

The diagonal matrix elements ρ_gg and ρ_ee represent the probability to find the system in the ground state, respectively in the excited state. Since the trace of the density matrix is one, the relation $\rho_\mathrm{ee} + \rho_\mathrm{gg} = 1$ holds, which is reasonable for identifying both terms as probabilities. The off-diagonal matrix elements describe the mixing of states. By definition, the density operator can be used to calculate the expectation value of an observable $\hat{O}$ as $\langle\hat{O}\rangle = \mathrm{tr}(\hat{\rho}\hat{O})$, where tr() denotes the trace.
To obtain the time evolution of the density operator for a given tunneling system, the von Neumann equation

$$i\hbar\frac{\partial\hat{\rho}}{\partial t} = \hat{\mathcal{H}}\hat{\rho} - \hat{\rho}\hat{\mathcal{H}} \tag{2.36}$$

has to be solved with the perturbation Hamilton from equation 2.30. This yields a system of four linear first order differential equations for the components of the density matrix, which read

$$\dot{\rho}_\mathrm{ee} = \frac{\Delta_0}{i\hbar E}\, p_\mathrm{eff} F(t)\,(\rho_\mathrm{ge} - \rho_\mathrm{eg}) - \frac{1}{2\tau_1}\left((\rho_\mathrm{ee} - \rho_\mathrm{gg}) + \tanh\left(\frac{E}{2k_\mathrm{B}T}\right)\right) \tag{2.37}$$

$$\dot{\rho}_\mathrm{gg} = \frac{\Delta_0}{i\hbar E}\, p_\mathrm{eff} F(t)\,(\rho_\mathrm{eg} - \rho_\mathrm{ge}) + \frac{1}{2\tau_1}\left((\rho_\mathrm{ee} - \rho_\mathrm{gg}) + \tanh\left(\frac{E}{2k_\mathrm{B}T}\right)\right) \tag{2.38}$$

$$\dot{\rho}_\mathrm{ge} = \frac{\Delta_0}{i\hbar E}\, p_\mathrm{eff} F(t)\,(\rho_\mathrm{ee} - \rho_\mathrm{gg}) - \frac{1}{i\hbar}\left(E + \frac{2\Delta}{E}\, p_\mathrm{eff} F(t)\right)\rho_\mathrm{ge} - \frac{\rho_\mathrm{ge}}{\tau_2} \tag{2.39}$$

$$\dot{\rho}_\mathrm{eg} = \frac{\Delta_0}{i\hbar E}\, p_\mathrm{eff} F(t)\,(\rho_\mathrm{gg} - \rho_\mathrm{ee}) + \frac{1}{i\hbar}\left(E + \frac{2\Delta}{E}\, p_\mathrm{eff} F(t)\right)\rho_\mathrm{eg} - \frac{\rho_\mathrm{eg}}{\tau_2}. \tag{2.40}$$

Additionally, the equations were expanded by two relaxation time scales τ_1 and τ_2. The longitudinal relaxation time τ_1 accounts for a possible decay of the systems state

to the thermal equilibrium value of the ensemble, which can be defined as

$$\overline{\Delta\rho}_0 = \tanh\left(\frac{E}{2k_\mathrm{B}T}\right). \tag{2.41}$$

The transversal relaxation time τ_2 represents the tendency of an ensemble of systems to dephase due to random fluctuations in the local fields. A deeper description for these quantities will be given in section 2.4.1 and section 2.4.2 respectively. The description with the density matrix formalism is analogous to the Bloch equations [Blo46]. In this case pure states are represented by vectors pointing on the Bloch sphere and mixed states are depicted as vectors in the interior. This connection can be seen when calculating the expectation values for the Pauli matrices

$$\langle\hat{\sigma_x}\rangle = \rho_\mathrm{eg} + \rho_\mathrm{ge} \tag{2.42}$$
$$\langle\hat{\sigma_y}\rangle = i(\rho_\mathrm{eg} - \rho_\mathrm{ge}) \tag{2.43}$$
$$\langle\hat{\sigma_z}\rangle = \rho_\mathrm{ee} - \rho_\mathrm{gg}, \tag{2.44}$$

since these quantities correspond to the entries of the Bloch vector. The further calculation is therefore based on the solutions of the Bloch equations done by Hunklinger *et al.* [Hun76] for the case of acoustic attenuation, respectively on [Car94, Bur98] for electric field excitations. With the definition of the occupation difference $\Delta\rho = \rho_\mathrm{gg} - \rho_\mathrm{ee}$ equations 2.37 and 2.38 can be combined into one equation

$$\dot{\Delta\rho} = 2\frac{\Delta_0}{i\hbar E}\, p_\mathrm{eff} F(t)\,(\rho_\mathrm{eg} - \rho_\mathrm{ge}) - \frac{\Delta\rho - \overline{\Delta\rho}}{\tau_1}. \tag{2.45}$$

The electric field also induces variations in the thermal equilibrium value $\overline{\Delta\rho}$ due to the perturbation in the energy splitting $E + \delta E_\mathrm{dia}$. The relation between an excitation and the consequently time dependent thermal equilibrium value can be approximated by a Taylor expansion of equation 2.41, which reads

$$\overline{\Delta\rho} \approx \overline{\Delta\rho}_0 + \overline{\Delta\rho}_1\cos(\omega t) = \overline{\Delta\rho}_0 + \left(\frac{\Delta}{E}\right)\frac{p_\mathrm{eff}F_\mathrm{ac}}{k_\mathrm{B}T}\,\mathrm{sech}^2\left(\frac{E}{2k_\mathrm{B}T}\right)\cos(\omega t). \tag{2.46}$$

The set of equations to solve the tunneling system problem can thus be rewritten as

$$\dot{\rho}_\mathrm{ge} = -\frac{\Delta_0}{i\hbar E}\, p_\mathrm{eff}F_\mathrm{ac}\cos(\omega t)\,\Delta\rho - \frac{1}{i\hbar}\left(E + \frac{2\Delta}{E}\, p_\mathrm{eff}F_\mathrm{ac}\cos(\omega t)\right)\rho_\mathrm{ge} - \frac{\rho_\mathrm{ge}}{\tau_2} \tag{2.47}$$
$$\dot{\rho}_\mathrm{eg} = \frac{\Delta_0}{i\hbar E}\, p_\mathrm{eff}F_\mathrm{ac}\cos(\omega t)\,\Delta\rho + \frac{1}{i\hbar}\left(E + \frac{2\Delta}{E}\, p_\mathrm{eff}F_\mathrm{ac}\cos(\omega t)\right)\rho_\mathrm{eg} - \frac{\rho_\mathrm{eg}}{\tau_2} \tag{2.48}$$
$$\dot{\Delta\rho} = 2\frac{\Delta_0}{i\hbar E}\, p_\mathrm{eff}F_\mathrm{ac}\cos(\omega t)\,(\rho_\mathrm{eg} - \rho_\mathrm{ge}) - \frac{\Delta\rho - (\overline{\Delta\rho}_0 + \overline{\Delta\rho}_1\cos(\omega t))}{\tau_1}. \tag{2.49}$$

The measurable quantity of the tunneling system is its contribution to the macroscopic polarisation of the sample. The corresponding polarisation operator is an observable and can be derived from equation 2.30 as

$$\hat{\pi} = -\left(\frac{\Delta}{E}\hat{\sigma_z} + \frac{\Delta_0}{E}\hat{\sigma_x}\right) p_{\text{eff}} \tag{2.50}$$

with an expectation value of

$$\langle\hat{\pi}\rangle = \left(\left(\frac{\Delta}{E}\right)\Delta\rho - \left(\frac{\Delta_0}{E}\right)(\rho_{\text{eg}} + \rho_{\text{ge}})\right) p_{\text{eff}}. \tag{2.51}$$

The two terms are later identified by distinct contributing processes. The first term is proportional to the occupation difference and is therefore determined by relaxation. The second term on the other hand is proportional to the transition elements of the density matrix and can hence be understood as a consequence of resonant interactions of the two-level system with the field.
An ansatz to solve the above equations for a steady state is made by

$$R(t) = \begin{pmatrix}\rho_{\text{ge}}(t)\\ \rho_{\text{eg}}(t)\\ \Delta\rho(t)\end{pmatrix} = \begin{pmatrix}0\\0\\R_0\end{pmatrix} + \sum_{n=-\infty}^{\infty}\begin{pmatrix}R_+^{(n)}\\ R_-^{(n)}\\ R_z^{(n)}\end{pmatrix} e^{-i\,\omega_n t}. \tag{2.52}$$

with $R_0 = \overline{\Delta\rho}_0$ and $\omega_n = n\,\omega$. Inserting this ansatz into equations 2.47, 2.48 and 2.49 yields $3n$ relations for the prefactors of the sum in equation 2.52. A good approximation is to focus on tunneling systems with frequencies close to the excitation frequency $\omega \approx \omega_0 = E/\hbar$ and with transversal relaxation rates, which are much smaller than the frequency of the electric field, thus $\omega\tau_2 \gg 1$. Therefore coefficients with higher order are less relevant[3] and the most important equations can be written as

$$\left(\frac{1}{\tau_2} \mp i(\omega \pm \omega_0)\right) R_+^{(\pm1)} = -\frac{p_{\text{eff}}F_{\text{ac}}}{2i\hbar}\left(\frac{\Delta_0}{E}\right)(R_0 + R_z^{(0)}) \tag{2.53}$$

$$\left(\frac{1}{\tau_2} \mp i(\omega \mp \omega_0)\right) R_-^{(\pm1)} = \frac{p_{\text{eff}}F_{\text{ac}}}{2i\hbar}\left(\frac{\Delta_0}{E}\right)(R_0 + R_z^{(0)}) \tag{2.54}$$

$$\frac{1}{\tau_1}\ R_z^{(0)} = \frac{p_{\text{eff}}F_{\text{ac}}}{i\hbar}\left(\frac{\Delta_0}{E}\right)(R_-^{(1)} + R_-^{(-1)} - R_+^{(1)} - R_+^{(-1)}) \tag{2.55}$$

$$\left(\frac{1}{\tau_1} \mp i\omega\right) R_z^{(\pm1)} = \frac{1}{2\tau_1}\overline{\Delta\rho}_1. \tag{2.56}$$

The next step is to solve the obtained equations for the prefactors in order to calculate the contribution for the resonant and relaxation processes.

[3] the approximation assumes that $R_\pm^{(0)}$, $R_+^{(\pm2)}$, $R_-^{(\pm2)}$, $R_z^{(\pm2)}$ and higher order terms vanish

Saturation

Inserting the terms from equations 2.53 and 2.54 into equation 2.55 yields the solution for $R_z^{(0)}$. Together with the unperturbed thermal equilibrium value R_0 this yields a relation to describe the saturation behaviour of the observed systems by

$$R_{\mathrm{Sat}} = R_0 + R_z^{(0)} = \tanh\left(\frac{E}{2k_{\mathrm{B}}T}\right)\left(1 - \frac{(F_{\mathrm{ac}}/F_c)^2}{1 + (F_{\mathrm{ac}}/F_c)^2}\, f_{\mathrm{Sat}}(\omega)\right) \tag{2.57}$$

with the line shape function

$$f_{\mathrm{Sat}}(\omega) = \frac{1}{1 + \tilde{\tau_2}^2(\omega - \omega_0)^2} + \frac{1}{1 + \tilde{\tau_2}^2(\omega + \omega_0)^2} \tag{2.58}$$

and the additionally defined parameters

$$\tilde{\tau_2} = \frac{\tau_2}{\sqrt{1 + (F_{\mathrm{ac}}/F_{\mathrm{c}})^2}} \quad \text{and} \quad F_{\mathrm{c}}^{-1} = \frac{\Delta_0}{E}\frac{p_{\mathrm{eff}}}{\hbar}\sqrt{\tau_1\tau_2}. \tag{2.59}$$

From the expression above, it can be deduced that terms, which contain R_{Sat} converge towards zero, if the electric field F_{ac} increases above the critical field limit F_{c}. Otherwise the contribution can be described by the value of the unperturbed equilibrium value R_0. Furthermore, the differential equations automatically lead to a Lorentzian line shape function $f_{\mathrm{Sat}}(\omega)$. This theoretical prediction was experimentally confirmed by so called *hole burning* experiments in [Arn75, Arn78]. Higher field intensities broaden the thereby emerging hole in the distribution function of the tunneling systems.
The functional dependency of the saturation factor R_{Sat} is depicted in figure 2.11 as a function of the asymmetry energy Δ and the tunneling splitting Δ_0. It is thereby normalized on the unperturbed thermal equilibrium value R_0. For field strengths smaller than the critical field F_{c} the saturation effect is insignificant and R_{Sat}/R_0 can be approximated as one. If the field strength reaches the critical value, tunneling systems around the excitation frequency ω start to saturate, as illustrated in figure 2.11 (left). For higher field strengths the band of saturated tunneling systems around the excitation frequency ω gets even wider since the modified relaxation time scale $\tilde{\tau_2}$ is also dependent on the field strength ratio. It is also worth to notice that the width of the saturated band of tunneling systems is increasing, because the critical field F_{c} is dependent on the ratio of Δ_0/E. Symmetric tunneling systems ($\Delta = 0$) are therefore saturated by smaller field excitations, as can be seen from the above defined relation 2.59 of the critical field strength.

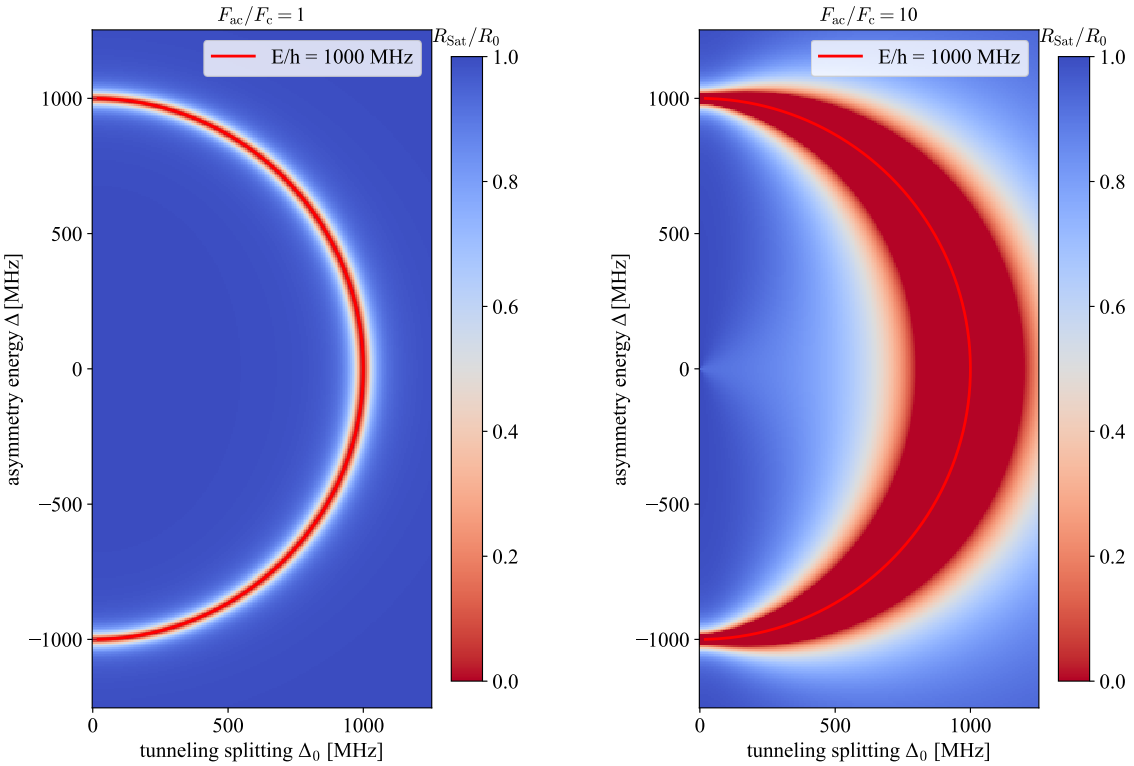

Figure 2.11: Illustration of the normalized saturation factor R_{Sat}/R_0 as a function of the asymmetry energy Δ and the tunneling splitting Δ_0. A constant energy of E/h =1000 MHz is drawn in red as a reference. The saturation is depicted for a field ratio $F_{\mathrm{ac}}/F_{\mathrm{c}}$ of 1 (**left**) and 10 (**right**). The relaxation time scale was chosen rather small as $\tau_2 = 50/\omega$ with ω =1000 MHz for a better visualisation.

Relaxation contribution

The contribution for the relaxation processes can be derived from equation 2.56 and the ansatz 2.52, which yields

$$R_z^{(\pm 1)} = \frac{\overline{\Delta\rho_1}}{2}\left(\frac{1}{1+\tau_1^2\omega^2} \pm i\frac{\tau_1\omega}{1+\tau_1^2\omega^2}\right) \tag{2.60}$$

as the relevant terms for the calculation of the polarisation

$$\langle\hat{\pi}\rangle_{\mathrm{rel}} = p_{\mathrm{eff}}\left(\frac{\Delta}{E}\right)\left(R_z^{(+1)}e^{-i\omega t} + R_z^{(-1)}e^{i\omega t}\right). \tag{2.61}$$

The constant terms of the thermal equilibrium value were neglected, since only components in or out-of-phase with the external electric field are relevant for the measurable change in polarisation. The definition of the linear susceptibility from equation 2.24 gives a relation to express the contribution of the tunneling systems to the

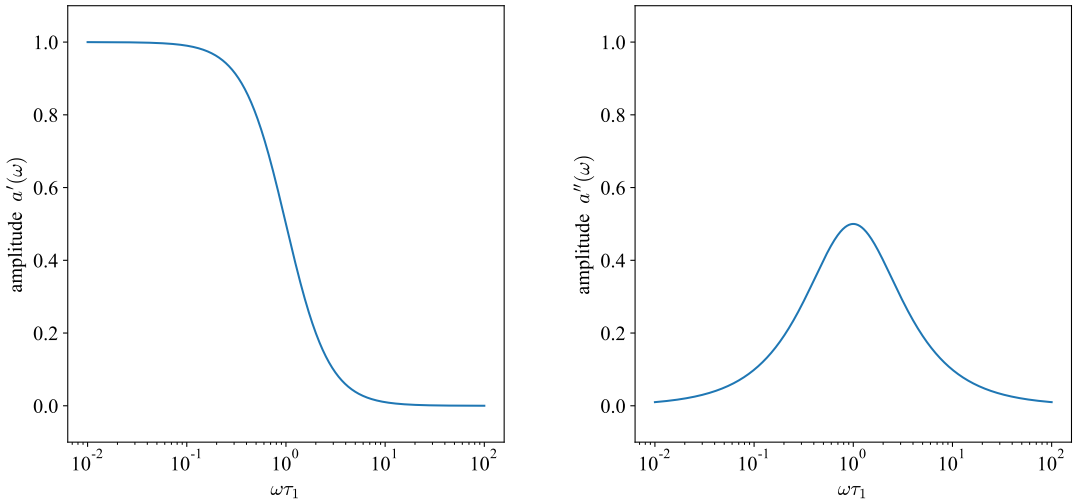

Figure 2.12: Frequency dependence of the relaxation contribution to the linear susceptibility as a function of $\omega\tau_1$. **Left:** in-phase component. **Right:** out-of-phase component.

material properties as

$$\chi'_{\mathrm{rel}} = \left(\frac{\Delta}{E}\right)^2 \frac{p_{\mathrm{eff}}^2}{\varepsilon_0 k_{\mathrm{B}} T} \operatorname{sech}^2\left(\frac{E}{2k_{\mathrm{B}}T}\right) a'(\omega) \tag{2.62}$$

$$\text{with} \quad a'(\omega) = \left(\frac{1}{1+\tau_1^2\omega^2}\right) \tag{2.63}$$

for the contribution in phase with the cosine excitation and the terms, which are 90° phase shifted as

$$\chi''_{\mathrm{rel}} = \left(\frac{\Delta}{E}\right)^2 \frac{p_{\mathrm{eff}}^2}{\varepsilon_0 k_{\mathrm{B}} T} \operatorname{sech}^2\left(\frac{E}{2k_{\mathrm{B}}T}\right) a''(\omega) \tag{2.64}$$

$$\text{with} \quad a''(\omega) = \left(\frac{\tau_1\omega}{1+\tau_1^2\omega^2}\right). \tag{2.65}$$

The relaxation mechanism can be understood as the tendency of the dipoles to follow the orientation of the external electric field since the energy splitting E of the tunneling system is constantly modulated by the excitation. It can follow the perturbation by exchanging energy with the surrounding on the characteristic relaxation time scale τ_1. This behaviour is analogous to the description of a classical Debye relaxation process [Deb13].
The frequency dependencies of both quantities are depicted in figure 2.12. If the frequency of the electric field is smaller than the relaxation rate, thus $\omega\tau_1 \ll 1$, the dipoles and therefore the polarisation can follow the excitation. The contribution to the component in phase $a'(\omega)$ is maximal and to the component out-of-phase $a''(\omega)$ is

vanishingly small. For increasing excitation frequencies the dipoles start to dephase due to the comparatively lower relaxation rates. In this regime the tunneling systems are lagging behind the external excitation, which leads to a decrease of the in-phase component $a'(\omega)$ and the emergence of a maximum in the out-of-phase component $a''(\omega)$. For even higher frequencies $\omega\tau_1 \gg 1$ the dipoles are not able to follow the electric field with the relaxation process. Both contribution therefore vanish in this frequency regime.

Resonant contribution

The relevant terms for the resonant contribution can directly be derived from equations 2.53 and 2.54 as

$$R_{+}^{(\pm 1)} = \left(\frac{\Delta_0}{E}\right) \frac{p_{\mathrm{eff}} F_{\mathrm{ac}}}{2\hbar} \tau_2 R_{\mathrm{Sat}} \left(\mp \frac{\tau_2(\omega \pm \omega_0)}{1+\tau_2^2(\omega \pm \omega_0)^2} + i \frac{1}{1+\tau_2^2(\omega \pm \omega_0)^2} \right) \tag{2.66}$$

$$R_{-}^{(\pm 1)} = \left(\frac{\Delta_0}{E}\right) \frac{p_{\mathrm{eff}} F_{\mathrm{ac}}}{2\hbar} \tau_2 R_{\mathrm{Sat}} \left(\pm \frac{\tau_2(\omega \mp \omega_0)}{1+\tau_2^2(\omega \mp \omega_0)^2} - i \frac{1}{1+\tau_2^2(\omega \mp \omega_0)^2} \right). \tag{2.67}$$

The total contribution can be derived from the second term in equation 2.51 and the used ansatz from 2.52 by

$$\langle \pi \rangle_{\mathrm{res}} = -p_{\mathrm{eff}} \left(\frac{\Delta_0}{E}\right) \left(R_{+}^{(+1)} e^{-i\omega t} + R_{+}^{(-1)} e^{i\omega t} + R_{-}^{(+1)} e^{-i\omega t} + R_{-}^{(-1)} e^{i\omega t} \right). \tag{2.68}$$

This expression can be rearranged in order to separate terms which are in phase with the cosine excitation of the external electric field and terms 90 degree phase shifted. With the definition of the polarisation in equation 2.24 the contribution of the resonant process can be expressed by the linear electric susceptibility as the in-phase component

$$\chi'_{\mathrm{res}} = \left(\frac{\Delta_0}{E}\right)^2 \frac{p_{\mathrm{eff}}^2}{\varepsilon_0 \hbar} \tau_2 \, R_{\mathrm{Sat}} \, b'(\omega, \omega_0) \tag{2.69}$$

$$\text{with} \quad b'(\omega, \omega_0) = \left(-\frac{\tau_2(\omega - \omega_0)}{1+\tau_2^2(\omega - \omega_0)^2} + \frac{\tau_2(\omega + \omega_0)}{1+\tau_2^2(\omega + \omega_0)^2} \right) \tag{2.70}$$

and the out-of-phase component

$$\chi''_{\mathrm{res}} = \left(\frac{\Delta_0}{E}\right)^2 \frac{p_{\mathrm{eff}}^2}{\varepsilon_0 \hbar} \tau_2 \, R_{\mathrm{Sat}} \, b''(\omega, \omega_0) \tag{2.71}$$

$$\text{with} \quad b''(\omega, \omega_0) = \left(\frac{1}{1+\tau_2^2(\omega - \omega_0)^2} - \frac{1}{1+\tau_2^2(\omega + \omega_0)^2} \right). \tag{2.72}$$

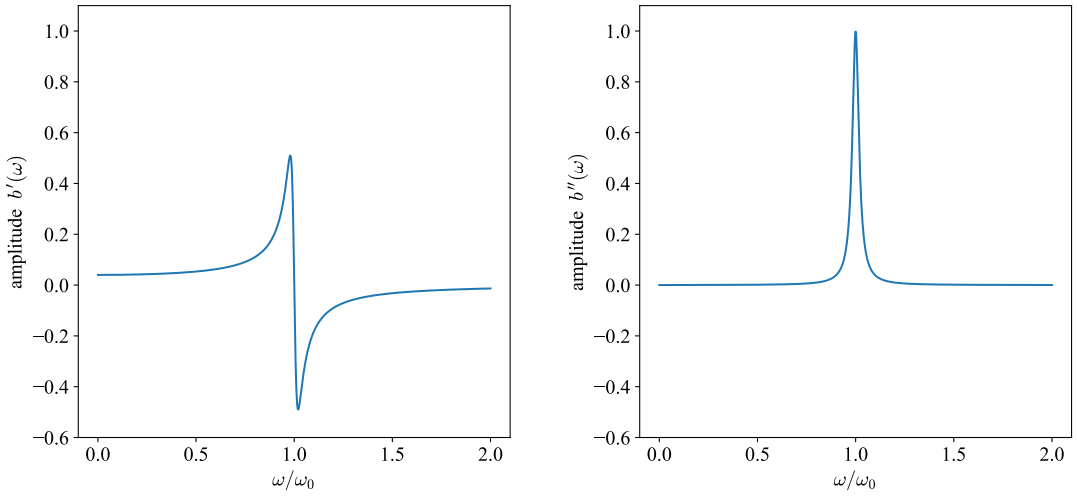

Figure 2.13: Frequency dependence of the resonant contribution to the linear susceptibility as a function of the normalized field frequency ω/ω_0. The relaxation time scale was chosen to be $\tau_2 = 50/\omega_0$. **Left:** in-phase component. **Right:** out-of-phase component.

The resonant contribution can be explained similar to a classical oscillator with external periodic excitation. If a photon of the electric field with energy $\hbar\omega$ is resonantly absorbed by a tunneling system in the ground state with an energy splitting of $E = \hbar\omega_0$ the system transitions into the excited state. In the case that the tunneling system was already in the excited state stimulated emission causes it to de-excite into the ground state by emitting a photon.
The frequency dependency of the linear susceptibility thereby follows a typical resonant behaviour as depicted in figure 2.13. For frequencies smaller than the resonance frequency of the energy transition the system can follow the electric field in phase only weakly. When the frequency is increased to $\omega = \omega_0$ the out-of-phase contribution $b''(\omega, \omega_0)$ reaches its maximal value, since the polarisation is 90° out of phase. Hence the in-phase contribution $b'(\omega, \omega_0)$ is vanishingly small when the field frequency exactly matches the resonance condition. For higher frequencies $\omega > \omega_0$ the phase difference increases even more which leads to a change of sign in the in-phase component of the frequency dependency and the corresponding decrease in the out-of-phase component. The position of the two extremes in $b'(\omega, \omega_0)$ and respectively the width of $b''(\omega, \omega_0)$ is directly related to the relaxation time scale τ_2.
It can also be seen that effects due to saturation mainly influence the out-of-phase contributions to the electric susceptibility. For a distribution of tunneling systems the responsible factor R_{Sat} would diminish positive and negative contributions of $b'(\omega, \omega_0)$ equally, whereas $b''(\omega, \omega_0)$ would effectively be decreased.

2.3.6 Rabi oscillations

A two-level system which interacts with an external periodic driving field can be described by Rabi oscillations. For two states with $\mathcal{H}_{0,\mathrm{Rabi}} |\Psi_1\rangle = E_1 |\Psi_1\rangle$ (lower state) and $\mathcal{H}_{0,\mathrm{Rabi}} |\Psi_2\rangle = E_2 |\Psi_2\rangle$ (upper state) the commonly used Hamiltonian can be expressed by

$$\mathcal{H}_{\mathrm{Rabi}} = \mathcal{H}_{0,\mathrm{Rabi}} + \mathcal{H}_{\mathrm{per,Rabi}} = \begin{pmatrix} E_1 & 0 \\ 0 & E_2 \end{pmatrix} + \begin{pmatrix} 0 & -\hbar\Omega_\mathrm{R} \\ -\hbar\Omega_\mathrm{R} & 0 \end{pmatrix} \cos(\omega t) \tag{2.73}$$

where Ω_R denotes the Rabi frequency. By solving the time dependent Schrödinger equation for this problem the prefactors $c_1(t)$ and $c_2(t)$ for an ansatz of

$$|\Psi_{\mathrm{Rabi}}\rangle = c_1(t) e^{-i\frac{E_1 t}{\hbar}} |\Psi_1\rangle + c_2(t) e^{-i\frac{E_2 t}{\hbar}} |\Psi_2\rangle \tag{2.74}$$

become

$$c_1(t) = \left(\cos\left(\frac{\Omega'_\mathrm{R} t}{2}\right) + i\frac{\delta\omega}{\Omega'_\mathrm{R}} \sin\left(\frac{\Omega'_\mathrm{R} t}{2}\right) \right) e^{-i\frac{\delta\omega t}{\hbar}} \tag{2.75}$$

$$c_2(t) = i\frac{\Omega}{\Omega'_\mathrm{R}} \sin\left(\frac{\Omega'_\mathrm{R} t}{2}\right) e^{i\frac{\delta\omega t}{\hbar}} \tag{2.76}$$

with the detuning frequency $\delta\omega = \frac{|E_2 - E_1|}{\hbar} - \omega$ and the generalized Rabi frequency $\Omega'_\mathrm{R} = \sqrt{\Omega_\mathrm{R}^2 + \delta\omega^2}$. The corresponding probabilities to find the system in a specific state for an initial ground state can easily be derived from this by

$$p_1(t) = |c_1(t)|^2 = \frac{\delta\omega^2}{|\Omega_\mathrm{R}^2 + \delta\omega^2|} + \frac{\Omega_\mathrm{R}^2}{|\Omega_\mathrm{R}^2 + \delta\omega^2|} \cos^2\left(\frac{\Omega'_\mathrm{R} t}{2}\right) \tag{2.77}$$

respectively

$$p_2(t) = |c_2(t)|^2 = \frac{\Omega_\mathrm{R}^2}{|\Omega_\mathrm{R}^2 + \delta\omega^2|} \sin^2\left(\frac{\Omega'_\mathrm{R} t}{2}\right). \tag{2.78}$$

The probability $p_2(t)$ for the two-level system to be in the upper state is depicted in figure 2.14 as a function of time. The probability only reaches unity for a vanishingly small detuning, otherwise its value is lowered due to the Lorentzian shape of the prefactor in equation 2.78. The Rabi frequency thereby describes the transition rate of the two states. For non-zero detuning frequencies Ω_R increases according to the definition of the modified Rabi frequency Ω'_R.

In comparison to the perturbation Hamiltonian of a tunneling system in equation 2.30 the Rabi formalism lacks the energy modulation of the diagonal matrix elements. Only symmetric tunneling systems ($\Delta = 0$) are fully described by the equations above. For the case of asymmetric tunneling systems ($\Delta \neq 0$) the additional term can be attributed to an additional intrinsic non-linearity of the TLS which can be demonstrated by simulations [Mün21]. The Rabi frequency of the tunneling system is therefore generally defined as

$$\Omega_\mathrm{R} = \frac{\Delta_0}{E} \frac{p_\mathrm{eff} F_\mathrm{ac}}{\hbar}. \tag{2.79}$$

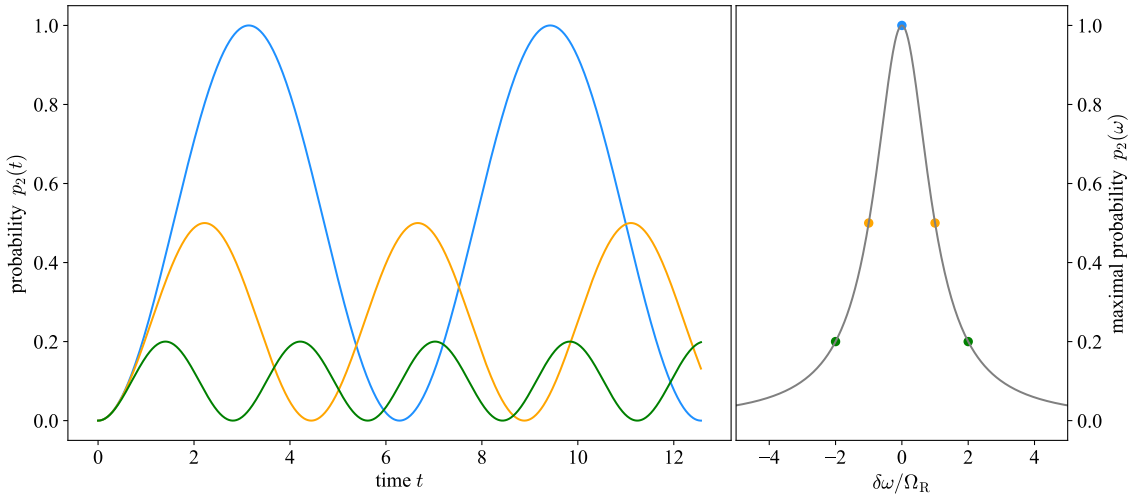

Figure 2.14: Solutions of the Rabi differential equations. The colours represent different detuning with $\delta\omega = 0$ (blue), $\delta\omega = \Omega_R$ (orange) and $\delta\omega = 2\Omega_R$ (green). **Left:** probability to find the two-level system in the excited state plotted over an arbitrary time trace for different detuning. **Right:** line shape function of the maximal probability amplitude for p_2. The higher the detuning from the resonance frequency of the system the smaller is the maximal amplitude of the transition.

2.3.7 Landau-Zener transitions

In contrast to the description of a two-level system as in section 2.3.6, tunneling systems possess additional diagonal matrix elements, which modify the energy splitting according to equation 2.30 as

$$\tilde{E}(t) = E + \delta E_{\mathrm{dia,b}}(t) = E + 2\frac{\Delta}{E} p_{\mathrm{eff}} F_{\mathrm{b}}(t). \tag{2.80}$$

This leads to a different non-equilibrium phenomenon responsible for an enhanced dielectric loss, whenever an additional electric field bias $F_{\mathrm{b}}(t)$ is applied to the tunneling system. It can be described by an avoided level crossing of the systems ground and excited state, for which Landau-Zener transitions [Lan32, Zen32] can occur. The effect was observed for amorphous thin film resonators in bias ramp measurements [Kha14] as well as for continuous periodic bias excitations [Mat19]. Both experiments showed good agreement with the theoretical predictions made by the Landau-Zener-model. Simulations of the tunneling systems Hamiltonian under the influence of different excitation and bias fields [Mün21, Fre21] also coincide with the Landau-Zener formalism.

In order to describe a tunneling system under the influence of a driving field $F(t)$ and an additional bias field $F_{\mathrm{b}}(t)$, the time-dependent Schrödinger equation has to be solved for the Hamiltonian in 2.30 and a general state $|\Psi_{\mathrm{LZ}}\rangle = c_{\mathrm{g}}(t)\,|\Psi_{\mathrm{g}}\rangle + c_{\mathrm{e}}(t)\,|\Psi_{\mathrm{e}}\rangle$. For simplicity the change in energy splitting due to the influence of the driving field

can be neglected since $\tilde{E}(t) \gg 2\frac{\Delta}{E} p_{\mathrm{eff}} F_{\mathrm{ac}}$ holds for most cases. The potential Rabi terms in the case of a continuous bias field can also be ignored, as long as the bias frequency ω_{b} is much smaller than the driving frequency ω. Consequently, the corresponding amplitude of the transition probability as in relation 2.78 would vanish at frequencies of the order of the driving frequency. The differential equations can hence be expressed by

$$i\hbar\dot{c}_{\mathrm{e}}(t) = \frac{\tilde{E}(t)}{2} c_{\mathrm{e}}(t) + \hbar\Omega_{\mathrm{R}}\cos(\omega t) c_{\mathrm{g}}(t) \tag{2.81}$$

$$i\hbar\dot{c}_{\mathrm{g}}(t) = -\frac{\tilde{E}(t)}{2} c_{\mathrm{g}}(t) + \hbar\Omega_{\mathrm{R}}\cos(\omega t) c_{\mathrm{e}}(t), \tag{2.82}$$

which are analogous to the equations in the Landau-Zener problem. An often used definition is hereby the change in energy splitting over time as a bias rate

$$\nu = \frac{1}{\hbar}\frac{d\tilde{E}(t)}{dt} = 2\,\frac{p_{\mathrm{eff}}\dot{F}_{\mathrm{b}}(t)}{\hbar}\sqrt{1-\left(\frac{\Delta_0}{E}\right)^2} \equiv \nu_0\sqrt{1-\left(\frac{\Delta_0}{E}\right)^2}. \tag{2.83}$$

An illustration of the occurring avoided level crossing is depicted in figure 2.15 for an exemplary tunneling system. The energy of the ground and the excited state is thereby modified by the applied bias field. For zero bias the difference between the two states is simply E. The levels also contain the energies for the n photons of the driving field as a constant offset. If the system is in the ground state $|\Psi_{\mathrm{g}}, n\rangle$ and absorbs a photon of energy $\hbar\omega$ it ends up in the excited state $|\Psi_{\mathrm{e}}, n-1\rangle$, which is shown as the dotted line in figure 2.15 (left). At the points where the two states intersect the tunneling system experiences an avoided level crossing with an energy gap in the order of the Rabi frequency Ω_{R}. This is shown in the right illustration of figure 2.15.

For the case of the Landau-Zener problem, there are two possibilities with a different outcome, depending on the biasing rate ν. If the energy is varied slowly in comparison to the frequency of the transition $\nu \ll \Omega_{\mathrm{R}}^2$, a system in the ground state $|\Psi_{\mathrm{g}}, n\rangle$ will undergo an adiabatic transition into the excited state $|\Psi_{\mathrm{e}}, n-1\rangle$ via the absorption of a photon. The opposite process from $|\Psi_{\mathrm{e}}, n-1\rangle$ into $|\Psi_{\mathrm{g}}, n\rangle$ takes place under the emission of a photon. For very high biasing rates $\nu \gg \Omega_{\mathrm{R}}^2$, on the other hand, the system can not exchange energy with the photon field since the change in energy splitting is too fast. This passage without energy exchange is called a Landau-Zener transition.

The solution of the Landau-Zener problem yields the probability for an adiabatic transition from the ground state into the excited state as

$$P_{\mathrm{g}\to\mathrm{e}} = 1 - \exp\left(-\frac{\pi\Omega_{\mathrm{R}}^2}{\nu}\right). \tag{2.84}$$

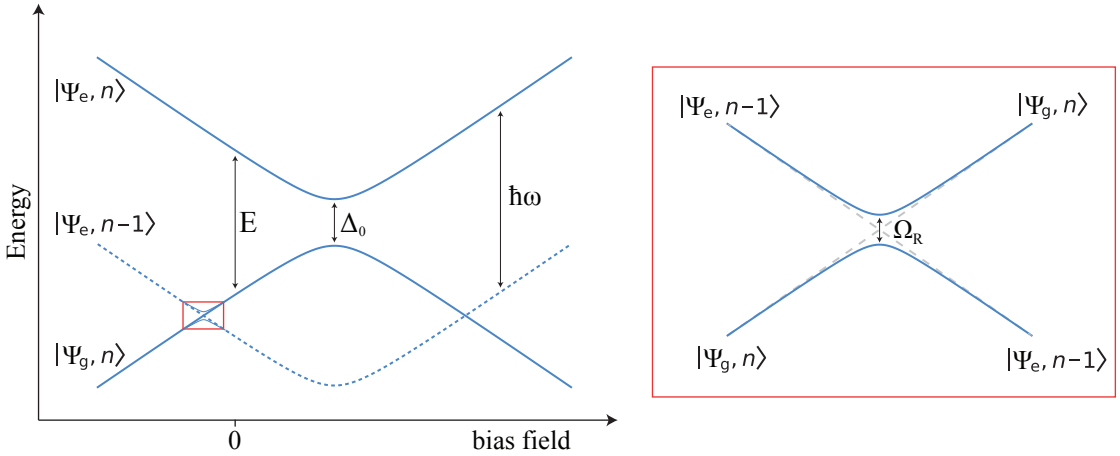

Figure 2.15: Illustration of the Landau-Zener problem. **Left:** energy diagram of a tunneling system together with the n photons of the driving field. If the system absorbs or emits a photon, the energy lines differ by $\hbar\omega$. For $F_\mathrm{b} = 0$ the energy splitting between the ground and the excited state is simply E. The minimal energy splitting $E_\mathrm{min} = \Delta_0$ is reached, when the bias field fully compensates the asymmetry energy Δ. **Right:** enlarged version of the red rectangle on the left. The avoided level crossing gives rise to adiabatic and non-adiabatic passages of the tunneling system dependent on the bias rate ν.

If off-resonant tunneling systems, which are mostly in their ground state, perform this transition via a bias field sweep, the photons of the driving field can be dissipated when out of resonance. This yields a contribution to the dielectric loss, which will be derived in section 2.5.3 for the entire ensemble of tunneling systems.

2.4 Relaxation mechanisms

Similar to the resonant interaction with the photon field, tunneling systems can interact with thermal phonons in the material. This introduces the relaxation time scales τ_1 and τ_2, which are characteristic quantities for dielectric measurement. They are distinguished by the order of their interaction. The longitudinal time scale τ_1 thereby represents the direct interactions with phonons, whereas the transversal time scale τ_2 corresponds to a dephasing of the tunneling systems state due to variations in the environment.

2.4.1 Longitudinal relaxation

Tunneling systems directly interact with the phonon bath via resonant absorption and spontaneous emission. The corresponding transitions are performed by single or multi-phonon processes dependent on the abundance of phonons and thus temperature. Since the number of phonons is small below 1 K, it is sufficient to describe the occurring interactions by one phonon processes. Two phonon processes are also discussed below for completeness, but are only relevant at temperatures above a few Kelvin.

One-phonon process

The derivation of the one-phonon relaxation time scale $\tau_{1\mathrm{P}}$ uses the perturbation Hamiltonian $\hat{\mathcal{H}}_{\mathrm{per}}^{(\mathrm{ph})}$ of the phononic interaction with the tunneling system [Esq98] to calculate the transition rates between the energy levels via Fermi's golden rule [Dir27]. The transition from an initial state $|\Psi_{\mathrm{g}}, \mathbb{1}\rangle$ (TLS in ground state, one phonon) into the final state $\langle\Psi_{\mathrm{e}}, 0|$ (TLS in excited state, no phonon) can therefore be expressed by the rate

$$\Gamma_{\mathrm{g}\to\mathrm{e}} = \int \frac{2\pi}{\hbar} |\langle\Psi_{\mathrm{e}}, 0| \hat{\mathcal{H}}_{\mathrm{per}}^{(\mathrm{ph})} |\Psi_{\mathrm{g}}, \mathbb{1}\rangle|^2 D(E) f(E) \delta(E - \hbar\omega_{\mathrm{ph}}) \,\mathrm{d}E, \tag{2.85}$$

where $D(E)$ denotes the density of phononic states and $f(E)$ the Bose-Einstein distribution. An analogous expression can be found for the rate $\Gamma_{\mathrm{e}\to\mathrm{g}}$ corresponding to the creation of a phonon via the transition from the excited state into the ground state. Therewith, the one-phonon relaxation rate can be calculated by summing $\Gamma_{\mathrm{g}\to\mathrm{e}} - \Gamma_{\mathrm{e}\to\mathrm{g}}$ over all possible phonon modes [Jäc72, Phi87], which yields

$$\tau_{1\mathrm{P}}^{-1} = \left(\frac{\gamma_{\mathrm{l}}^2}{v_{\mathrm{l}}^5} + 2\frac{\gamma_{\mathrm{t}}^2}{v_{\mathrm{t}}^5}\right) \frac{E^3}{2\pi\rho\hbar^4} \left(\frac{\Delta_0}{E}\right)^2 \coth\left(\frac{E}{2k_{\mathrm{B}}T}\right) \tag{2.86}$$

with density ρ of the material. The longitudinal (index l) and the two transversal (index t) phonon branches are described by the elastic deformation potential parameter γ and the sound velocity v. The material specific parameters are often summarized into a factor

$$K_1 = \frac{1}{2\pi\rho\hbar^4}\left(\frac{\gamma_\mathrm{l}^2}{v_\mathrm{l}^5} + 2\frac{\gamma_\mathrm{t}^2}{v_\mathrm{t}^5}\right). \tag{2.87}$$

A detailed derivation of this formula can also be found in [Ang07]. For a constant energy splitting the relaxation time $\tau_{1\mathrm{P}}$ increases with the asymmetry of the tunneling system. The minimal value $\tau_{1,\mathrm{min}}$ is therefore obtained by perfectly symmetric tunneling systems ($\Delta = 0$) and can be used to rewrite equation 2.86 as

$$\tau_{1\mathrm{P}}^{-1} = \tau_{1,\mathrm{min}}^{-1}\left(\frac{\Delta_0}{E}\right)^2. \tag{2.88}$$

Two Phonon process

At higher temperatures the phonon number is increased, which allows the tunneling systems to interact with two phonons simultaneously via a virtual or real third energy level. The corresponding relaxation rate can be expressed as

$$\tau_{2\mathrm{P}}^{-1} = K_2\left(\frac{\Delta_0}{E}\right)^2 T^7 f_{2\mathrm{P}}\left(\frac{E}{2k_\mathrm{B}T}\right)\coth\left(\frac{E}{2k_\mathrm{B}T}\right), \tag{2.89}$$

where K_2, similar to the one-phonon process, represents a material dependent parameter and $f_{2\mathrm{P}}$ a phenomenologically chosen function [Dou80]. At temperatures below 1 K it is sufficient to approximate the longitudinal relaxation time scale τ_1 with one-phonon processes. At higher temperatures two-phonon processes have to be taken into account and the total relaxation rate is described by

$$\tau_1^{-1} = \tau_{1\mathrm{P}}^{-1} + \tau_{2\mathrm{P}}^{-1}. \tag{2.90}$$

2.4.2 Transversal relaxation

Besides the already discussed direct process, tunneling systems can indirectly exchange energy with their environment via strain or dipole field interactions. The basic idea behind this mechanism is described by the theory of spectral diffusion. The model was originally developed to describe the decay rates of spin echoes [Kla62] and later polarisation echoes [Bla77] from experiments on amorphous materials. A tunneling system, which interacts with an electric or strain field, is surrounded by many off-resonant tunneling systems not affected by the excitation. This assumption

is reasonable since the total number of tunneling systems is many orders of magnitude larger than the number of tunneling systems, which are resonantly excited by the field. These off-resonant systems continue to perform thermal transitions according to their longitudinal relaxation rate τ_1. This induces slight changes in the local strain field, respectively in the dipole orientation. The transitions of the surrounding tunneling systems can therefore alter the field at the site of the resonant system. Similar to the bias interaction, a single transition changes the asymmetry energy Δ and thereby the energy splitting E of a tunneling system i. The change in energy can hence be expressed by a sum over all interacting tunneling systems j in the surrounding environment as

$$\delta E_i = \frac{\Delta_i}{E_i} \sum_j \frac{\Delta_j}{E_j} U_{ij} R_{z,j}, \tag{2.91}$$

where $R_{z,j}$ represents the z-components from the Bloch vectors and U_{ij} the factor for the interaction strength between the two systems. The often used interaction constant U_0 is thereby defined as an average value of the interaction strength. Multiple transitions in the surrounding environment lead to a random-walk-like broadening for the expectation value of the tunneling systems energy over time. This property is expressed in [Bla77] by the diffusion kernel

$$D(\omega - \omega_0, t) = \frac{1}{\pi} \frac{\Delta\omega(t)}{(\omega - \omega_0)^2 + \Delta\omega(t)^2}, \tag{2.92}$$

which represents the probability to find a tunneling system with energy $\hbar\omega_0$ at a different frequency ω after the time t. The width of the Lorentzian distribution is increased with time and thus defines a time scale for the loss of phase coherence. In the short time limit $t < \tau_{1,\mathrm{min}} < \tau_1$ the dephasing rate [Bur18] of the tunneling system can be expressed by

$$\tau_\phi^{-1} = \sqrt{\frac{\pi}{24} \frac{P_0 U_0 k_\mathrm{B} T}{\hbar \tau_{1\mathrm{P}}}}. \tag{2.93}$$

For later times, the dephasing rate is expected to decrease in a crossover region and again in a long-time limit [Bla77]. Detailed descriptions of this quantity often depend strongly on the time interval and the experimental setup itself. The total transversal relaxation rate can be written as

$$\tau_2^{-1} = 2\tau_1^{-1} + \tau_\phi^{-1}. \tag{2.94}$$

2.5 Relations for the entire ensemble

Section 2.3 introduced the formal definition of a single tunneling system, described its properties for the interaction with an external field excitation and derived equations in order to characterize its response in the context of a macroscopic quantity in a dielectric measurement. This section will utilize these relations to deduce a description for the temperature dependency and the saturation effects of the entire ensemble.

2.5.1 Temperature dependency

In order to derive the dielectric function for the entire ensemble, the contributions for the individual tunneling systems have to be integrated over their defining parameters with the distribution function from section 2.3.2. This yields the real and the imaginary parts, which consist of their relaxation and resonant contributions as derived in section 2.3.5.
The relations also contain the effective dipole moment p_{eff} of the tunneling system. To include different orientations of the total dipole moment p to the direction of the applied electrical field, the average value of p_{eff}^2 can be calculated as an integration over the polar angles

$$\langle p_{\mathrm{eff}}^2 \rangle = \frac{\int_0^{2\pi} \int_0^{\pi} p^2 \cos(\theta)^2 \sin(\theta) \mathrm{d}\theta \mathrm{d}\varphi}{\int_0^{2\pi} \int_0^{\pi} \sin(\theta) \mathrm{d}\theta \mathrm{d}\varphi} = \frac{1}{3} p^2. \tag{2.95}$$

Total contribution to the real part

The real part of the dielectric function is often described by the relative change of permittivity. This quantity is useful since the total permittivity consists of different contributions, of which the tunneling systems make up only a small fraction. The other contributions can be assumed as constants in the observed temperature regime below 1 K. The relative change of permittivity can therefore be expressed by the susceptibility as

$$\frac{\delta \varepsilon'}{\varepsilon'} = \frac{\delta \chi'}{1 + \chi'}. \tag{2.96}$$

This change in susceptibility can thereby be derived by an integration over the single tunneling system contributions from equations 2.62 and 2.69 as

$$\frac{\delta \varepsilon'}{\varepsilon'} = \frac{1}{1 + \chi'} \int_{\Delta_{0,\mathrm{min}}}^{E_{\mathrm{max}}} \int_{\Delta_{0,\mathrm{min}}}^{E} \left(\chi'_{\mathrm{rel}} + \chi'_{\mathrm{res}} \right) P(E, \Delta_0) \, \mathrm{d}\Delta_0 \, \mathrm{d}E, \tag{2.97}$$

where the change of the total relative permittivity $\varepsilon_{\mathrm{r}} = 1 + \chi$ is assumed to be insignificant under the variation of the parameters and can hence be treated as constant.

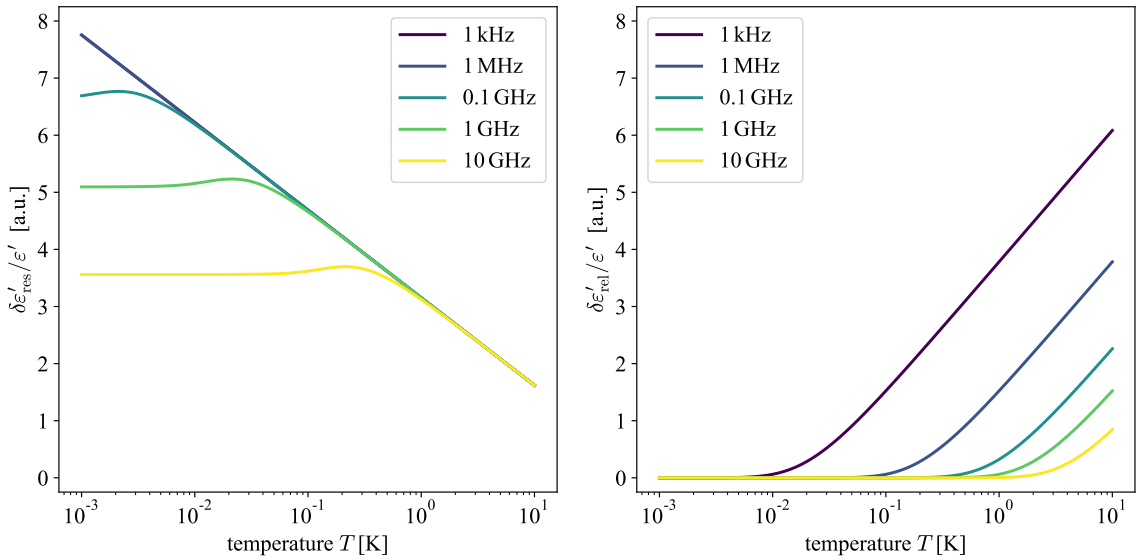

Figure 2.16: Individual contributions to the relative change in permittivity in dependency of the temperature are plotted for different excitation frequencies ω of the applied field. **Left:** the resonant contribution increases for low temperatures as more tunneling systems are in the ground state. **Right:** the relaxation contribution decreases for low temperatures since less phonons are available for this process.

The temperature dependency can now be calculated by a numerical integration of the expression above. The relative change in permittivity can be divided into a relaxation component

$$\frac{\delta\varepsilon'_{\mathrm{rel}}}{\varepsilon'} = \frac{p^2 P_0}{3\varepsilon_0\varepsilon_{\mathrm{r}}}\frac{1}{k_{\mathrm{B}}T}\int_{\Delta_{0,\mathrm{min}}}^{E_{\mathrm{max}}}\int_{\Delta_{0,\mathrm{min}}}^{E}\frac{\sqrt{E^2-\Delta_0^2}}{E\Delta_0}\,\mathrm{sech}^2\left(\frac{E}{2k_{\mathrm{B}}T}\right)a'(\omega)\,\mathrm{d}\Delta_0\,\mathrm{d}E \tag{2.98}$$

and a resonant component

$$\frac{\delta\varepsilon'_{\mathrm{res}}}{\varepsilon'} = \frac{p^2 P_0}{3\varepsilon_0\varepsilon_{\mathrm{r}}}\frac{1}{\hbar}\int_{\Delta_{0,\mathrm{min}}}^{E_{\mathrm{max}}}\int_{\Delta_{0,\mathrm{min}}}^{E}\frac{\Delta_0}{E}\frac{1}{\sqrt{E^2-\Delta_0^2}}\,\tau_2\,R_{\mathrm{Sat}}(E,T)\,b'(\omega,\omega_0)\,\mathrm{d}\Delta_0\,\mathrm{d}E \tag{2.99}$$

with $\omega_0 = E/\hbar$. The dependence over temperature is shown in figure 2.16 for the individual contributions of the relaxation and resonant processes. At high temperatures, the thermal phonon number is large and the relaxation time scale τ_1 is short. This allows systems to follow the external field and to contribute via relaxation processes. For higher frequencies of the applied excitation, however, tunneling systems start to dephase when $\omega\tau_1 \lesssim 1$ according to $a'(\omega)$ and the contribution to the permittivity is therefore reduced. The occupation difference on the other hand vanishes for systems with $E \ll k_{\mathrm{B}}T$, which suppresses resonant processes according to the dependency of the saturation parameter $R_{\mathrm{Sat}}(E,T)$. With decreasing temperature tunneling systems with an energy of $E > k_{\mathrm{B}}T$ are primarily in their ground state and therefore

positively contribute to the resonant permittivity according to $b'(\omega, \omega_0)$. When the temperature reaches the energy scale of the excitation frequency $T \approx \hbar\omega/k_\mathrm{B}$, tunneling systems with a negative contribution to the permittivity contribute as well. For tunneling systems with even lower energy splitting, the contributions are vanishingly small and thus level off into a plateau. The permittivity caused by relaxation processes dies out for decreasing temperatures since the phonon number is reduced and the relaxation time scale τ_1 increases.

Total contribution to the loss

The out-of-phase components responsible for dissipation are usually described by the dielectric loss. This quantity can be expressed by the dielectric susceptibility as

$$\tan\delta = \frac{\varepsilon''}{\varepsilon'} = \frac{\chi''}{1+\chi'}. \tag{2.100}$$

The loss can thereby be derived analogous to the real part by an integration over the individual tunneling system contributions from equations 2.64 and 2.71 as

$$\tan\delta = \frac{1}{1+\chi'} \int_{\Delta_{0,\min}}^{E_\mathrm{max}} \int_{\Delta_{0,\min}}^{E} \left(\chi''_\mathrm{rel} + \chi''_\mathrm{res}\right) P(E, \Delta_0)\, \mathrm{d}\Delta_0\, \mathrm{d}E. \tag{2.101}$$

A numerical integration yields the temperature dependency of the dielectric loss with the relaxation component

$$\tan\delta_\mathrm{rel} = \frac{p^2 P_0}{3\varepsilon_0\varepsilon_\mathrm{r}} \frac{1}{k_\mathrm{B}T} \int_{\Delta_{0,\min}}^{E_\mathrm{max}} \int_{\Delta_{0,\min}}^{E} \frac{\sqrt{E^2-\Delta_0^2}}{E\Delta_0} \operatorname{sech}^2\left(\frac{E}{2k_\mathrm{B}T}\right) a''(\omega)\, \mathrm{d}\Delta_0\, \mathrm{d}E \tag{2.102}$$

and the resonant component

$$\tan\delta_\mathrm{res} = \frac{p^2 P_0}{3\varepsilon_0\varepsilon_\mathrm{r}} \frac{1}{\hbar} \int_{\Delta_{0,\min}}^{E_\mathrm{max}} \int_{\Delta_{0,\min}}^{E} \frac{\Delta_0}{E} \frac{1}{\sqrt{E^2-\Delta_0^2}}\, \tau_2\, R_\mathrm{Sat}(E,T)\, b''(\omega,\omega_0)\, \mathrm{d}\Delta_0\, \mathrm{d}E \tag{2.103}$$

The obtained results of these calculations are shown in figure 2.17 for the individual contributions. At low temperatures the dielectric loss is mainly determined by resonant processes. Due to $b''(\omega, \omega_0)$ the small energy bandwidth of the order of τ_2 defines a subset of contributing tunneling systems with $E \sim \hbar\omega$. If the relation $k_\mathrm{B}T \ll E$ holds, these systems are in their ground state and contribute to the resonant component of the loss. This also defines the height of the emerging plateau. For higher temperatures tunneling systems with small energy splitting are thermally saturated first, which decreases the resonant contribution when $k_\mathrm{B}T \sim E$.
The relaxation becomes relevant if tunneling systems fulfil the relation $\omega\tau_1 \sim 1$ due to the Lorentzian shape of $a''(\omega)$. At lower temperatures the relaxation time scale

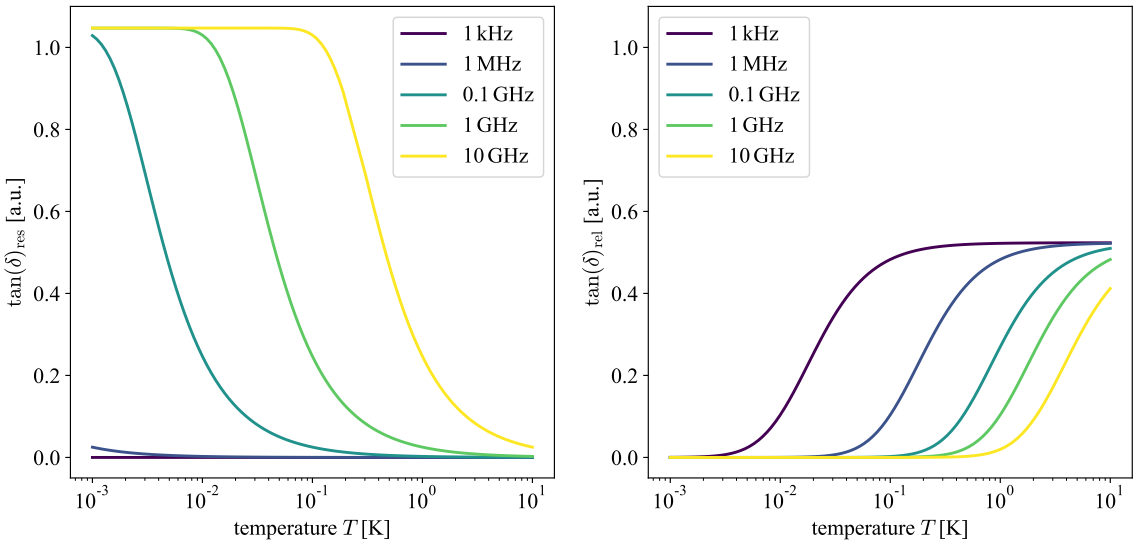

Figure 2.17: Individual contributions to the dielectric loss in dependency of the temperature are plotted for different excitation frequencies ω of the applied field. **Left:** the resonant contribution decreases for higher temperatures as less tunneling systems are in their ground state. **Right:** the relaxation contribution increases for high temperatures due to the increased relaxation rate.

τ_1 is too long and the term of the hyperbolic secant suppresses any contribution to the numeric integral. Hence, the relaxation first becomes apparent for low excitation frequencies of the external field. For even higher temperatures the dielectric loss evens out in a plateau independent of the applied frequency.

2.5.2 Saturation of TLS

The calculations in section 2.5.1 all assume a negligible influence of saturation effects as derived by equation 2.57 for the resonant contributions, so $F_{\mathrm{ac}} \ll F_{\mathrm{c}}$. Since the mechanism of resonant absorption is noticeably affected by the strength of the external field, this section will derive an expression to describe the saturation for an ensemble of tunneling systems in a dielectric material.
The photon number is increased by the strength of the excitation field F_{ac}, which in turn enhances the interaction rate of the tunneling systems with photons. If this rate exceeds the relaxation rate of the two-level system, states created by resonant absorption can be de-excited by stimulated emission before they decay through a relaxation process. The occupation difference therefore becomes zero and both counteracting processes occur equally often. The dielectric material can be understood as transparent in the energy band, where the resonant condition is fulfilled. This effect was already depicted in figure 2.11 for high field excitations. The real part and

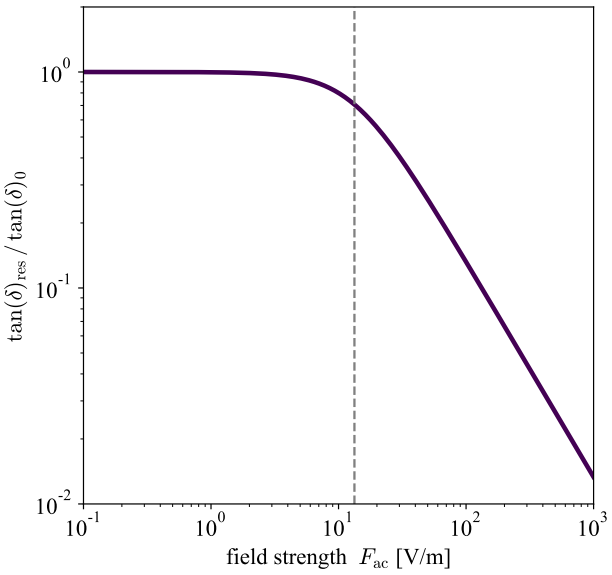

Figure 2.18: Dependency of the resonant loss as a function of the external field excitation F_{ac}. The plot used exemplary values of p =1 D, $\tau_{1,\mathrm{min}}$ =100 µs and τ_2 =5 µs. The resonant loss is decreased around the critical field limit F_{c} (grey dotted line).

the loss of the dielectric function are differently influenced by the saturation. Since the integral for the real part consists of positive and negative components due to the line shape function $b'(\omega, \omega_0)$, saturation effects cancel both contributions almost equally. A deviation can only be observed for very high field excitations. The loss, on the other hand, is significantly influenced by saturation effects. It is reduced via equation 2.57 for a single tunneling system. The total contribution of the ensemble to the dielectric loss can be derived identically to equation 2.103, but as a function of the excitation field F_{ac} for an arbitrary temperature T. This yields the expression

$$\tan\delta_{\mathrm{res}} = \frac{\pi P_0 p^2}{3\varepsilon_0\varepsilon_{\mathrm{r}}} \frac{\tanh\left(\frac{\hbar\omega}{2k_{\mathrm{B}}T}\right)}{\sqrt{1+\left(\frac{F_{\mathrm{ac}}}{F_{\mathrm{c}}}\right)^2}}, \tag{2.104}$$

in which the low power limit for the dielectric loss can be defined as

$$\tan\delta_0 = \frac{\pi P_0 p^2}{3\varepsilon_0\varepsilon_{\mathrm{r}}} \tanh\left(\frac{\hbar\omega}{2k_{\mathrm{B}}T}\right) \tag{2.105}$$

and the critical field limit as

$$\bar{F}_{\mathrm{c}} = \frac{3\hbar}{2p} \frac{1}{\sqrt{\tau_{1,\mathrm{min}}\tau_2}}. \tag{2.106}$$

The equation includes an average over all possible dipole angles θ and provides a good description for the entire ensemble. The dependency of the resonant loss is depicted in figure 2.18 as a function of the applied external field strength F_{ac}. For small field excitations $F_{\mathrm{ac}} \ll \bar{F}_{\mathrm{c}}$ the resonant loss can be approximated with the low power limit from equation 2.105. For values in the order of the critical field limit $\bar{F}_{\mathrm{c}}$

the dielectric loss starts to decrease due to saturation effects. For even higher field strengths $F_{\mathrm{ac}} \gg \bar{F}_{\mathrm{c}}$, the dependency of the resonant loss becomes approximately $\tan\delta_{\mathrm{res}} \sim F_{\mathrm{ac}}^{-1}$ with a convergence towards zero.

Since this effect is especially important for the resonant dielectric loss, a measurement of the temperature dependence as described in section 2.5.1 is also dependent on the of the applied field strength F_{ac}. Figure 2.19 shows the total dielectric loss for different ratios of the applied field strength F_{ac} and the corresponding critical field F_{c}. According to figure 2.18 the resonant loss is reduced above the critical field F_{c} due to the saturation of the tunneling systems. The relaxation contribution is thereby not affected, as well as the contributions to the real part of the dielectric function.

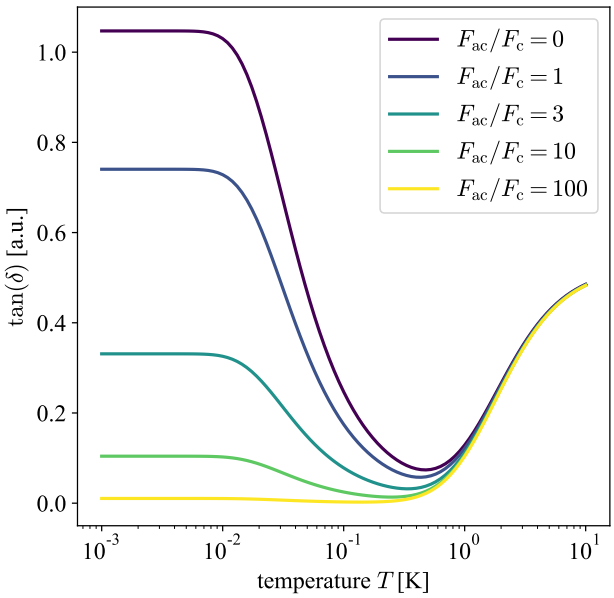

Figure 2.19: Total dielectric loss in dependence on temperature. The plot shows the effect of a strong field excitation on the low temperature resonant loss for different ratios of the field strength F_{ac} to the critical field F_{c}. The contribution is reduced due to the saturation effects of the tunneling systems.

2.5.3 Landau-Zener loss contribution

Section 2.3.7 introduced Landau-Zener transitions as a possible contribution to the dielectric loss, which will be derived in the following for the entire ensemble following [Kha13]. The total dissipated energy $\mathrm{d}\mathcal{E}$ can thereby be expressed by an integral over the dielectric sample V and the number of tunneling systems N that perform an adiabatic passage during the time interval $\mathrm{d}t$. The term reads

$$\mathrm{d}\mathcal{E} = \int \mathrm{d}V \int \mathrm{d}N\hbar\omega P_{\mathrm{g}\to\mathrm{e}}, \tag{2.107}$$

where $P_{\mathrm{g}\to\mathrm{e}}$ is the transition probability from equation 2.84. All systems are hereby assumed to be in the ground state, which corresponds to a vanishingly small tem-

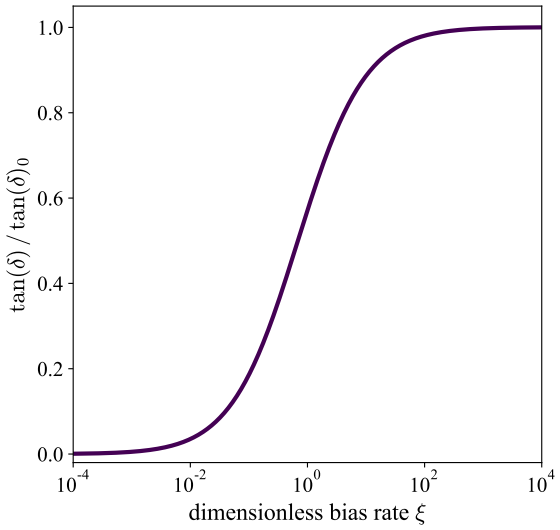

Figure 2.20: Numerical integration for the total dielectric loss in relation to the low power limit $\tan(\delta)_0$ in dependence of the dimensionless bias rate ξ. The low power limit is restored if the bias rate is increased, even if the systems would be saturated in their steady state limit without a bias field.

perature. The dielectric loss is connected to the dissipated power P_{dis} via the total energy stored in the capacitor $W_{\mathrm{tot}} = \varepsilon_0 \varepsilon_{\mathrm{r}} F_{\mathrm{ac}}^2 V$ as

$$\tan\delta = \frac{P_{\mathrm{dis}}}{\omega W_{\mathrm{tot}}} = \frac{\mathrm{d}\mathcal{E}/\mathrm{d}t}{\omega W_{\mathrm{tot}}}. \tag{2.108}$$

Following this approach leads to an expression for the dielectric loss

$$\tan\delta = \frac{\pi P_0 p^2}{\varepsilon_0 \varepsilon_{\mathrm{r}}} \xi \int_0^1 \cos\theta \int_0^1 \left(1 - \exp\left(-\frac{\cos\theta}{\xi} \frac{x^2}{\sqrt{1-x^2}}\right)\right) \frac{\mathrm{d}x}{x} \mathrm{d}(\cos\theta), \tag{2.109}$$

which can be evaluated numerically. The dimensionless bias rate ξ is thereby defined as

$$\xi = \frac{2\nu_0 \hbar^2}{\pi p^2 F_{\mathrm{ac}}^2}. \tag{2.110}$$

The calculation also includes an integration over the dipole angles θ which takes into account their orientation with respect to the direction of the electric field by $p_{\mathrm{eff}} = p\cos\theta$. For very high bias rates $\nu \gg \Omega_{\mathrm{R}}$ the loss matches the low power limit for vanishing temperatures

$$\tan\delta_{0,T\to 0} = \frac{\pi P_0 p^2}{3\varepsilon_0 \varepsilon_{\mathrm{r}}}, \tag{2.111}$$

which matches the relation derived in section 2.5.2 for the fully unsaturated ensemble. The emergence of a plateau can be explained by the sheer number of tunneling system that are swept through the resonance at high bias rates. This compensates the steady decrease in transition probability to a constant value of the integral. The dependency of the Landau-Zener dielectric loss is depicted in figure 2.20 over the dimensionless bias rate ξ. Since these calculations neglect relaxation processes equation 2.109 can not describe the dielectric loss for $\xi \ll (\Omega_{\mathrm{R}}\sqrt{\tau_1\tau_2})^{-1}$. In this regime the bias rate plays a minor role and the dielectric loss is better approximated with the steady

state limit from equation 2.104. The transition between both limits can be described by the crossover rate

$$\xi_1 = \frac{2}{\pi \Omega_{\mathrm{R0}} \tau} \tag{2.112}$$

with $\Omega_{\mathrm{R0}} = \frac{p_{\mathrm{eff}} F_{\mathrm{ac}}}{\hbar}$ and $\tau = \sqrt{\tau_{1,\mathrm{min}} \tau_2}$. In summary, this means that a single low power driving field would only see the low power loss of the dielectric sample. For increasing field strength, the tunneling systems become saturated, which decreases the resonant contribution to the steady state limit according to equation 2.104. The additional application of a bias field would then restore the low power loss limit with increasing values of the corresponding bias rate. This behaviour was experimentally verified by measurements for example in [Kha14, Fre21].

For the case of a periodic bias sweep instead of a single ramp the corresponding systems traverse the region of the avoided crossing several times. They interact multiple times with the excitation field while additionally accumulating a phase, also known as the dynamic phase in between transitions [Stü32], which results in constructive or destructive interference between the individual states. The possibility of a population inversion is thereby restricted due to the associated interference pattern and dependent on the defining system parameters. The effect is referenced as Landau-Zener-Stückelberg (LZS) interferometry [She10, Iva22], which will be introduced in the following section.

2.5.4 Continuous biasing effects

A continuous bias field can be understood as a periodic modulation of the TLS‘s asymmetry energy and therefore its energy splitting. In principle every periodic function can be used to bias the TLS-ensemble but an obvious choice would be a sinusoidal function to create a discrete bias frequency f_{b} or a triangular signal in order to achieve a constant bias rate. During this modulation a subset of TLSs cross the frequency region of the driving field multiple times and the corresponding systems are therefore repeatedly interacting with the excitation field. The bias frequency f_{b} and the relaxation time scale τ_1 are hereby the two defining parameters that divide this scenario into two different cases. For $1/f_{\mathrm{b}} \gg \tau_1$ the TLS can relax to the ground state after each interaction. Each transition can hence be treated individually with the formalism presented above. For $1/f_{\mathrm{b}} \ll \tau_1$, which will be referred to later as the coherent regime, consecutive crossings are dependent on each other. The acquired phase becomes important and leads to interference effects between multiple transitions. As a result constructive or destructive interference can excite off-resonant TLS or respectively hold them in their ground state during multiple passages. Figure 2.21 shows a simulation of this effect from [Bli22] for two

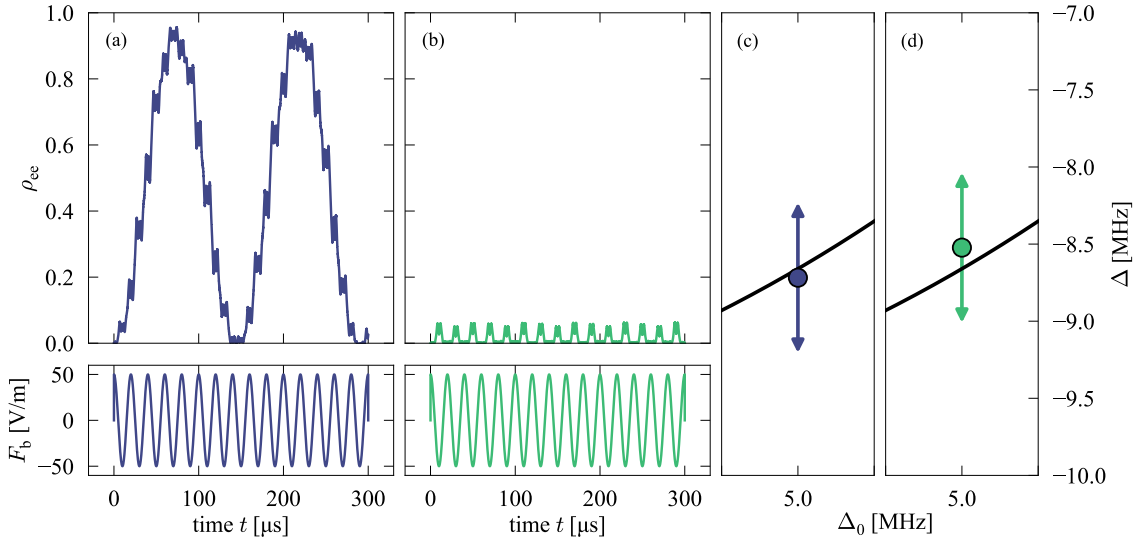

Figure 2.21: Numerical calculation from [Bli22] of the excitation probability ρ_{ee} for two continuously biased TLS. Both systems have $\Delta_0 = 5\,\mathrm{MHz}$ but differ slightly in asymmetry energy with $\Delta(F_b = 0) = -8.718\,\mathrm{MHz}$ (blue) respectively $\Delta(F_b = 0) = -8.523\,\mathrm{MHz}$ (green). The illustrations in (a) and (b) show the occurring constructive, respectively destructive, interference, whereas (c) and (d) clarify their position in the Δ-Δ_0-plane with the corresponding maximal bias shift. Adapted from [Bli22].

systems both with $\Delta_0 = 5\,\mathrm{MHz}$ and $\Delta(F_b = 0) = -8.718\,\mathrm{MHz}$ (blue) respectively $\Delta(F_b = 0) = -8.523\,\mathrm{MHz}$ (green), which are biased by a sinusoidal field $F_b(t) = F_b \cos(2\pi f_b t)$ of amplitude $F_b = 50\,\mathrm{V/m}$ and frequency $f_b = 50\,\mathrm{kHz}$. This shows that a slight variation of the systems parameters drastically change the behaviour of individual TLSs under the continuous bias field. The dark blue system experiences a stepwise Rabi-like oscillation due to the constructive interference from multiple passages of the excitation field. The green system, on the other hand, stays in the ground state since destructive interference prevents an excitation during the crossings. This exemplary scenario does not include relaxation processes for the individual systems. A more detailed discussion can be found in [Bli22].
In literature this effect is referred to as LZS interferometry [She10, Iva22]. The calculations thereby yield the condition for photon absorption of TLSs in the non-adiabatic limit as

$$\delta E_0 = |\sqrt{\Delta_0^2 + \Delta^2(F_b = 0)} - \hbar\omega| = k \cdot h f_b, \quad k \in \mathbb{Z}. \tag{2.113}$$

This condition can be interpreted as a k-photon resonance of the TLSs with the specific set of defining parameters Δ_0 and $\Delta(F_b = 0)$. The interaction involves k bias photons together with the driving field to perform the transition according to $\omega = \omega_0 + k \cdot \omega_b$. For a better understanding figure 2.22 shows the time averaged occupation probability $\bar{\rho}_{ee}$ to find the corresponding systems in the excited state after

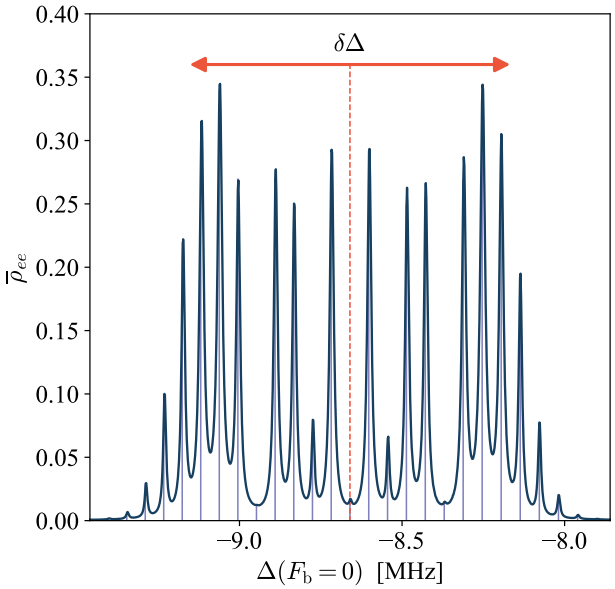

Figure 2.22: Time averaged occupation probability $\bar{\rho}_{\mathrm{ee}}$ for various TLS with $\Delta_0 = 5\,\mathrm{MHz}$ but different values for $\Delta(F_\mathrm{b} = 0)$. The vertical blue lines illustrate the expected positions for the k-photon resonances. The horizontal red arrow indicates the maximal modulation $\delta\Delta$. Adapted from [Bli22].

multiple passages, which in this case include relaxation processes. The k-photon resonances (vertical lines) can be observed according to equation 2.113 in dependence of the initial asymmetry energy $\Delta(F_\mathrm{b} = 0)$ and for a constant tunneling splitting Δ_0. The constructive interference effect can only occur in the frequency band of width $\delta\Delta$ around the excitation frequency (vertical red line). The horizontal red arrow thereby indicates the maximal modulation $\delta\Delta = 2p_{\mathrm{eff}}\,F_\mathrm{b}$ in dependence on the bias field strength. For systems outside of this range the interaction probability is reduced since the shift in asymmetry energy is not large enough to reach the resonance of the excitation field. Some of these peaks are very small $k = \{0, \pm 5\}$. This effect is often referred to as the *coherent destruction of interference*, which is caused by very slow frequencies of the Rabi-like oscillations. This prevents an excitation of the corresponding systems in a sensible amount of time and therefore the occurrence of a resonance. These k-photon resonance peaks can also be linked to the non-linear behaviour of TLSs with the appearance of intermodulation products in the frequency band, which were already observed in numerical simulations in [Mün21].
A treatment including relaxation processes was also done in [Mat19] for the coherent evolution of n resonant passages. Their calculations assumed relaxation after $m = \tau_1 f_\mathrm{b}$ coherent transitions. The thereby derived second critical bias rate

$$\xi_2 = \frac{8\,p\,F_\mathrm{b}}{\pi\hbar\Omega_{\mathrm{R0}}^2\tau_1} \tag{2.114}$$

defines the limit, in which the ensemble transitions from the picture of the single sweep formalism to the coherent regime.
From figure 2.22 it can also be understood that a significant difference exists between the increase of bias field strength and bias frequency. With higher values of F_b the

area of interacting systems is broadened with $\delta\Delta$, which increases the total contribution of the ensemble, for example to the dielectric loss. Higher bias frequencies, on the other hand, widen the distance between individual k-photon resonances. The total contribution to the loss is therefore even reduced for an increase of the bias frequency in the coherent regime as shown in [Bli22]. This condition ($h f_\mathrm{b} > p\, F_\mathrm{b}$) can be translated into the third critical bias rate

$$\xi_3 = \frac{F_\mathrm{b}^2}{F_\mathrm{ac}^2}, \tag{2.115}$$

which indicates the return of the dielectric loss from the coherent regime back to the saturation limit. A full evaluation can be found in [Bli22] with a numerical simulation of the TLS dynamics and the corresponding experimental observations.

2.6 Resonators

Resonant systems are applied to almost every field of physics for either the realisation of experimental setups or the theoretical description of the thereby observed phenomena. This section provides a theoretical description of a transmission line resonator and an introduction in the formalism of a non-linear Duffing oscillator, which are essential for the understanding of the following chapters.

2.6.1 Equation of motion for microwave resonators

The experimental setup of this thesis uses microelectronic absorption-type resonators inductively coupled to a transmission line. In the simplest case such a system consists of a capacitance C and an inductance L as schematically illustrated in figure 2.23. They can be described by the formalism of a quantum mechanical harmonic oscillator with a Hamiltonian of

$$\mathcal{H}_\mathrm{r} = \hbar\omega_\mathrm{r}\left(\hat{a}^\dagger(t)\hat{a}(t) + \frac{1}{2}\right), \tag{2.116}$$

where ω_r defines the resonance frequency of the system. The creation $\hat{a}^\dagger(t)$ and annihilation operator $\hat{a}(t)$ are thereby the characterising quantum mechanical system operators, which can be used to derive the classical properties associated with the resonator system. The electric and magnetic fields for example are related to the system operators via

$$E(t) \sim (\hat{a}(t) + \hat{a}^\dagger(t)) \quad \text{and} \quad B(t) \sim i\,(\hat{a}(t) - \hat{a}^\dagger(t)). \tag{2.117}$$

The resonator can be described by the linear Heisenberg equation of motion

$$i\hbar\frac{\partial}{\partial t}\hat{a}(t) = [\hat{a}(t),\mathcal{H}_\mathrm{r}], \tag{2.118}$$

which can be rewritten as

$$\frac{\partial}{\partial t}\hat{a}(t) = i\omega_\mathrm{r}\hat{a}(t) \tag{2.119}$$

using the canonical commutation relations of the system operators. An analogous equation follows for the adjoint creation operator $\hat{a}^\dagger(t)$. The coupling to the environment via the transmission line and the implementation of a channel for intrinsic losses adds additional terms to equation 2.119 resulting in

$$\dot{\hat{a}}(t) = i\omega_\mathrm{r}\,\hat{a}(t) - (\kappa_\mathrm{i} + \kappa_\mathrm{c})\,\hat{a}(t) + \sqrt{\kappa_\mathrm{c}}\,\hat{b}_\mathrm{in}(t). \tag{2.120}$$

The quantity $\hat{b}_\mathrm{in}(t)$ thereby represents an external excitation via the transmission line. A similar equation is found for the creation operator $\hat{a}^\dagger$, but since it describes the same system properties it is sufficient to focus on equation 2.120 for the derivation.

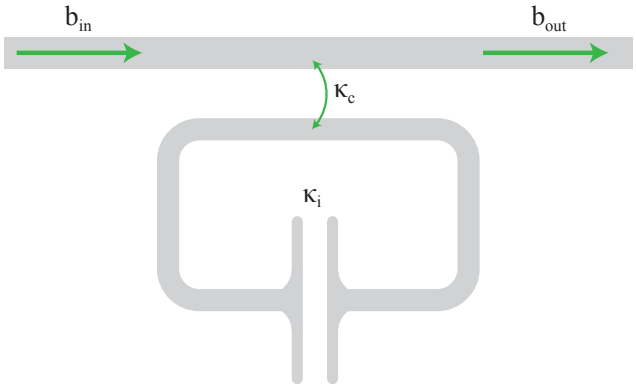

Figure 2.23: Schematic illustration of an absorption type LC-resonator inductively coupled to a transmission line. The systems possess a loss rate due to coupling κ_c and to internal losses κ_i. The resonator is excited with a drive tone $\hat{b}_\mathrm{in}$, which is reduced through the resonators coupling to the output field $\hat{b}_\mathrm{out}$.

The photons of the signal couple into the inductor with the corresponding loss rate κ_c. While inside the resonator, the amplitude of the system operator is reduced via internal losses κ_i and the coupling of photons to the transmission line κ_c. These parameters are also used to define the coupling coefficient

$$\eta_\mathrm{c} = \frac{\kappa_\mathrm{c}}{\kappa_\mathrm{i} + \kappa_\mathrm{c}}, \tag{2.121}$$

which can be used to quantify the distribution between internal and external losses. If $\eta_\mathrm{c} < 0.5$, the total loss is mostly dominated by the internal properties, which is why the resonator is called undercoupled. For an over-coupled system $\eta_\mathrm{c} > 0.5$ the losses are mainly determined by the coupling to the transmission line and the internal losses are not as important. A steady state solution for equation 2.120 can be found by an ansatz of $\hat{a}(t) = \hat{a}e^{i\omega t}$, $\hat{a} \in \mathbb{R}$, for the applied drive tone of $\hat{b}_\mathrm{in}(t) = \hat{b}_\mathrm{in}e^{i\omega t}$, $\hat{b}_\mathrm{in} \in \mathbb{C}$ [Nat17]. The substitution into equation 2.120 yields the expression

$$\dot{\hat{a}} = -(i(\omega - \omega_\mathrm{r}) + (\kappa_\mathrm{i} + \kappa_\mathrm{c}))\hat{a} + \sqrt{\kappa_\mathrm{c}}\,\hat{b}_\mathrm{in}, \tag{2.122}$$

for which $\dot{\hat{a}} = 0$ can be assumed to obtain a steady state solution. The amplitude is thereby derived as

$$\hat{a}(\omega) = \frac{\sqrt{\kappa}_\mathrm{c}}{(\kappa_\mathrm{i} + \kappa_\mathrm{c}) + i(\omega - \omega_\mathrm{r})} \tag{2.123}$$

and the corresponding phase shift between the input signal and the resonator field as

$$\varphi_\mathrm{a}(\omega) = -\arctan\left(\frac{(\omega - \omega_\mathrm{r})}{(\kappa_\mathrm{i} + \kappa_\mathrm{c})}\right). \tag{2.124}$$

In a measurement setup as in figure 2.23, the resonator is often described by the transmission parameter S_{21}, which compares the input field of the external excitation $\hat{b}_\mathrm{in}$ with the output field $\hat{b}_\mathrm{out}$. The corresponding value can be calculated using

$$\hat{b}_\mathrm{out}(\omega) = \hat{b}_\mathrm{in}(\omega) - \sqrt{\kappa_\mathrm{c}}\,\hat{a}(\omega) \tag{2.125}$$

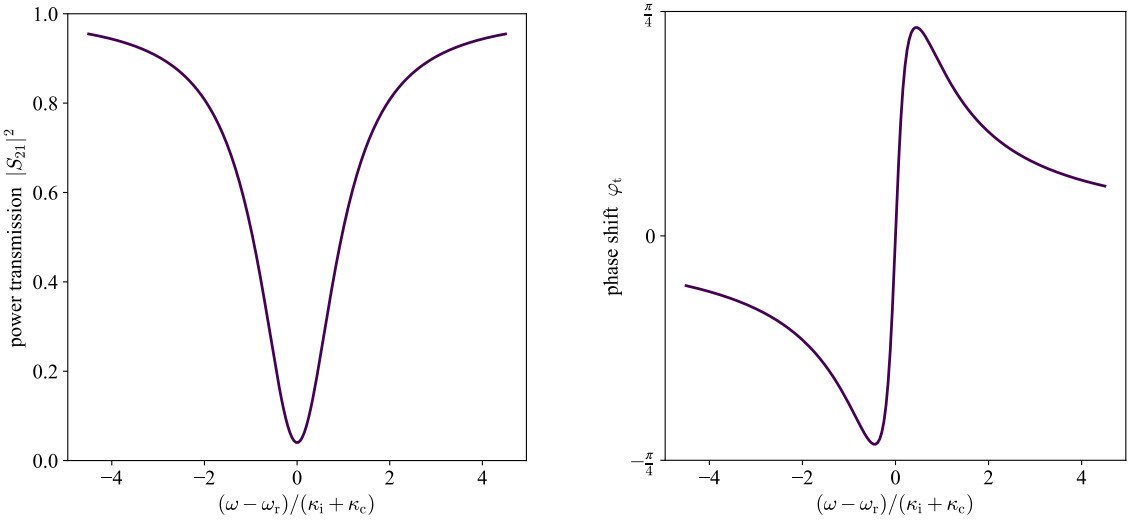

Figure 2.24: Transmission response of an absorption type resonator. Power transmission $|S_{21}|^2$ (**left**) and phase shift φ_t (**rigth**) as a function of the absolute change in resonance frequency normalized to the total loss.

and the expression for $\hat{a}(\omega)$ from equation 2.123, which yields

$$S_{21}(\omega) = \frac{\hat{b}_{\text{out}}(\omega)}{\hat{b}_{\text{in}}(\omega)} = 1 - \frac{\kappa_c}{(\kappa_i + \kappa_c) + i(\omega - \omega_r)}. \tag{2.126}$$

The phase shift between the output and the input field can be expressed as

$$\varphi_t(\omega) = \arctan\left(\frac{\kappa_c(\omega - \omega_r)}{\kappa_i(\kappa_i + \kappa_c) + (\omega - \omega_r)^2}\right). \tag{2.127}$$

This is a result of the resonator field coupling back into the transmission line according to equation 2.125 and interfering with the external field excitation $\hat{b}_{\text{out}}$. The associated behaviour is depicted in figure 2.24 for the power transmission $|S_{21}|^2$ and the phase shift φ_t of an absorption type resonator. For strongly detuned excitation frequencies the external field passes through the transmission line without any significant absorption of the resonator. The transmission parameter is thereby negligibly reduced and the phase is shifted only slightly. Near the resonance frequency the field amplitude of the outgoing component is decreased by the absorption of the associated loss mechanisms of the system. The phase shift is determined by the overlap of the initial excitation with the resonator field coupled back into the transmission line. At resonance the absorption is maximal and the phase shift vanishes.

2.6.2 Non-linear Duffing oscillator

The harmonic oscillator potential is a valuable approximation for most resonant systems at sufficiently small excitations. Above a certain threshold, however, many

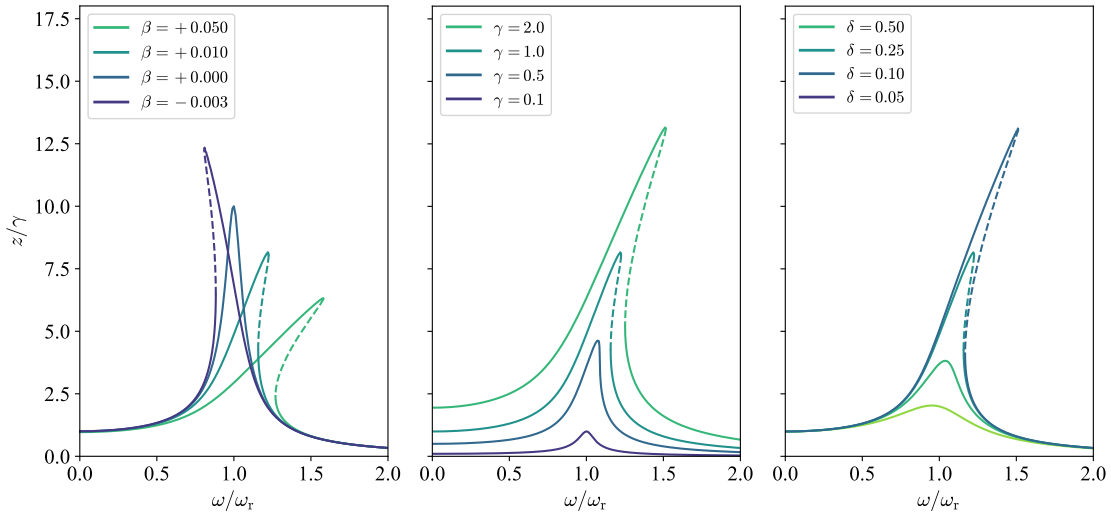

Figure 2.25: Solutions for the Duffing response equation for different system parameter sets. The dependence of the oscillation amplitude z is plotted over frequency for different values of the non-linearity factor β (**left**), the amplitude of the external field excitation γ (**middle**) and the damping parameter δ (**right**). If the corresponding quantity is not otherwise indicated in the plots, the remaining parameters were chosen as $\beta = 0.01$, $\gamma = 1$ and $\delta = 0.1$.

of these systems show anharmonicities in their potential, which are responsible for occurring non-linear effects. This section therefore describes the properties of the Duffing oscillator [Duf18] as an exemplary system. This type of resonator can be described by a non-linear second-order differential equation, which reads

$$\ddot{x} + \delta\dot{x} + \omega_r^2 x + \beta x^3 = \gamma\cos(\omega t). \tag{2.128}$$

The quantity δ thereby describes the damping of the system, ω_r its resonance frequency in the harmonic limit, β the non-linearity factor and γ the amplitude of the external driving field. The solution for the frequency response of a steady state can be found by applying the harmonic balance method [Jor07], which leads to an implicit function for the oscillation amplitude z in the form of

$$\left(\left(\omega^2 - \omega_r^2 - \frac{3}{4}\beta z^2\right)^2 + (\delta\,\omega)^2\right) z^2 = \gamma^2. \tag{2.129}$$

The functional dependency of this equation is depicted in figure 2.25 for an arbitrary set of system parameters. Each picture shows the behaviour for a variation for a specific quantity. The non-linearity factor β changes the prefactor of the anharmonic potential. Contrary to the case of the harmonic oscillator ($\beta = 0$) the Duffing response equation has multiple solutions for a single excitation frequency ω with stable (solid lines) and unstable (dashed lines) equilibrium states. Sweeping

the frequency in the resonator window results in a discontinuous dependence of the amplitude response with a characteristic jump phenomenon, when the two stable solution collapse into a single value. The obtained curve is different for increasing or decreasing values of the excitation field. This behaviour is a consequence of the anharmonic potential and the associated non-linear restoring force. With a non-vanishing value for β the potential transitions from harmonic to anharmonic via a spontaneous symmetry breaking. As a result, the dynamical system of the Duffing resonator displays bifurcation and chaos for a complex evaluation of the systems equation of motion [Guc86]. A more detailed description and further reading on this topic can also be found in [Guc86, Nay95, Pea06, Jor07].

It is worth mentioning that the description of the Duffing resonator shows many parallels to the theoretical formalism used for the two-level system. The Duffing resonators potential is likewise formed by two separate wells. The occurring bifurcation can thereby be linked to the appearance of two separate states with different amplitudes.

2.6.3 Duffing oscillator with two excitation fields

The conducted experiments in this thesis show characteristics similar to the behaviour of a non-linear resonator. In order to understand the obtained data in the following chapters, the theoretical description of the Duffing oscillator is extended by an additional excitation field. The corresponding differential equation reads

$$\ddot{x} + \delta\dot{x} + \omega_\mathrm{r}^2 x + \beta x^3 = \gamma_1 \cos(\omega_1 t) + \gamma_2 \cos(\omega_2 t). \tag{2.130}$$

The analysis of the equation above is thereby intended to describe the case of a strong excitation field represented by the parameters γ_1, ω_1 and a weak probe field with γ_2, ω_2. Similar to the single excitation case, the corresponding implicit functions of the system can be obtained by the harmonic balance method, which yields

$$\gamma_1^2 = z_1^2 \left((\delta\omega_1)^2 + \left(\frac{3}{2}\beta z_2^2 - (\omega_1^2 - \omega_\mathrm{r}^2) + \frac{3}{4}\beta z_1^2 \right)^2 \right) \tag{2.131}$$

and

$$\gamma_2^2 = z_2^2 \left((\delta\omega_2)^2 + \left(\frac{3}{2}\beta z_1^2 - (\omega_2^2 - \omega_\mathrm{r}^2) + \frac{3}{4}\beta z_2^2 \right)^2 \right). \tag{2.132}$$

The oscillation amplitudes z_1 and z_2 thereby represent the response to the individual excitation fields at the associated frequency ω_1 respectively ω_2. A more detailed derivation of these equations can be found in [Din22]. The scenario of interest in this thesis is the application of a fixed frequency for the strong excitation together with

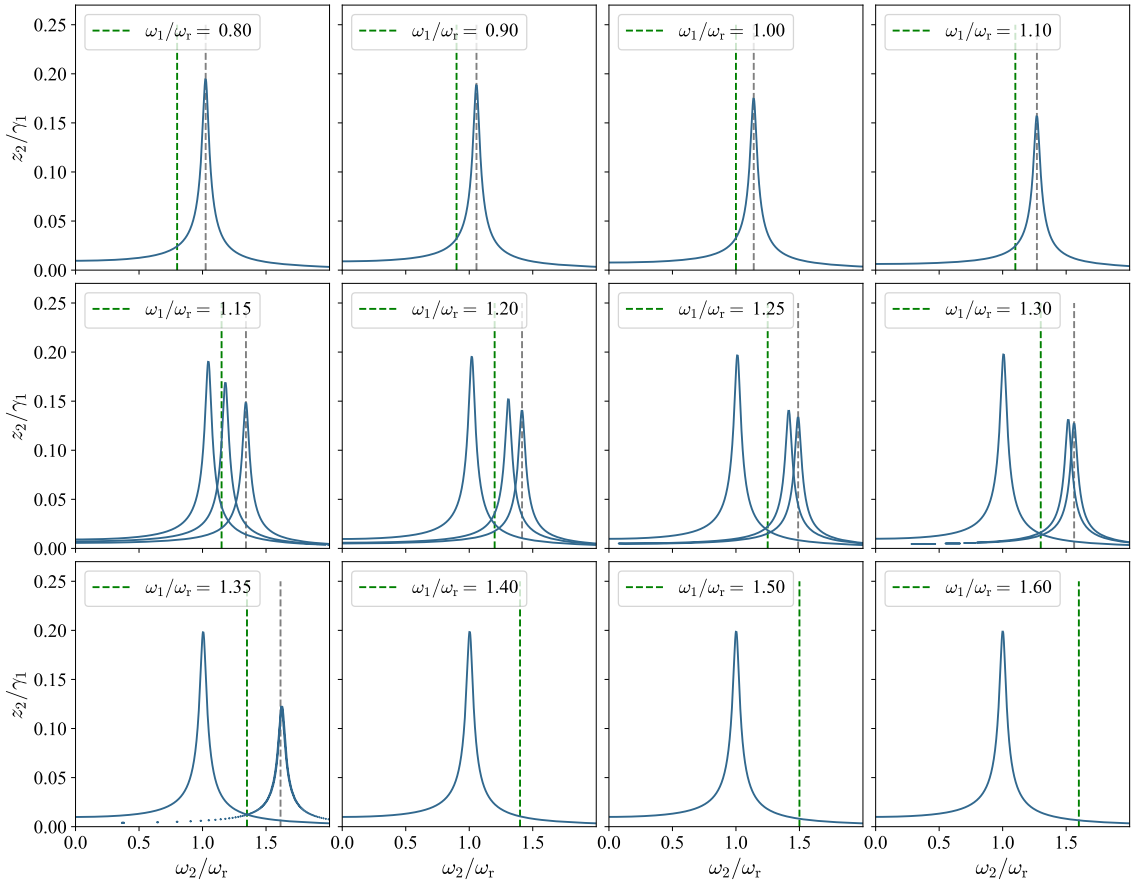

Figure 2.26: Numerical solutions for the oscillation amplitude z_2 in dependence of the probe field frequency ω_2 for different values of the strong excitation field frequency ω_1 (green dotted line). The other parameters were chosen as $\omega_r = 1$, $\beta = 0.005$, $\gamma_1 = 1$, $\gamma_2 = 0.01$ and $\delta = 0.05$. The grey dotted line describes the approximation of the modified resonance frequency $\tilde{\omega}_r$ in accordance with equation 2.134.

the variation of the weak probe field to measure the systems transmission response. This can be achieved by a numerical solution of the implicit functions given above. Figure 2.26 shows the response of the resonator in dependence of the probe field frequency ω_2 for various frequencies of the strong excitation field ω_1, which is represented by the dotted green line. For values of ω_1 close to the resonance frequency ω_r the resonator response is shifted towards higher frequencies. Increasing ω_1 further reveals three separate Lorentzian shaped response functions for the dependence of the probe field. This effect results from the multiple solutions of a Duffing type oscillator under a strong excitation field with the frequency ω_1. The three possible solutions correspond to three different values of z_1, which leads to the emergences of individual response functions. The middle peak thereby arises from the unstable solution as depicted by the dotted line in figure 2.25 and the two side peaks from the stable

solutions. After ω_1 passes the jump frequency, the resonator response restores its original position at approximately ω_r according to the single solution. With a strong excitation field compared to a weak probe field ($\gamma_1 \gg \gamma_2$) it can be assumed, that the corresponding oscillation amplitudes fulfil a similar relation $z_1 \gg z_2$. Therewith, equation 2.131 takes the same form as the response function of a Duffing oscillator with a single strong excitation field

$$\gamma_1^2 = z_1^2 \left((\delta\omega_1)^2 + \left(\frac{3}{4}\beta z_1^2 + \omega_\mathrm{r}^2 - \omega_1^2 \right)^2 \right) \tag{2.133}$$

equivalent to equation 2.129. This relation can be used to calculate $z_1(\omega_1, \gamma_1)$ numerically independent of parameters wit index 2. Hence, the strong excitation field drives the resonator in the non-linear regime with nearly no disturbance of the weak probe field. The resonance response in dependence of ω_2, on the other hand, is altered by z_1 according to equation 2.132. The corresponding modified resonance frequency $\tilde{\omega}_\mathrm{r}$ can then be approximated with equation 2.132 as

$$\tilde{\omega}_\mathrm{r} = \sqrt{\omega_\mathrm{r}^2 + \frac{3}{2}\beta z_1^2(\omega_1, \gamma_1)}. \tag{2.134}$$

The obtained values can be used to describe the position of the response peaks as plotted in figure 2.26. Here the position of the upper resonance according to equation 2.134 is depicted by a grey dotted line. In this limit ($\gamma_1 \gg \gamma_2$) the approximation yields a good description for the resonance frequency.

2.7 Stimulated emission in disordered media

This section provides a brief introduction for the possible collective effect of stimulated emission for an ensemble of broadly distributed two-level states. In order to generate a measurable field contribution in a certain bandwidth of frequency, the intrinsic loss of the entire system has to be not only compensated, but exceeded. This can theoretically be realized for a population inversion ($\Delta\rho < 0$) of the TLS ensemble, which -if maintained- compensates the loss through the contributions from the stimulated emission of the excited TLS. The basic condition for this effect can therefore be written as

$$(\kappa_\mathrm{i} + \kappa_\mathrm{c}) < 0, \tag{2.135}$$

where κ_i is negative for an arising gain. The difficulty hereby lies in the creation and preservation of the population inversion in at least a certain range of frequency. A theoretical description for this was given in [Bur14a] utilizing the Landau-Zener formalism. The calculations provide a model to explain the mechanisms to produce a population inversion, a coherent gain and beyond that a possible regime for lasing to occur. A schematic illustration of this process is depicted in figure 2.27. The population inversion is thereby achieved by Landau-Zener transitions of TLS in the frequency domain of a strong pump field via an external bias sweep. Thereafter the

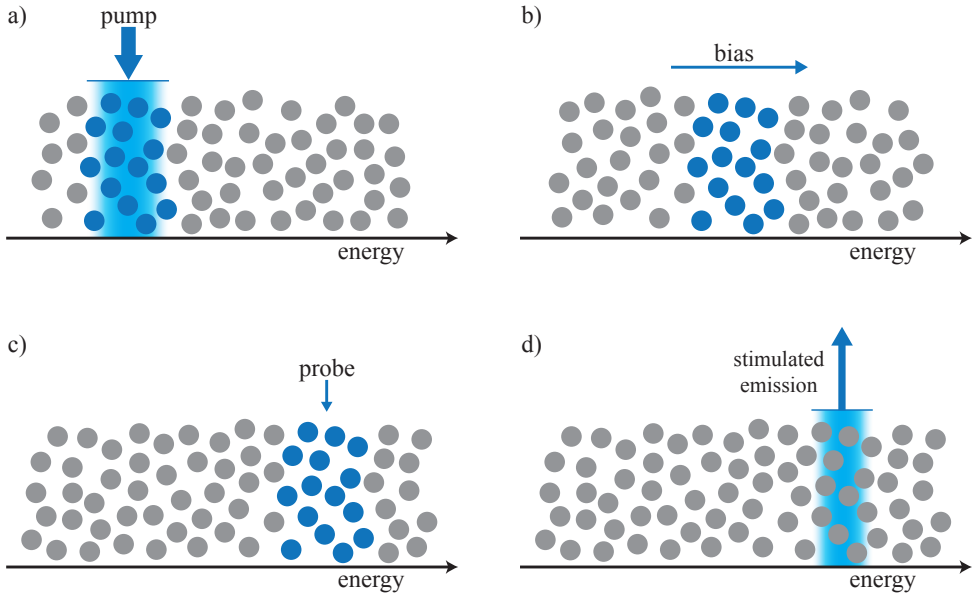

Figure 2.27: Schematic illustration of a process for stimulated emission. **a)** A pump field inverts systems from the ground (grey) to the excited state (blue). **b)** The systems are swept to a different frequency via a bias field. **c)** A weak probe tone is applied in order to induce stimulated emission for the excited systems, which is created in **d)**.

systems traverse the energy domain of a weak probe field under which stimulated emission can produce a coherent gain. If this signal is produced in the frequency window of a resonator setup, it can be picked up and read out via a transmission measurement.
The occurring effect is similar to lasing but the term has to be used with some caution here, since the active medium in this case is an ensemble of energetically random distributed two-level states instead of the normally utilized narrow line width transitions. Additionally, the minimal amount of energy levels for a classical laser system is three in order to realize a population inversion. Fewer levels can only saturate the associated states since stimulated emission is compensated by the absorption process. The mechanism, which is illustrated in figure 2.27, uses a separation in the frequency domain in order to isolate the region of pumping from the stimulated emission to realise the arising gain.
A corresponding system was presented in [Ros16] as a *random-defect laser* and showed the emission of a microwave resonator under off-resonant pumping. The effect of sound amplification by the process of stimulated emission in an amorphous compound was already shown separately in [Pri93]. With the emerging branch of research for the creation of artificial single atoms many related systems show similar properties. Some examples for further reading on this can be found for single-qubit lasing [Hau08], lasing effects on voltage-biased Cooper-pair transistors [Che14] or artificial single atom lasing via voltage-biased superconducting qubits [Ast07, Ash09].

3. Experimental methods

This chapter provides an overview about the experimental methods used within the framework of this thesis. It starts with an introduction of cryogenic measurements in section 3.1 with all elements that enable experiments at very low temperatures. The following section 3.2 deals with the experimental setup. It begins with the investigated sample material in section 3.2.1 and the design and characterisation of the microstructured resonator in section 3.2.2. Afterwards the fabrication of the resonator chip and the sample holder are described in section 3.2.3, followed by an explanation and characterisation of the measurement electronics in section 3.2.4.

3.1 Realising low-temperature measurements

The emphasis of this thesis is the direct resonant interaction of individual two-level systems with the external excitation fields. According to section 2.3.5 this contribution is only noticeable, if the corresponding ensemble is unsaturated or in other words, if the occupation difference is non vanishing. Considering that the frequency domain of the applied fields is around 1 GHz, the temperature of the experiment has to be well below 1 K in order to realise the required conditions. The measurement setup is therefore placed inside a ^{3}He/^{4}He dilution refrigerator of the type Oxford Kelvinox 400[1], which enables measurements in a temperature stabilised environment between 10 mK and 8 K.

The working principle is based on the phase separation of a mixture of ^{3}He and ^{4}He below temperatures of approximately 800 mK. This creates a heavier ^{3}He-poor phase, in which the ^{3}He is diluted in superfluid ^{4}He, and a lighter ^{3}He-rich phase, which consists almost entirely of pure ^{3}He. The actual concentration of ^{3}He in the individual phases depend on the temperature of the mixture. For normal pressure and vanishing temperatures $T \to 0$ the concentrated ^{3}He phase converges towards a pure phase, whereas the diluted phase reaches a ^{3}He-concentration of approximately 6.5 %. Due to the difference in enthalpy of ^{3}He in the individual phases, the separation can be used to realise a cooling effect by the *evaporation* of ^{3}He atoms from the ^{3}He-rich phase into the ^{3}He-poor phase. The ^{3}He, which is diluted in liquid ^{4}He, can hereby be understood as a gas due to the vanishing viscosity of the superfluid. A more detailed description of this effect and the working principle of a ^{3}He/^{4}He dilution refrigerator can be found in [Fro92, Bal96, Ens05, Pob07]. The following section is a short overview of the experimental framework but for deeper under-

[1] Oxford Instruments, Tubney Woods, Abingdon, Oxon, OX13 5QX, England

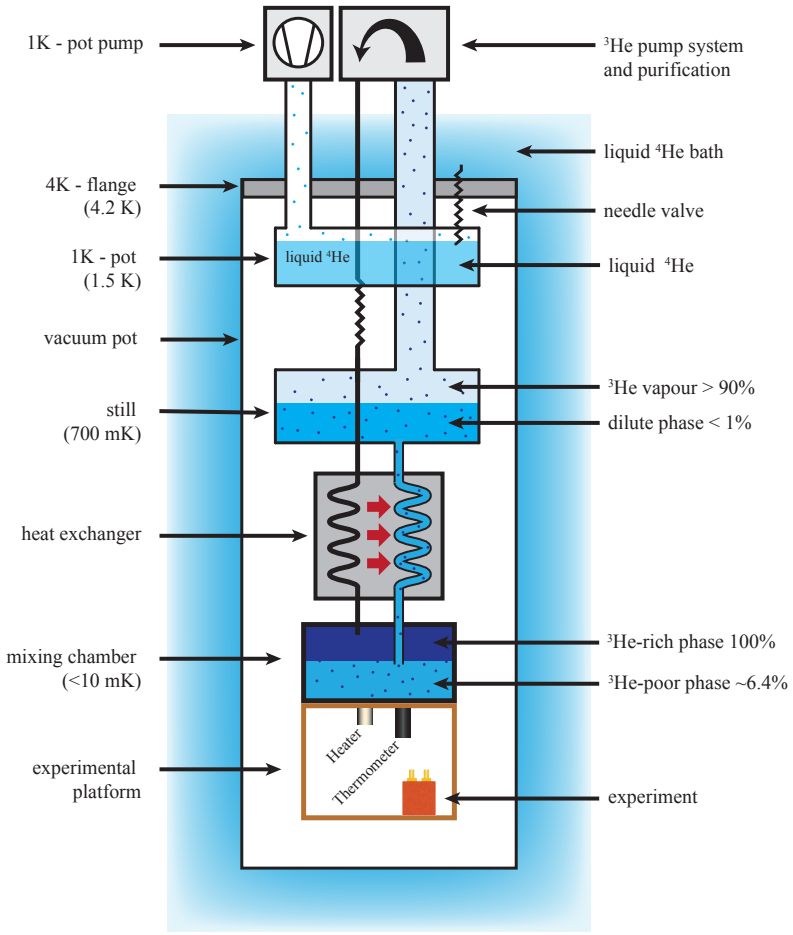

Figure 3.1: Schematic illustration of the ^{3}He/^{4}He dilution refrigerator. The entire dilution unit is enclosed in a vacuum pot surrounded by a liquid ^{4}He bath. The individual cooling stages further reduce the temperature in order to reach values below 10 mK at the mixing chamber and the experimental platform. The schematic illustration is adapted from [Pob07, Fre21].

standing the literature is recommended. A schematic illustration of the main part for the ^{3}He/^{4}He dilution refrigerator unit is shown in figure 3.1. In order to realize these low temperatures all sources of thermal heat transport have to be reduced to a bare minimum. The entire setup is therefore enclosed in a vacuum pot and the different cooling stages are shielded against thermal radiation. The mechanical connection in between stages is thermally decoupled from the next stage through materials with low thermal conductivity. The vacuum pot is placed in a liquid ^{4}He bath to precool the individual components and to improve the achieved vacuum by the condensation of the remaining gas on the inner surface. The first cooling stage is the 1K-pot, which is independent from the circulation of the ^{3}He/^{4}He-mixture. It

consists of a reservoir for liquid ^{4}He, which can be feed from the main bath via a needle valve. Constantly pumping the contained ^{4}He reduces the temperature down to approximately 1.5 K. This stage can hence be used for the condensation of the ^{3}He/^{4}He-mixture. The resulting phase separation is formed in the mixing chamber by design. During its passage the temperature of the mixture is further reduced by thermal coupling to the individual stages and the heat exchangers (continuous and step heat exchanger). For the generation of a constant cooling power, it is essential to reduce the concentration of ^{3}He in the diluted phase inside the mixing chamber. This is achieved by the still, which creates an osmotic pressure through the evaporation of ^{3}He. The ^{4}He thereby stays liquid since the vapour pressure of ^{3}He is much higher than for ^{4}He. The temperature of the still is hence adjusted to increase the circulation flow of ^{3}He whilst minimizing the ratio between ^{3}He and ^{4}He vapour. After that, the gas goes through the pumps (rotary and roots pump) and is purified by a nitrogen cold trap followed by a helium cold trap. The ^{3}He is then fed back into the condensation capillary to repeat the circulation process. Since the mixing chamber is the coldest part of the cryostat, the experimental platform is mounted directly underneath.
The temperature of the cryostat is controlled by an additional heater on the experimental plattform. Since the circulation provides a constant cooling power, higher temperatures are achieved by heating the experimental platform to the desired value. The stabilisation of temperature is thereby realized by a PID controller within a LabVIEW routine to monitor the different parameters for the refrigerator unit. The temperature on the mixing chamber, hence also of the experimental platform, is read out by a carbon resistor thermometer. This thermometer is calibrated by a noise thermometer, which on the other hand was calibrated by a fixed point thermometer [Rei17]. During the experiments, the corresponding resistivity is measured by an AC resistance bridge[2], which utilises small excitation fields to avoid parasitic heating effects.

[2]LR-700, Linear Research Inc., 5231 Cushman Place, Suite 21, San Diego, CA 92110-3910, USA

3.2 Experimental setup

This section is dedicated to explain the experimental setup used within the framework of this thesis from the investigated sample in section 3.2.1 over the resonator design and characterisation in section 3.2.2 to the fabrication of the chip and the sample holder in section 3.2.3. Thereafter the measurement electronics for the readout of the resonator chip are introduced in section 3.2.4 including the rf-pathway and all utilised measurement devices.

3.2.1 Sample

The sample material in this thesis is a thin layer of sputter deposited silicon dioxide (SiO_2). Since it is one of the most prominent representatives for network formers in glasses, it acts as a building block for many multi component glasses. With the vapour deposition technique, by which silicon is sputter deposited in a pure oxygen atmosphere, it became possible to microstructure thin layers of this material in all desired shapes. Silicon dioxide is therefore used as a standard isolation layer in the field of microelectronics. The general structure was already presented in section 2.1 for the introduction of the amorphous and crystalline networks. If no further precautions are undertaken, the disordered state is more likely to emerge, since the formation of the crystalline lattice requires stable temperatures and a precise oxygen concentration condition. For the utilised sample, however, the oxygen concentrations are optimised for as little magnetic contamination as possible. In reality, the term SiO_x would therefore be more accurate to describe the sample composition, but the following sections will also refer to it as SiO_2. A good comparison with similar sample materials measured with different resonator geometries can also be found in [McR20], which summarized many measurements on thin film dielectrics.

3.2.2 Microstructured resonator

In the low frequency regime, the dielectric properties can directly be determined with a capacitance bridge measuring a capacitor containing the sample material. In the Megahertz-regime and for higher frequencies the capacitive reactance makes this measurement technique difficult, which is why another approach is required to extract the desired quantities. The most common concept is the deployment of a resonator circuit, which is able to enhance the amplitude at its resonance frequency and therefore simultaneously acts as a band pass filter for off-resonant frequencies. For electrical excitation fields the most straightforward realisation is an LC-resonator with an inductance L and a capacitance C analogous to the description presented in section 2.6.1. Within the framework of this thesis, an LC-resonator in hanger

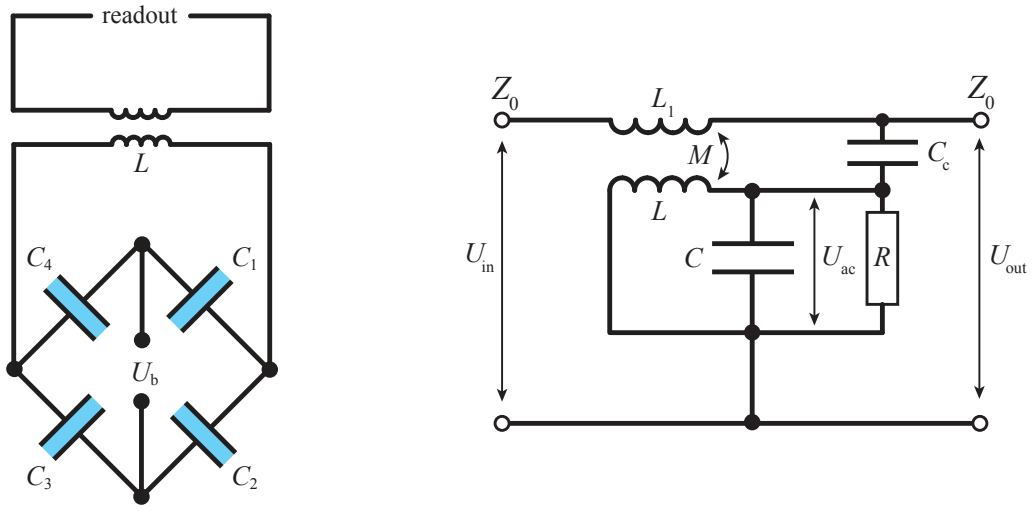

Figure 3.2: Left: Schematic illustration of the Wheatstone bridge-like arrangement for four identical capacitors loaded with a dielectric material (blue). **Right**: Corresponding circuit diagram for an equivalent RLC-resonator [Kha12], which can be used to model the LC-resonator in hanger mode.

mode is used to measure the dielectric properties of the material. In this type of operation, the resonator is coupled inductively to a transmission line and only absorbs the applied field, if the resonance condition is fulfilled. This has the advantage that off-resonant frequencies can be used to extract a background for the remaining electronic setup.

In order to perform pump-probe experiments on the material, strong fields are required inside the capacitor. With the purpose of avoiding a coupling into the transmission line of the resonator, which is used as the readout branch during the experiment, a Wheatstone bridge-like arrangement of capacitors as in figure 3.2 (left) is used. It consists of four identical capacitors (C_1, C_2, C_3 and C_4) each with capacitance C, which are arranged in a loop in order to create two decoupled branches. The sample is thereby used as the dielectric material in each capacitor. The total capacitance for this arrangement can be easily calculated to be C as well. Together with the inductance, which is connected to the horizontal branch, this forms the LC-circuit. In addition, the coil is inductively coupled to the transmission line for readout. The applied driving field therefore generates an effective voltage across the horizontal diagonal. Since all four capacitors are identical, the additional vertical branch for biasing is decoupled from the readout branch. This is also beneficial for the integrated amplifiers in the output side of the transmission line to avoid a saturation and a non-linear drive.

Figure 3.2 (right) shows the corresponding circuit diagram of an equivalent RLC-circuit. The incoming rf-field with amplitude U_{in} is inductively M and partially

capacitively C_c coupled from the impedance matched $Z_0 = 50\,\Omega$ transmission line into the resonator. This creates a voltage U_{ac} across all elements inside the resonator. The outgoing signal U_{out} therefore depends on the amount of field absorbed by the RLC-circuit, which is equivalent to the description introduced in section 2.6.1. According to that, the LC-resonator can be described by the resonance frequency

$$f_{res} = \frac{1}{2\pi\sqrt{LC}} \tag{3.1}$$

and the loss contributions, which can be defined as dimensionless quality factors according to

$$Q = \frac{\pi f_{res}}{\kappa}, \quad Q_i = \frac{\pi f_{res}}{\kappa_i} \quad \text{and} \quad Q_c = \frac{\pi f_{res}}{\kappa_c}. \tag{3.2}$$

This yields the relation

$$\frac{1}{Q} = \frac{1}{Q_i} + \frac{1}{Q_c}, \tag{3.3}$$

for which the individual contributions can be identified as internal Q_i and from the coupling of the electric field to the transmission line Q_c. The internal quality factor can have many contributions, but in this case it mainly originates from two-level systems and hence $Q_i \approx Q_{i,TLS}$ holds. In certain circumstances Q_i can have additional sources of loss, especially when the ensemble of TLS is saturated and other mechanisms of loss dominate for example different contributions from quasiparticle loss, vortex loss, radiative loss and parasitic modes [McR20]. The two parameters f_{res} and Q can consequently be used to characterise the resonator, and since they are directly connected to the dielectric properties, also to characterise the sample material.

According to equation 3.1, the resonance frequency is directly dependent on the capacitance C of the LC-circuit, which is a function of the dielectric real part ε'. It is important to take into account that the capacitance C consists of two parts, the capacitance C_d originating from the dielectric response of the sample and the parasitic capacitance C_p, which is caused by the electric field in vacuum outside the capacitor. The total capacitance can therefore be expressed by

$$C = C_d + C_p. \tag{3.4}$$

With equation 3.1 and under the assumption that the stray capacitance is constant, the relative change of the dielectric real part can be written as

$$\frac{\delta\varepsilon'}{\varepsilon'} = \frac{\delta C_d}{C_d} = \frac{\delta C}{C}\frac{C}{C_d} = \left(\left(\frac{f_{res}^*}{f_{res}}\right)^2 - 1\right)\frac{1}{\mathcal{F}}. \tag{3.5}$$

The quantity f_{res}^* is hereby an arbitrary reference point of the measured resonance frequencies, which is often chosen as the minimum in the temperature dependency.

The derivation of equation 3.5 also assumes no significant change in inductance L and no other effects like for example a change of sample size through thermal expansion. The corresponding modification for the dielectric loss hence is

$$\tan\delta = \frac{1}{Q_{\mathrm{i,d}}} = \frac{1}{Q_{\mathrm{i}}\sqrt{\mathcal{F}}}. \tag{3.6}$$

The parameter $\mathcal{F}$ is called the filling factor and is calculated by the relation

$$\mathcal{F} = 1 - \frac{C_{\mathrm{p}}}{C}. \tag{3.7}$$

It can be understood as a measure for the amount of electric field lines that penetrate the sample compared to the field lines in vacuum. Its value is mainly dependent on the geometry of the sample and the capacitance, which will be discussed in the following section for the resonator design in this thesis.

Design

The circuit from figure 3.2 is realised as a lumped element resonator. This type of resonators are characterised by their small dimensions compared to the wave length of the resonance frequency. The individual elements can therefore be treated as separate components with a capacitance C and an inductance L instead of a standing wave formalism. For that, the electrical circuit is microstructured on a 3"-silicon waver. The silicon hereby serves only as the substrate for the design. A single resonator chip is thereby fairly small (10 mm×10 mm), which is why the entire waver can fit 32 chips in total for the production process. One of these chips is illustrated in figure 3.3 with the schematic design for the resonator. The metal conductor layers are made from niobium, which becomes superconducting below approximately 9.2 K [Mat63]. This property inhibits ohmic losses of the material, which enables the production of resonators with very high quality factors. As already mentioned above, the capacitance consists of four capacitors with identical surface area of 120 µm×105 µm. The individual capacitors are in this case realised as parallel plate capacitors with a niobium layer for the individual plates and a 300 nm thick SiO_2 isolation layer as the dielectric material. This yields a capacitance of about 1.45 pF for each capacitor. In comparison to a standard interdigital capacitor (IDC) the electric field is expected to be much more homogeneous. The comparatively small distance of the capacitor plates, which is given by the thickness of the sample material, additionally enables high field strengths. This is also higher than what is achievable for the IDC since the minimal spacing for the capacitor finger is approximately 1 µm.
To apply the bias voltage against ground, an additional bond pad is connected to two capacitors (C_1 and C_4) as depicted in the circuit diagram of figure 3.2. The remaining two (C_2 and C_3) are attached to the ground plane. The enlarged version

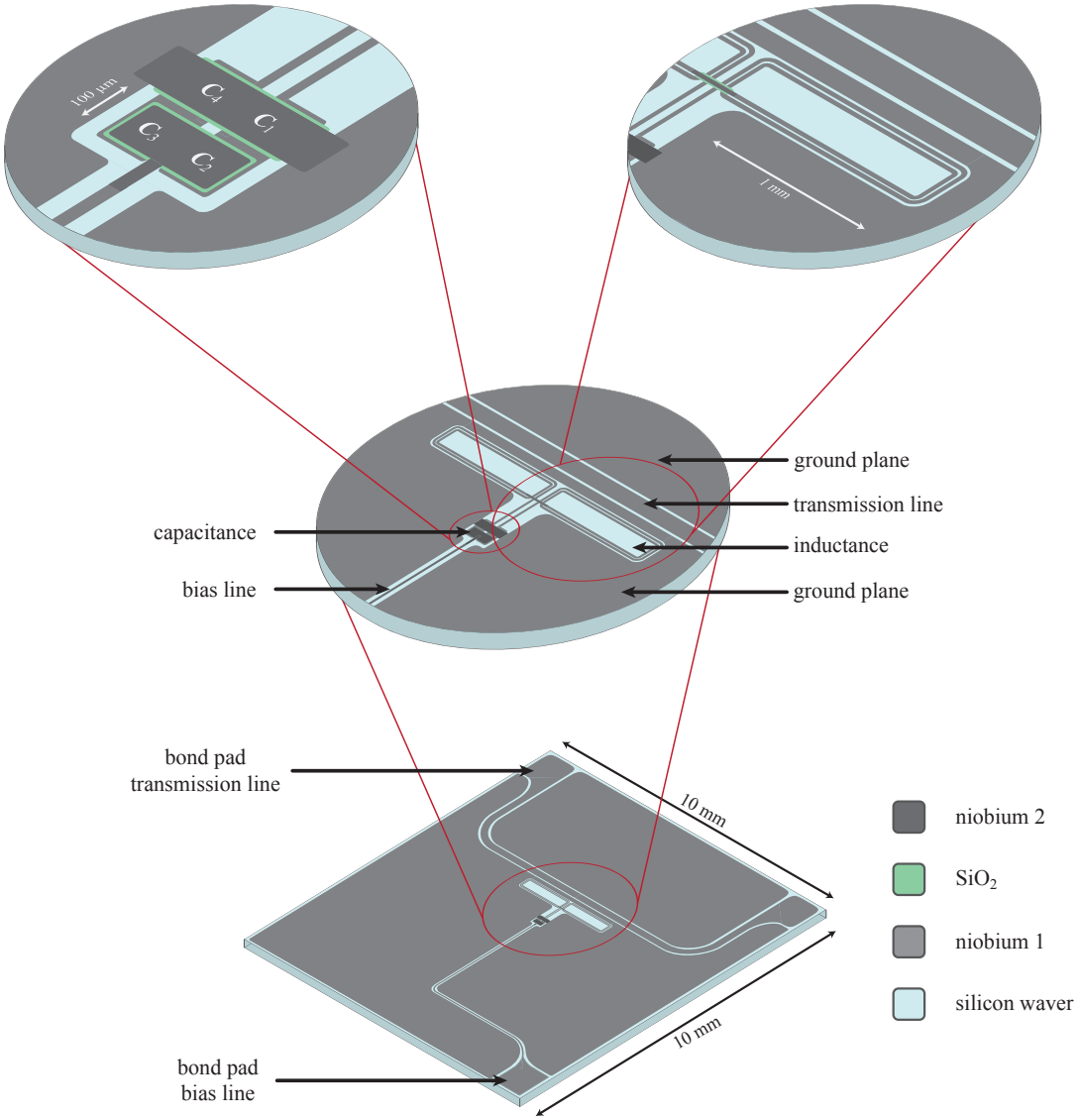

Figure 3.3: Schematic illustration of the resonator chip design. The picture shows the individual microstructured layers on the silicon waver substrate with enlarged segments of important structures. The first zoom-in shows the entire resonator, which is coupled to the transmission line. The other two zoom-ins show the capacitance bridge of the design and the geometry of the inductance in more detail.

in figure 3.3 shows the alignment of the individual layers and the connections for the desired capacitance bridge. The inductance is formed by two separate coils, which are connected by a conductor bridge. The classical meander structure was not chosen since the illustrated design reduced the asymmetry of the resonance curve in the simulations drastically. The coil is separated from the feedline by a small stripline of niobium, which is part of the ground plane. This isolates the resonator from the

transmission line and hence increases the coupling quality factor. The thickness of this ground plane stripline was adjusted to 130 µm to achieve the desired high value for Q_c. For the connection of the resonator feedline to the readout chain of the measurement electronics, two bond pads are placed at the upper edges of the chip. The width of the feedline and the gap distance to the surrounding ground plane is thereby chosen to match an impedance of 50 Ω.

Characterisation and simulation

With the resonator design at hand this section gives an introduction on how to evaluate a transmission measurement of the device and how to extract the desired parameters from S_{21} data. The presented chip was designed and simulated with the software Sonnet[Son18]. The resonator parameters can thereby be chosen as desired and the resonance frequency can easily be adjusted according to the inductance and capacitance. For this purpose the simulation parameters were selected as $\varepsilon_r = 3.9$ for the dielectric response, $\tan\delta = 4 \cdot 10^{-4}$ for the loss tangent and $d = 300\,\text{nm}$ for the thickness of the dielectric material. The metal structure was assumed as lossless since the niobium will become superconducting at low temperatures. The additional bias connection was grounded for the simulations. With this, the calculation yields the S_{21} parameter similar to a resonator response measurement with different excitation frequencies. The resulting simulation is depicted in figure 3.4 and shows an ideal symmetric resonance behaviour with $f_{\text{res}} = 1094.79\,\text{MHz}$. The coupling quality factor according to the simulation $Q_{\text{c,sim}}$ can be calculated as

$$Q_{\text{c,sim}} = \frac{\min(S_{21})}{1 - \min(S_{21})} Q_{\text{i,sim}} \tag{3.8}$$

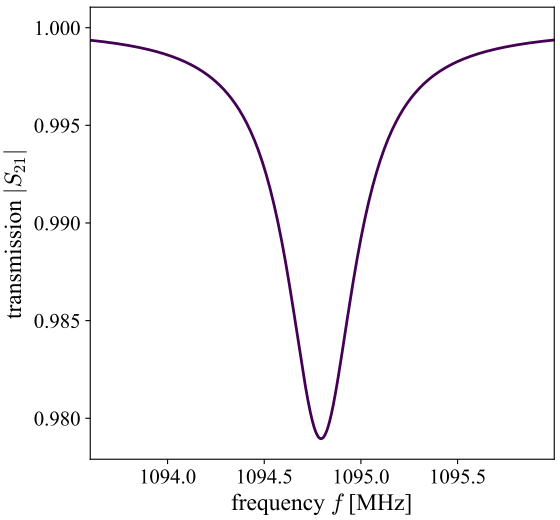

Figure 3.4: Simulation of the resonance frequency with the design from Sonnet software. The curve shows the characteristic Lorentzian shape with a minimal amplitude $\min(S_{21}) = 0.979$ and a resonance frequency of $f_{\text{res,sim}}$ =1094.79 MHz.

with the intrinsic quality for the simulation $Q_{\mathrm{i,sim}} = 1/\tan\delta$. This yields an expected coupling quality factor of $Q_{\mathrm{c,sim}} = 117000$ for the simulated design. As already derived in equation 2.126, this type of resonator is describable via a Lorentzian function. An analogous result was found by [Kha14] for the description of an LC-resonator in hanger mode coupled to a transmission line, which is given by

$$S_{21}(f) = 1 - \frac{Q/Q_{\mathrm{c}}}{1 + 2iQ\frac{f-f_{\mathrm{res}}}{f_{\mathrm{res}}}}. \tag{3.9}$$

In a realistic measurement environment a resonator usually shows deviation from this behaviour. One of the main contributions are asymmetries of the resonance response due to impedance mismatches. They are difficult to avoid since they originate from many sources, for example the connectors between cables, the bonds or material changes. Equation 3.9 can hence be extended for the non-ideal resonator case with additional terms following [Pro15] as

$$S_{21}(f) = ae^{i\alpha}e^{-2\pi i f\tau}\left(1 - \frac{Q/Q_{\mathrm{c}}e^{i\phi}}{1 + 2iQ\frac{f-f_{\mathrm{res}}}{f_{\mathrm{res}}}}\right). \tag{3.10}$$

The amplification or attenuation in the measurement path lead to a scaling factor a of the measured signal. Additionally, a possible phase shift of the outgoing signal is represented by the factor $e^{i\alpha}$. Also the cables can cause an additional delay τ, which is dependent on frequency and therefore results in the phase factor $e^{-2\pi i f\tau}$. The effect of imbalanced impedances is included by the factor $e^{i\phi}$, which effectively assumes a complex value for the coupling quality factor Q_{c} [Kha12]. The corresponding algorithm described in [Pro15] can then be used to remove the non-ideal behaviour by applying individual transformations to compensate the additional factors.
Figure 3.5 shows exemplary data from the resonator chip for 165 mK. The illustrated

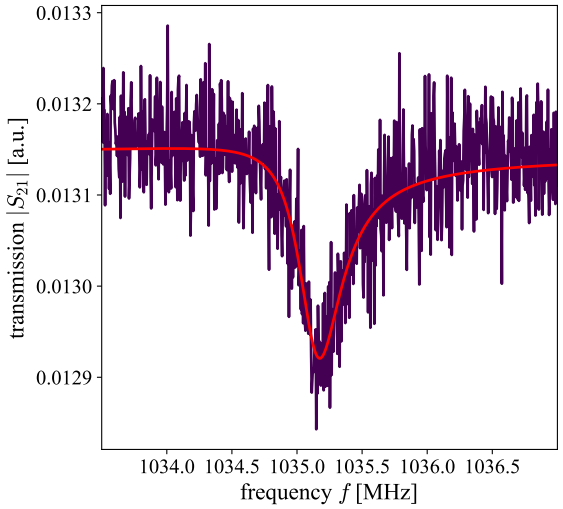

Figure 3.5: Exemplary data (dark blue line) for a transmission resonance measurement at 165 mK. The corresponding fit function (red line) from equation 3.10 describes the obtained S_{21}-parameters well. It yields a resonance frequency of $f_{\mathrm{res,exp}} = 1035.14$ MHz and a coupling quality factor of $Q_{\mathrm{c,exp}} = 149000$.

$f_{\mathrm{res,sim}}$	$f_{\mathrm{res,exp}}$	$Q_{\mathrm{c,sim}}$	$Q_{\mathrm{c,exp}}$
1094.79 MHz	1035.14 MHz	117000	149000

Table 3.1: Comparison between the simulated values and the experimentally obtained parameters for the resonance frequency and the coupling quality factor.

fit was conducted according to equation 3.10 and is in good agreement with the S_{21} data. Since the coupling quality factor was selected very large, the data at low temperatures and low field strengths generally shows an unsatisfactory signal to noise ratio. Measurements in this temperature regime hence depend on many averages and a high bandwidth resolution to extract the parameters. The benefit of high Q_{c} values is the isolation of the resonator from the remaining measurement system. The fit of the S_{21} data can be used to extract the resonance frequency and the coupling quality factor and compare it to the simulated parameters, which were adjusted by design. The corresponding values are depicted in table 3.1.
The experimentally obtained resonance frequency is slightly lower than the targeted value. This could be the result of a small deviation for example in the thickness of the isolation layer during the fabrication process. The specific source of this deviation is not of importance as long as the resonance frequency is of the right order of magnitude. Note that the resonance frequency also changes with temperature in a range of 1033 MHz to 1040 MHz due to the change in dielectric permittivity.
The coupling quality factor Q_c is slightly higher than the expected value from the simulation but also matches the right order of magnitude. This value is expected to be unchanged under variation of temperature or other system parameters. Since its value is approximately two orders of magnitude higher than the intrinsic quality factor of the sample, it is expected to have only a small contribution to the total quality factor Q according to equation 3.3.
It is also important to keep in mind that equation 3.10 assumes a constant quality factor Q_{i} during the measurement sweep. Especially for strong driving fields this condition is not satisfied due to the saturation of the underlying TLS-ensemble as described in section 2.2.2. The loss of the material and therefore the quality factor of the resonator is dependent on the applied electric field strength. Inside the resonator, this field strength is strongly dependent on the applied frequency according to the Lorentzian line shape. At resonance the amplitude is maximal and therefore much stronger than for detuned frequencies. This results in a frequency dependent internal quality factor of the material during a measurement sweep. The peak would hereby get sharper, due to the enhanced quality factor, whereas the sides of the detuned frequencies would be almost unchanged. This alters the shape of resonance curve and therefore under- or overestimates the extracted parameter for the quality factor.

This effect becomes important especially for high driving fields above the critical field value. Furthermore, the utilised parallel plate capacitor geometry was investigated for the field distribution and to determine the filling factor for the setup. For this purpose a finite element simulation of the capacitor field was performed with the software FEMM[3]. Figure 3.6 shows the simulation result for a vertical slice of the resonator geometry. The individual layers are hereby modelled on top of the silicon waver with vacuum above. The field distribution is mostly homogeneous especially

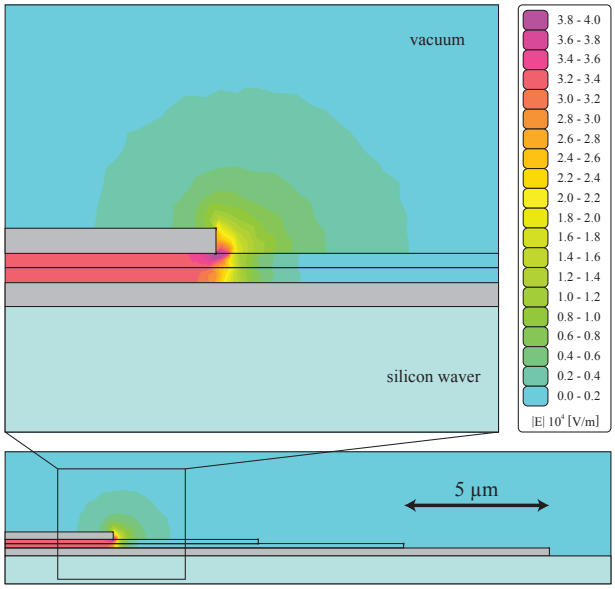

Figure 3.6: Simulation of the electric field strength for an vertical slice of the resonators plate capacitor geometry. The two SiO_2-layers are between the niobium structure (grey) on top of the silicon waver. The enlarged picture shows the border region, in which the field lines deviate from the homogeneous behaviour in the remaining structure. The simulation only shows minor field leakage and yields a filling factor of $\mathcal{F} = 0.996$.

between the capacitor plates. The edges show some leakage of the electric stray field, but only with minor effects in a restricted area. The simulation can also be used to calculate the filling factor for the design. It can be calculated by the stored energy inside the dielectric material compared to the entire stored energy. This yields a filling factor of $\mathcal{F} = 0.996$, which is close to the expected value for an ideal parallel plate capacitor of 1. It can therefore be assumed that the amount of parasitic capacitance is insignificant compared to the capacitance originating from the dielectric.

3.2.3 Fabrication and sample holder

The fabrication of the microstructured resonator was done in-house in a cleanroom by members of our working group. The structure was realised by a four-layer-process consisting of the first niobium layer with 250 nm thickness, two isolation layers with 150 nm SiO_2 each and the second niobium layer with 500 nm. For the first layer, the silicon waver is fully covered with niobium. The excess material is then etched by

[3]Finite Element Method Magnetics

a plasma beam to produce the desired micro-structure. Afterwards, the two isolation layers are added with a standardized lift-off process. A photoresistive varnish is therefore applied to the entire waver. The negative of the structure is then created by the removal of the photoresist at specific sites through photolithography. The material is then sputter deposited onto the entire waver, but only the exposed sections add to the underlying structure. The photoresist together with the supplementary material on top is then removed, so that only the desired structure remains. The second isolation layer is produced analogously. The SiO_2-layer is fabricated in two separate layers to create steps for the bridge connection of the inductance and the capacitor plate connections. This process is necessary to ensure the conductivity of the final niobium layer, but has no significant experimental effect. Too large differences in hight might lead to a discontinuity in the conductor path. The second niobium layer is also applied by a lift-off process. After the production, the waver is coated with a protective varnish and sawed into individual chips. Before the assembly of the experiment the protective varnish is removed with different solvents and an ultrasonic bath. Figure 3.7 shows a microscope picture of the critical structures from the cleanroom directly after fabrication. The cleaned chip is then mounted

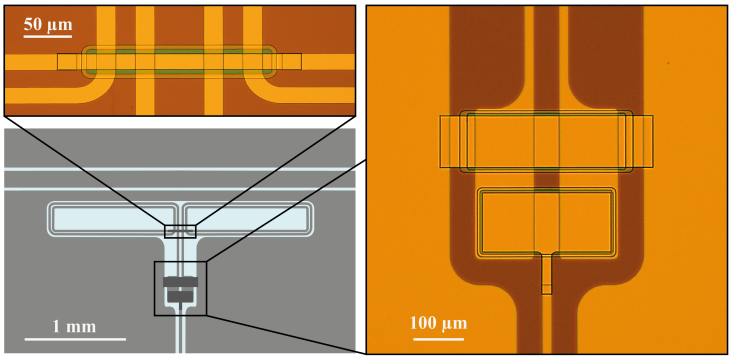

Figure 3.7: Microscope pictures after the production of the design in the cleanroom. The bottom left picture shows the schematic illustration with two zoom-ins for the conductor bridge of the inductance and the capacitance region.

inside the sample holder, which is shown in figure 3.8 with the matching cover. The holder is made from tempered oxygen-free copper and coated on the inside with a layer of niobium. This additional step is applied to create a superconducting layer at low temperatures to reduce the radiation losses of the resonator setup. The chip is then glued with GE varnish, which functions as an adhesive and simultaneously ensures the thermal contact to the copper body. The connection from the bondpads to the inner conductor of the SMA connectors is achieved directly by bonding with aluminium wire. In order to create a smooth surface, the SMA connector is filled with a piece of wire made from a copper-nickel-zinc alloy and soldered to the SMA connector. Afterwards, the smooth surface is achieved by milling the created extension of the connector to a plane surface. The ground connection is achieved by bonding from the chip directly onto the surface of the sample holder, which is connected to the experimental platform and therefore the cryostat's ground.

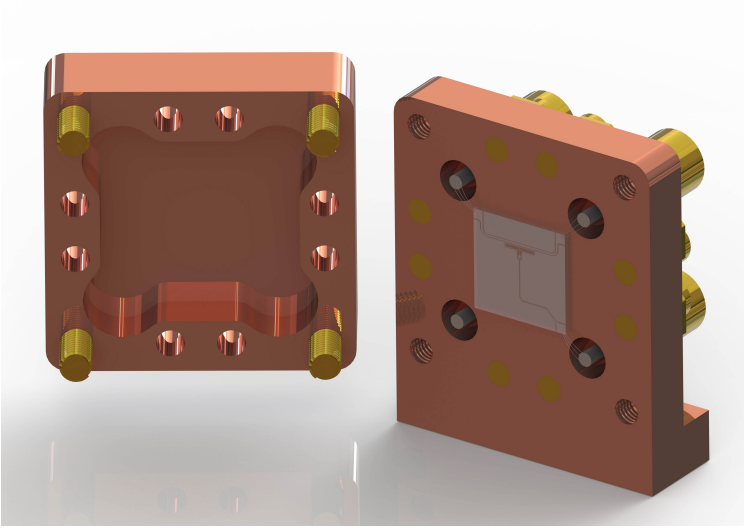

Figure 3.8: Rendered picture of the sample holder on the right with the matching cover on the left. The resonator chip is glued to the sample holder and connected via bonds to the inner conductor of the SMA connectors.

3.2.4 Measurement electronics

In order to read out the resonance frequency of the device a well tuned rf-measurement setup is needed, which is schematically illustrated in figure 3.9 with all the essential parts. The core component of the measurement is the vector network analyser[4] (NWA) with a frequency range from 300 kHz to 1.3 GHz. The NWA provides a source signal at its output port, which it passes to the device under test. The input port then compares the received signal with the initial value and captures the electrical network parameters including the transmission, the reflection or the S-parameters. Several measurements within this thesis required the evaluation of the spectrum coming from the resonator. These measurements used a different NWA[5], which can additionally be operated as a spectrum analyser (SA). The source signal of the output port is thereby disabled and the input port functions as the SA. In this type of operation the device can receive an rf-signal only from other sources. The frequency range of the HP 4396A is 100 kHz to 1.8 GHz in the NWA mode and 2 Hz to 1.8 GHz in SA mode. Both devices have an adjustable output power ranging from −20 dBm to 5 dBm for the source signal.
The coaxial cables are equipped with several attenuators outside the cryostat and on the different stages down to the experimental platform. Two of them are at room temperature (RT) outside the cryostat. The first attenuator[6] is controllable via a micro-controller[7] and the associated LabVIEW software from the computer. It contains six attenuator elements (1 dB, 2 dB, 4 dB, 8 dB, 16 dB, 32 dB), which can be switched on individually. The device therefore allows a signal reduction from 0 dB

[4]HP 8752C, Hewlett-Packard Company, 3000 Hanover Street, Palo Alto, CA 94304-1185 USA
[5]HP 4396A, Hewlett-Packard Company, 3000 Hanover Street, Palo Alto, CA 94304-1185 USA
[6]Model 50P-1207 Serial 287346, JFW Industries INC, 84 Iron St, Johnstown, PA 15906, USA
[7]Arduino Pro Mini 328 - 5V/16MHz

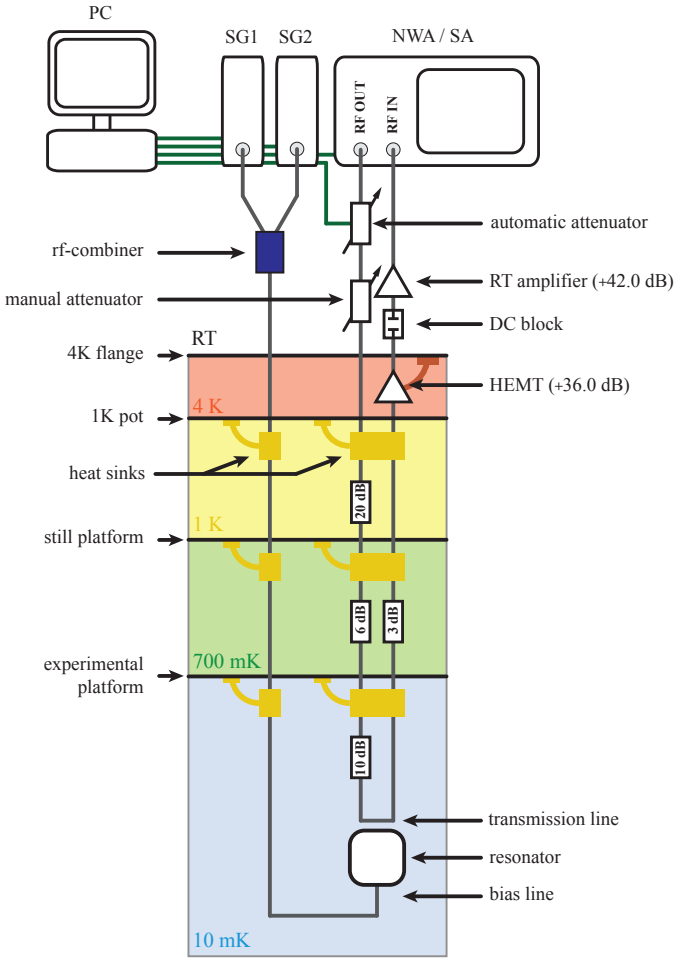

Figure 3.9: Schematic illustration of the individual components of the measurement electronics. The NWA is connected via the transmission line with the resonator chip. The additional bias line enables the application of up to two distinct frequencies to the sample without interfering with the readout chain. Some devices are controllable via a GPIB connection (green lines) by the computer, which runs the LabVIEW measurement routine.

to 63 dB in increments of 1 dB. The second one is a step attenuator[8] with values adjustable from 0 dB to 60 dB in steps of 10 dB. For the experiment, the second attenuator is primarily used to roughly adjust the order of magnitude for the measurement signal. The automatic attenuator can then be used to select the specific input power within the routine of the measurement program.
Inside the cryostat on the input side of the transmission line are three additional attenuators at different temperature stages. There are 20 dB at 1 K, 6 dB at 700 mK and 10 dB at 10 mK. These attenuators reduce the effective noise temperature and therefore increase the signal to noise ratio step by step starting at room temperature.

[8]Step Attenuator AE116-60-01-0N, Weinschel, 5305 Spectrum Drive Frederick , MD 21703 USA

The corresponding noise temperature can be calculated by the Friis formula [Fri44] and is approximately 180 mK at the resonator. Having said this, the experiment is however limited by the noise temperature of the utilised amplifier, which comes to 8 K [Low13]. The different attenuators also prevent the formation of standing waves along the coaxial cables resulting from possible impedance mismatches. For further reading on the optimisation of the rf-setup [Kri19] is recommended.
Heat sinks (golden boxes in figure 3.9) at the individual stages of the cryostat ensure a good thermal contact for the inner conductor of the coaxial cables. This prevents heat leaks from a direct thermal coupling through the cables from room temperature to the experiment. Inside the cryostat the signal is transmitted mainly by semi-rigid coaxial cables. Only the last few centimetres from the last heat sink to the SMA connector of the experiment are flexible stainless steel miniature coaxial cables. They have more attenuation per meter, but are especially useful due to their flexibility for the connection of the measurement setup.

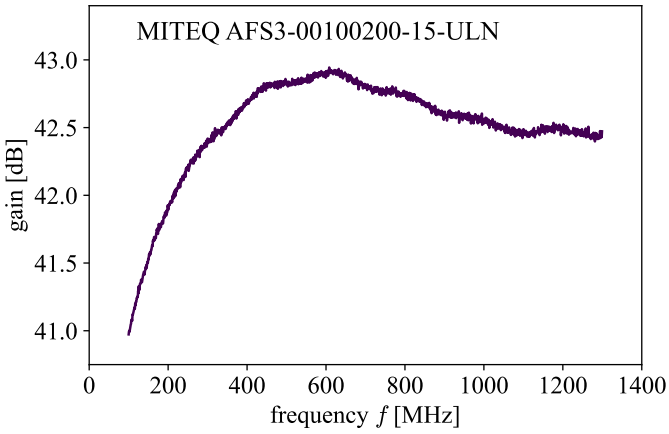

Figure 3.10: Measurement of the gain from the MITEQ room temperature amplifier from [Fre16].

The returning signal has usually a small amplitude, which is why the outgoing measurement line is equipped with two amplifiers. The first amplifier is a high-electron-mobility transistor[9] (HEMT) amplifier, which is thermally coupled to the 4K-flange of the vacuum pot. These devices are commercially available and operate as a low power amplifier suitable for low temperatures and high frequencies up to several GHz. At a frequency of 1 GHz the HEMT provides an amplification of approximately 36 dB [Low13]. The second amplifier is a low noise room temperature amplifier[10] with an amplification of approximately 42 dB as illustrated in figure 3.10. The additional DC block[11] at room temperature between the two amplifiers acts as a filter for DC-currents and low frequencies. This applies for both directions, for signals from the cryostat and for signals from the room temperature amplifier.

[9] LNF-LNC1 12A s/n 313B, Low Noise Factory AB, Nellickevägen 24, 412 63 Göteborg, Sweden
[10] AFS3-00100200-15-ULN, Narda-MITEQ, 435 Moreland Rd Hauppauge, NY 11788 USA
[11] Crystek CBLK-300-3, Crystek Corporation, 16850 Oriole Road Fort Myers, Florida 33912, USA

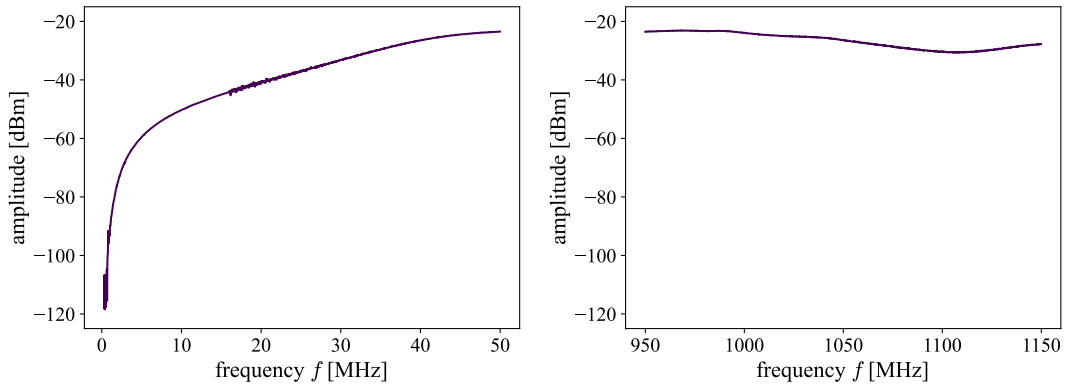

Figure 3.11: Transmission measurement of the S_{21}-parameter in the low frequency regime from 0.3 MHz to 50 MHz (**left**) and in the high frequency regime from 950 MHz to 1150 MHz.

Furthermore, a simple transmission measurement of the S_{21}-parameter was conducted to determine the attenuation of the coaxial cables. This measurement is shown in figure 3.11 for low frequencies between 0.3 MHz and 50 MHz (left) and high frequencies between 950 MHz and 1150 MHz. It was conducted with 0 dBm output power of the NWA and 50 dB on the manual attenuators. The low frequency decrease is thereby caused by the amplifiers and the DC block. At high frequencies in the range of the resonance frequency the additional attenuation originating from the coaxial cables can be approximated by this measurement as 14 dB. With the assumption of a symmetric assembly each coaxial line can be assumed to have 7 dB of attenuation. Within this thesis, all values of excitation power therefore include the added values of all attenuators plus one cable branch, if not stated otherwise. This value hence corresponds to the power in the transmission line on the chip.
The bias branch consists of two signal generators[12,13], which are brought together with an rf-combiner. The corresponding coaxial cable is directly connected to the resonator without additional attenuation. Analogous to the readout chain, the bias line is thermally coupled to the individual stages of the cryostat through a separate set of heat sinks. For the application of a constant voltage to the bias line to observe single TLS dynamics it would be necessary to low-pass filter this branch, otherwise the voltage noise disturbs the coupling of TLS to the resonator [Hun22].
All programmable measurement devices are connected to the computer via a GPIB connection (green lines in figure 3.9). With this it is possible to use different measurement routines in LabVIEW to control all important devices and change the

[12]RS SMH, Rohde & Schwarz, Mühldorfstrae 15, 81671, Munich
[13]HP 8648C, Hewlett-Packard Company, 3000 Hanover Street, Palo Alto, CA 94304-1185 USA

system parameters during a measurement. Together with the temperature control of the cryostat this enables a fully automated data acquisition for a given set of parameters.

4. Experimental results

This chapter presents the experimental results of this thesis. The first section begins with a standard measurement to ensure a sufficient thermalisation of the sample. The following section 4.2 focuses on the saturation experiments for the TLS ensemble. Section 4.3 thereafter shows the temperature dependency of the samples dielectric function to compare it to the derived theory. The following section 4.4 continues with pump probe experiments under symmetric and asymmetric pump-tones. The experiment revealed the appearance of an additional non-trivial peak in the frequency spectrum, which is characterised in subsection 4.4.3. It also provides an explanation for the observed characteristic of the resonator's frequency response spectrum. This observation leads to a more detailed investigation of the non-linear properties of the resonator setup in section 4.5. Afterwards, the phenomenon is further examined in section 4.6, in which a theoretical approach is provided in section 4.6.2 to explain the observed limits and behaviours.

4.1 Thermalisation

Amorphous structures and glassy compounds are well known for long thermalisation time scales, sometimes in the order of hours or even days. Especially in the lowest temperature range this is mainly caused by tunneling systems, which possesses very small relaxation rates due to the statistically broad distribution of parameters and thus release the stored heat only slowly to their surroundings. Together with the generally high heat capacity and low thermal conductivity this can lead to an internally induced heat leak originating from these materials. For measurements at very low temperatures it is therefore essential to ensure a sufficient thermalisation of the sample before the actual experiment is performed. Otherwise the sample temperature decouples from the adjusted temperature of the cryostat leading to an artificially created behaviour recognizable by a constant drift in measurement parameters.
In order to estimate the corresponding relaxation rate of the glass sample, a simple thermalisation measurement was conducted. The temperature of the cryostat is thereby changed stepwise and held constant over a long period of time for a single step. By doing so, the sample temperature adapts to this variation according to its internal relaxation time scale. By measuring the real part or the dielectric loss as a function of the measuring time the actual temperature of the sample can be observed and an estimation for the glass relaxation time scale can be given.

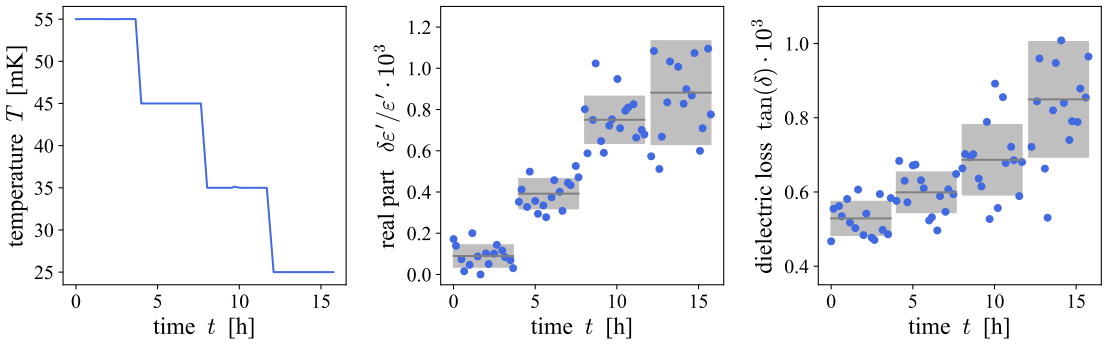

Figure 4.1: Thermalisation measurement for different temperature steps at the lowest temperatures with a probe field of −91 dBm. The individual figures show the adjusted temperature of the cryostat (**left**) together with the dielectric real part (**middle**) and the loss (**right**) as a function of the measurement time. The mean value (dark grey line) and the 1σ-range (grey shaded area) is also marked for each temperature.

A corresponding measurement is shown in figure 4.1 for a stepwise decrease in the lowest temperature range as a function over time. The data was taken for an excitation of the probe field of −91 dBm to avoid saturation effects but simultaneously achieve a sufficient signal to noise ratio to reduce the measuring time enough to resolve possible thermalisation effects. The temperature of the cryostat was kept constant for a duration of approximately four hours and then automatically adjusted to the next temperature step as depicted in figure 4.1 (left). During this time the transmission of the resonator was constantly measured to extract the real part $\delta\varepsilon'/\varepsilon'$ (middle) and the loss $\tan(\delta)$ (right) of the dielectric function. Both quantities thereby demonstrate an almost direct adaptation to the variation in temperature. The single measurements scatter evenly around the calculated mean value for each temperature step without any visible drift. The corresponding glass relaxation time scale can therefore be approximated to be smaller than the measuring time of a single data point, which was about 15 minutes. To ensure proper thermalisation of the sample, all following measurements had at least 30 minutes time to thermalise after a change in temperature before the actual measurement started. The overall increase in the real part and the loss is the expected behaviour for the resonant contribution at low temperatures. A closer look at the temperature dependence of the dielectric function is given in section 2.5.1. The increasing uncertainty for lower temperatures, which is depicted as a grey area in figure 4.1 for the 1σ-range, is a result of the weak coupling of the resonator to the transmission line and the increasing width of the resonance. Measurements with high attenuations and high loss values take very long in order to reduce the signal to noise ratio to the desirable level.

4.2 Saturation experiments

A fairly standard equilibrium measurement to perform are driving field strength dependent saturation experiments of the dielectric loss. For many measurements it is important to disturb or excite the ensemble of tunneling systems as little as possible to extract the unperturbed parameters of the system. Of course, decreasing the amplitude of the driving field also decreases the obtained signal to noise ratio during a measurement. The two extremes have to be balanced out in order to produce reliable data. The saturation measurement thereby serves the purpose of determining the range, in which the low power limit from equation 2.105 can be applied.
The corresponding measurement is depicted in figure 4.2 (top) for different temperatures from 50 mK up to 300 mK. The expected behaviour of the dielectric loss under increasing probe power is described by equation 2.104 beginning with the low power limit at small field strengths and decreasing for higher values according to the given relation. The obtained data was fitted (solid lines) using equation 2.104 with the low power limit $\tan\delta_0$ and the critical field $\bar{F}_c$ as free parameters. For the low and intermediate power regime this yields a good description for the behaviour of the dielectric loss. Higher values of the probe power reduce the loss below the expected threshold for all measured temperatures. This could indicate the dependency on a higher order exponent in the high power regime, compared to the relation given in equation

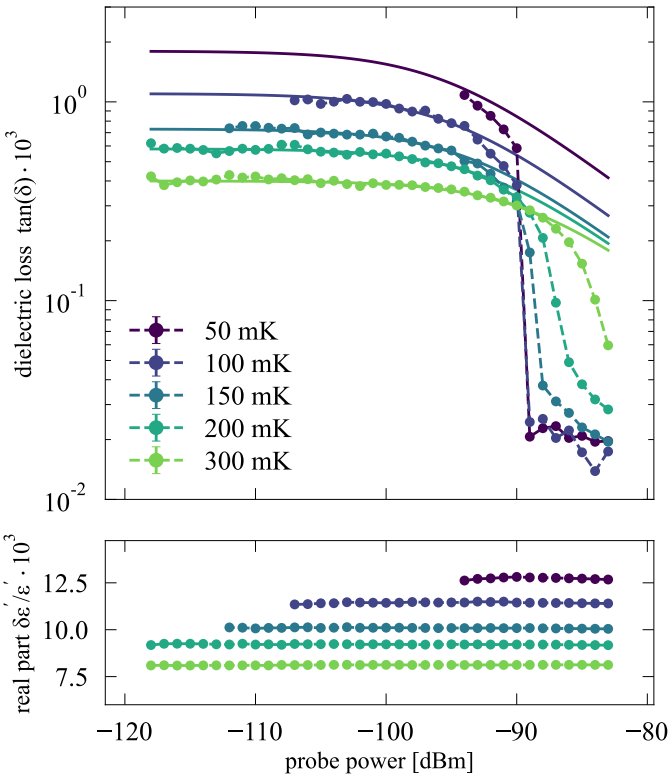

Figure 4.2: Driving field strength dependency of the real part (**bottom**) and dielectric loss (**top**). The measurement was performed for different temperatures from 50 mK to 300 mK. The data shows good agreement with the theoretical description for the saturation effect (solid lines) in the low and intermediate power regime. At higher powers the saturation is drastically enhanced and even displays a critical phenomenon for temperatures below 150 mK.

2.104. For lower temperatures this deviation from the theoretical progression sets in for even smaller field strengths. The resonance frequency and therefore the real part of the dielectric function remained unchanged under probe power variation, which is expected from theory and indicates that simple heating effects can be excluded. The corresponding plot is shown on the bottom in figure 4.2. Additionally, for decreasing temperatures a jump arises for saturation measurements below 150 mK, for which the loss is abruptly reduced by more than an order of magnitude. This behaviour is highly unexpected for the dependency of the driving field strength and can not be explained by the equations derived within the standard tunneling model. The sudden jump thereby implies a critical phenomenon below 150 mK around a probe power of approximately −89 dBm. For higher temperatures the jump vanishes, but the increased saturation effect in the high power regime remains.

4.3 Temperature dependence

This section discusses the temperature dependence of the dielectric properties for the experimental resonator setup. Furthermore, this is an important measurement to verify that the sputter deposited thin film layer of SiO_2 contains an ensemble of TLS and therefore follows the expected behaviour of an amorphous structure. Section 4.2 already showed the characteristic saturation effect for the dielectric material in dependence on the applied probe field strength. The corresponding measurement in figure 4.2 can be used to determine a suitable probe power for the temperature dependent measurement. The field strength should thereby be adjusted large enough in order to obtain a sufficient signal to noise ratio but small enough to disturb the ensemble as little as possible. For this measurement the excitation power was hence adjusted to −95 dBm.
Figure 4.3 shows the obtained data for a temperature dependent measurement from 20 mK to 6.5 K. The values below 1 K were thereby obtained in two successive measurements from 20 mK to 50 mK and from 50 mK to 850 mK, whereas the high temperature data was taken in a separate run without the circulating ^{3}He/^{4}He-mixture from 1.5 K to 6.5 K. The curvature of the resonant contribution in the real part hereby indicates the deviation from the logarithmic dependency predicted by the standard tunneling model. The solid line in figure 4.3 shows the theoretical description of the STM with a modified distribution function according to the extension

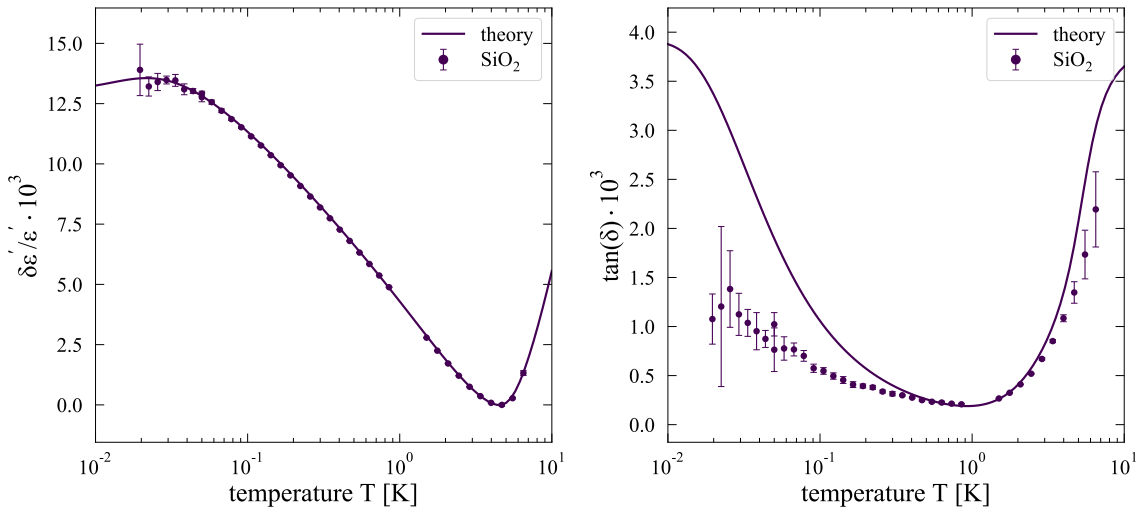

Figure 4.3: Temperature dependence measurement of the dielectric function from 20 mK to 6.5 K with −95 dBm input power on the transmission line. The real part (**left**) and the dielectric loss (**right**) show the characteristic behaviour of an amorphous material. The solid line shows the theoretical prediction from the standard tunneling model.

made by [Bur95] as

$$\tilde{P}(E,\Delta_0)\mathrm{d}E\mathrm{d}\Delta_0 = P(E,\Delta_0)\left(1-\frac{2\pi}{3}P_0U_0\log\left(\frac{W}{E+k_\mathrm{B}T}\right)\log\left(\frac{W}{\Delta_{0,\min}}\right)\right)\mathrm{d}E\mathrm{d}\Delta_0. \tag{4.1}$$

This modification takes into account a long-range interaction between the dipoles of the TLS, for which U_0 quantifies the interaction constant. The so called crossover temperature W/k_B is hereby a scale for a change of excitation type from tunneling states to high excitation modes.
With the modification, the theoretical model is able to describe the real part of the dielectric function well. Table 4.1 displays the corresponding values for the numerical integration of the STM. The loss on the other hand deviates from the expected behaviour especially for the resonant contribution at lowest temperatures. When compared to the saturation measurement in figure 4.2, this can be ascribed to the fact that the measurement at $-95\,\mathrm{dBm}$ is not fully in the low power loss limit. The corresponding deviation could therefore originate from a saturation of the systems by the probe field, which has its biggest contribution at lowest temperatures. A measurement with lower probe power was not possible because of the high coupling quality factor of the resonator. The signal to noise ratio was to low for small temperatures, for which the intrinsic quality factor of the resonator would be very small.

$A = P_0p^2/(\varepsilon_0\varepsilon_r)$	$K_1[\mathrm{J}^{-3}\mathrm{s}^{-1}]$	$K_2[\mathrm{K}^{-7}\mathrm{s}^{-1}]$	$\tau_2[\mu\mathrm{s}]$	P_0U_0	W/k_B [K]
$6.25\cdot10^{-3}$	$1.2\cdot10^{76}$	10	1	0.005	5

Table 4.1: Utilized parameters for the derivation of the theory curve in figure 4.3 for the standard tunneling model. The limits for the numerical integration were chosen as $\Delta_{0,\min}/k_\mathrm{B} = 10^{-3}\,\mathrm{K}$ and $E_\mathrm{max}/k_\mathrm{B} = 100\,\mathrm{K}$.

4.4 Pump-tone measurements

Additionally applied pump-tones can saturate tunneling systems in a specific frequency band around the pump-tone frequency, similar to the simple power dependency measurements. This modifies the occupation difference of the corresponding systems and therefore their contribution to the dielectric function. The influence of a single pump-tone on the resonator parameters were investigated in several experiments, for example [Kir17, Cap20, Fre21], which also provided theoretical descriptions by the off-resonant saturation of the TLS-ensemble.
This section presents measurements under the influence of two additional off-resonant pump fields and their impact on the resonator parameters. This opens a wide parameter space for an investigation of the tunneling systems behaviour under the applied fields. The following measurements were performed with symmetric or asymmetric arrangements of the pump-tones with respect to the resonance frequency. This setup shows interesting new limits, which are discussed in section 4.4.3.

4.4.1 Temperature dependency with symmetric pumps

The previous section showed the temperature dependence of the real part and the dielectric loss. This measurement was repeated with the additional application of two pump-tones of equal field strength. It is convenient to define the two pump-tones by their centre frequency

$$f_\mathrm{c} = \frac{f_\mathrm{p1} + f_\mathrm{p2}}{2} \tag{4.2}$$

and their detuning

$$\delta\omega = \frac{f_\mathrm{p2} - f_\mathrm{p1}}{2} \qquad \text{with} \qquad f_\mathrm{p2} > f_\mathrm{p1}. \tag{4.3}$$

The quantities f_p1 and f_p2 represent hereby the excitation frequencies of the pump-tones. For this measurement they were chosen to be symmetrically around the resonance frequency ($f_\mathrm{res} = f_\mathrm{c}$) and detuned by $\delta\omega = \pm 10\,\mathrm{MHz}$. Figure 4.4 shows

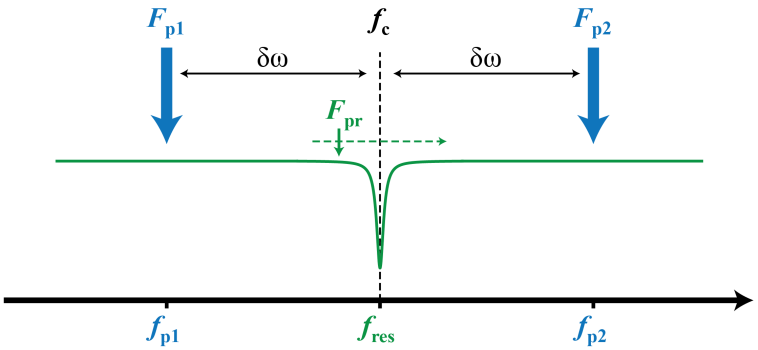

Figure 4.4: Schematic illustration of the symmetric arrangement for the temperature dependent measurement with two pump-tones.

a schematic of the corresponding frequency setup with the probe field F_{pr} for the NWA-sweep (green) and the two additional pump-tones of field strengths F_{p1} and F_{p2} (blue). Experimentally the pump field was injected into the bias line as already mentioned in section 3.2.2 in order to not saturate the utilized HEMT amplifier at higher pump fields. The resonator response was read out as before through the feedline in transmission. By the application of the symmetric configuration to the resonator, the resonance frequency was slightly shifted to higher values until an equilibrium value was reached. This could be caused by the asymmetry of the resonant contribution $b'(\omega, \omega_0)$ to the real part of the dielectric function or simply a mismatch of the pump-tone strengths. Tunneling systems with a larger resonance frequency have a positive contribution to the in phase component and systems with a smaller resonance frequency a negative one. If the corresponding systems are saturated, the overall contribution to the real part could be reduced, which on the other hand increases the resonance frequency of the resonator. Another explanation could be a small local heating effect through the application of the pumps and thus a related shift in resonance frequency, but since the real part is almost unchanged this scenario alone is unlikely. The shift in resonance frequency due to temperature was compensated experimentally by an algorithm of the measurement program to readjust the pumps around f_{res} after a change in resonance frequency to ensure the symmetry of the pumps before the actual start of the measurement.
Figure 4.5 shows the corresponding measurement with different field strengths for the pump-tones. The data is compared with the measurement from section 4.3 with-

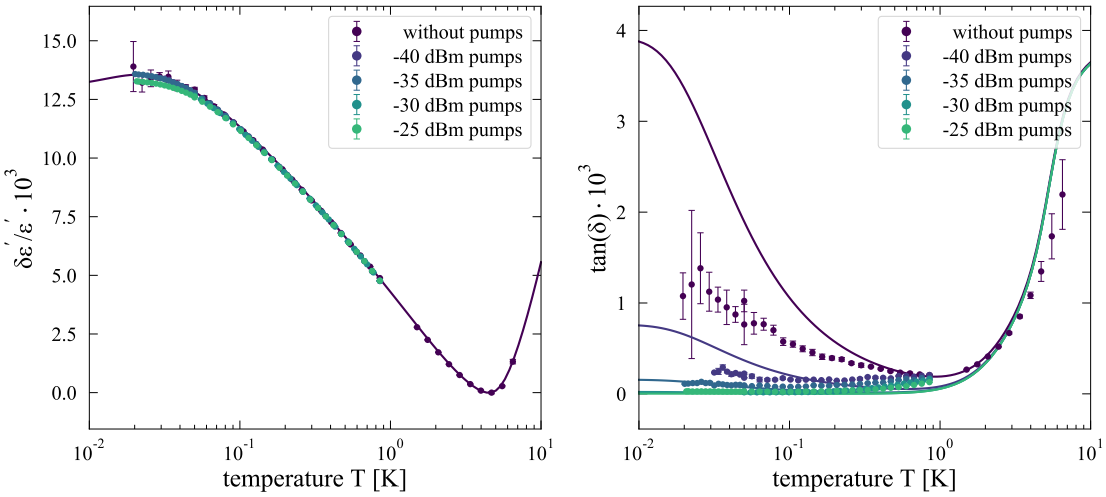

Figure 4.5: Temperature dependence of the dielectric function with additionally applied symmetric pumps. The real part (**left**) is almost unchanged under the influence of the pump fields, whereas the resonant dielectric loss (**right**) is reduced due to the saturation caused by the detuned pump-tones.

out additional pump signals. The temperature ranges from 850 mK to 20 mK to focus on the resonant contribution of the tunneling systems to the dielectric function. The real part $\delta\varepsilon'/\varepsilon'$ shows almost no dependence on the applied pump power. All relative values are thereby normalized to the minimal value of the measurement without pump-tones. This can be explained similar as above by the shape of the function for the resonant contribution $b'(\omega, \omega_0)$. For symmetrically applied pump signals negative and positive contributions are cancelled out almost equally through saturation. In addition, the value of the real part consists of contributions from different frequencies. The in-phase component is therefore unchanged under two symmetric pump-tones. Only at high field strength and low temperatures a small deviation can be observed, which originates either from the slight asymmetry of $b'(\omega, \omega_0)$ or a small but insignificant heating effect. The dielectric loss $\tan(\delta)$, on the other hand, is drastically reduced for increasing field strengths of the pump-tones. Similar to the *hole burning* experiments, the additional fields saturate tunneling systems in a frequency range around f_{p1} and f_{p2} respectively. For strong pump fields this effect can grow large enough to saturate tunneling systems close to the resonance frequency of the resonator. Since these systems contribute mainly to the imaginary part of the dielectric function according to $b''(\omega, \omega_0)$, the loss is reduced for two symmetrically applied pump-tones.
This behaviour could be described by expanding the theoretical description of the STM for the dielectric loss by the saturation formula from equation 2.57. This would reduce the number of contributing tunneling systems by a factor according to the saturation in the frequency window of the resonator. An accurate description proved to be difficult. The main parameters for this equation, the critical power and the transversal relaxation rate, were therefore chosen as $P_{\mathrm{c}} = -93\,\mathrm{dBm}$ and $\tau_2 = 1\,\mu\mathrm{s}$ respectively. The value for P_{c} is comparable to the approximation of the power dependency measurement of figure 4.2, but the description of the saturation behaviour is still missing the full picture. Overall, the device shows more saturation than expected for the simple assumption of two separate *hole burning* events at f_{p1} and f_{p2}. The following section will introduce another measurement in order to understand this phenomenon better.

4.4.2 Symmetric detuning measurements

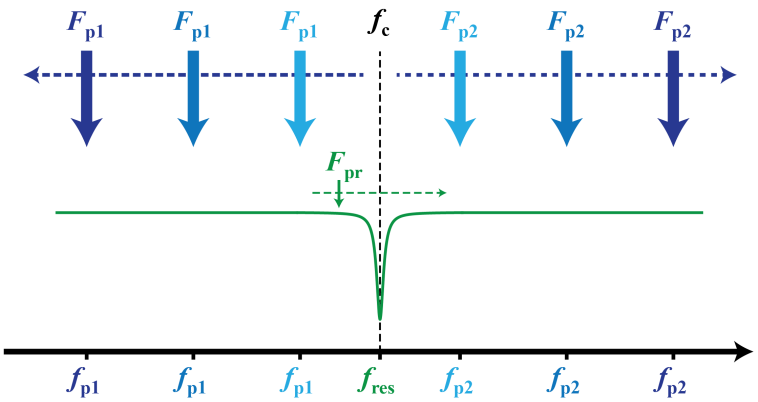

Figure 4.6: Schematic illustration of the symmetric arrangement for the detuning dependent measurement with two pump-tones. Each shade of blue represents the adjustment of the two pump-tones with different detuning.

In order to study the influence of the detuning parameter on the resonance curve and explicitly on the dielectric loss, an additional measurement was performed at a constant temperature of 35 mK. A schematic illustration of the pump-tone arrangement is depicted in figure 4.6. The measurement starts at a symmetric ($f_{\mathrm{res}} = f_{\mathrm{c}}$) detuning of $\delta\omega = 0.5\,\mathrm{MHz}$, which is increased until the resonator parameters remain unchanged. This increase of the detuning parameter $\delta\omega$ is illustrated in figure 4.6 by three shades of blue, which represent three different pump-tone arrangements. This measurement is repeated for various values of the pump field strength in the range from $-50\,\mathrm{dBm}$ to $-25\,\mathrm{dBm}$. The corresponding data is depicted in figure 4.7 for all twelve measurements as the loaded quality factor Q of the resonator in dependence of the detuning $\delta\omega$. Its value is maximal for a small detuning and decreases for higher values. This behaviour is expected, if the measurement is understood as two *hole burning* events around the two pump frequencies. For larger detuning the saturation in the frequency range of the resonator is decreased and thereby also the quality factor.
A theoretical description for the saturation of two symmetric pumps can be derived with equation 2.57, which yields the relation

$$R_{\mathrm{Sat}}(\delta\omega) = R_0 \left(1 - \frac{(F_{\mathrm{ac}}/F_{\mathrm{c}})^2}{1 + (F_{\mathrm{ac}}/F_{\mathrm{c}})^2} \frac{1}{1 + \tilde{\tau}_2{}^2 \delta\omega^2}\right) \tag{4.4}$$

for the saturation at resonance frequency caused by a pump field detuned by $\delta\omega$. The frequency dependent term stemming from the line shape function in equation 2.57 hereby neglects the second term for simplicity. This equation can be used to define a saturation factor R_{Sat}/R_0, which modifies the intrinsic quality factor Q_{i} of the resonator. The loaded quality factor can now be described by

$$Q(\delta\omega) = \left(\frac{1}{Q_{\mathrm{c}}} + \frac{1}{Q_{\mathrm{i}}} \left(\frac{R_{\mathrm{Sat}}(\delta\omega)}{R_0}\right)^2\right)^{-1}. \tag{4.5}$$

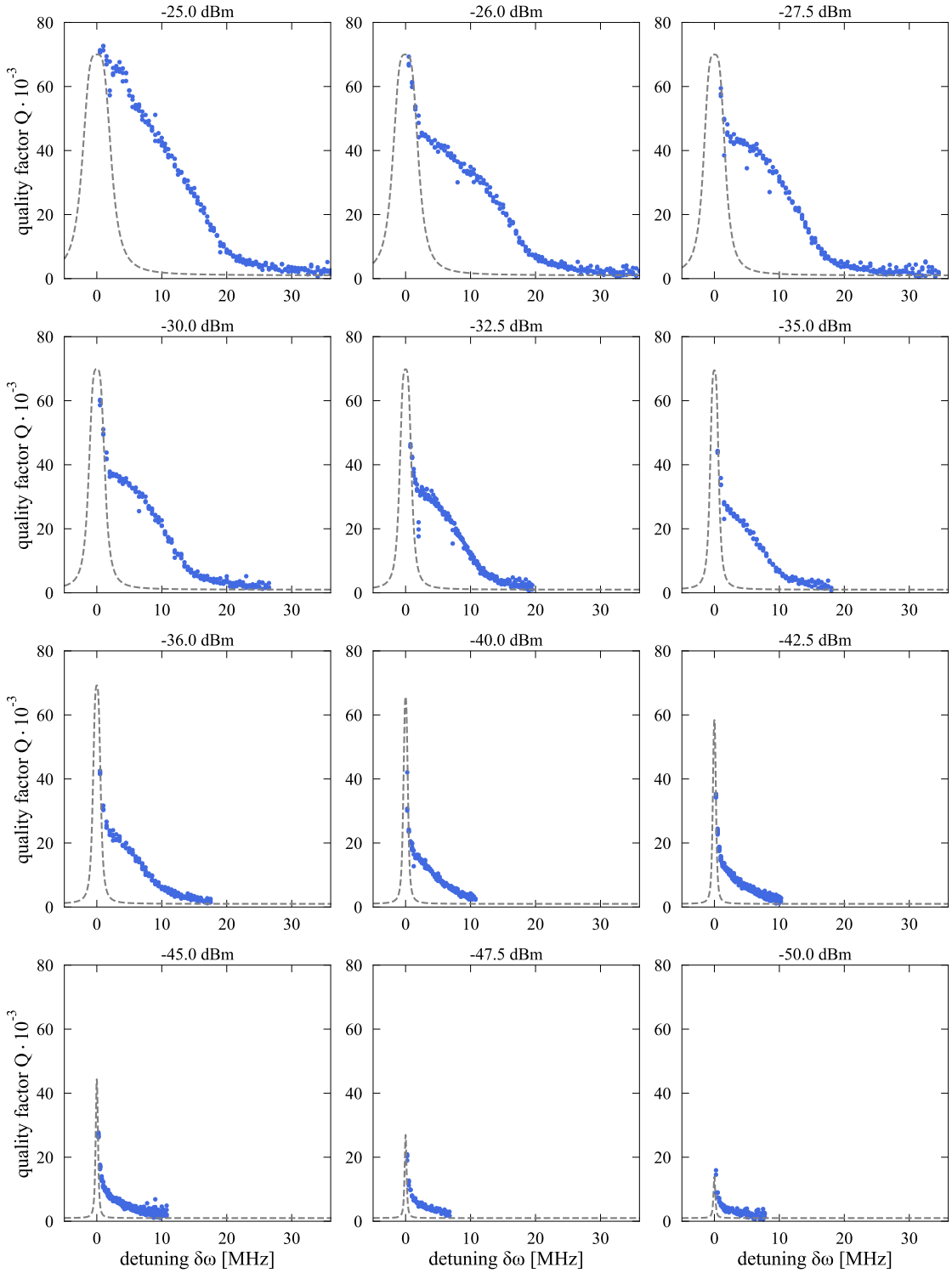

Figure 4.7: Enhancement of the quality factor with symmetric pumping in comparison to the expected behaviour for 35 mK. $Q_c = 70000$, $Q_i = 1000$, τ_2 =5 µs and F_{ac}/F_c was scaled for the lowest pumping powers and then relayed according to the experimentally used value, starting with $F_{ac}/F_c \approx 1.8$ for -50 dBm.

For small values of the detuning, the saturation factor is minimal and the loaded quality factor approaches the coupling constant Q_c of the resonator setup. For larger detuning the saturation effect can be neglected and the intrinsic loss Q_i contributes fully to the total value. Equation 4.5 was used to describe the measured data in figure 4.7 (grey dotted line) for different values of the pump field strength. The parameters were chosen as $Q_\mathrm{c} = 70000$, $Q_\mathrm{i} = 1000$ and $\tau_2 = 5\,\mu\mathrm{s}$ for all measurements. Note that the deviation of Q_c from the determined values in table 3.1 can be caused by additional sources of intrinsic loss besides TLSs [McR20], which are not included in this description. The ratio of the pump field strength to the critical field was selected as $F_\mathrm{ac}/F_\mathrm{c} \approx 1.8$ for the lowest pump power of $-50\,\mathrm{dBm}$ and scaled according to the experimentally used value for all other measurements. For small detuning the theoretical prediction fits the experimental data, but for increasing pump power the quality factor is enhanced over an order of magnitude compared to the expected behaviour under two individual pump-tones. At higher detuning the quality factor converges around the equilibrium loss limit, which corresponds to Q_i in the limit $Q_\mathrm{c} \gg Q_\mathrm{i}$. This outcome is interesting, since the TLS-ensemble seems to be saturated over a broader frequency range than expected for the simple assumption within the standard tunneling model. An interpretation of the broad peak as simple *hole burning* would yield a relaxation time scale shorter than $0.1\,\mu\mathrm{s}$, which does not coincide with comparable experimental results. The observed characteristic of the additional enhancement, especially for higher pump powers, therefore suggests the formation of a secondary mechanism besides simple saturation. An explanation for this effect requires a deeper understanding of the resonator's properties, which will be given in the following sections.

4.4.3 Asymmetric detuning measurements (f_c-sweep)

For values of the pump power above −25 dBm the symmetric detuning measurement proved to be difficult. Unlike the case of smaller field strengths, for which the real part was nearly unchanged, the resonance frequency started to shift to higher frequencies under the symmetric pump arrangement. A rearrangement of the pump-tones around the new resonance frequency led to a further increase of f_{res}. In order to understand the observed behaviour better, a different measuring technique was used, which revealed the emergence of two new limits for the resonator response in the regime of higher pump powers. The results of these investigations are presented in this section.

The utilized technique is an asymmetric detuning measurement, for which the centre frequency of the two pump-tones is swept over the resonator's response function. A schematic illustration for this measurement arrangement is depicted in figure 4.8. In this case the detuning $\delta\omega$ is kept constant and the two pump frequencies are increased by the same amount during the measurement. For each setting of the pump-tones a resonance curve is determined with the weak probe field F_{pr} of the NWA, which is indicated by the green dashed arrow in figure 4.8. With fixed detuning the measurement can therefore be described by the change in centre frequency f_c, which equals the change of a single pump frequency. The measurement will therefore also be referred to as a centre frequency sweep or f_c-sweep.

In the following, different asymmetric detuning measurements are presented as an example for the emerging limits. If not otherwise stated, the detuning was chosen as $\delta\omega = 5\,\mathrm{MHz}$ and only the centre frequency f_c was changed. As already mentioned, the resonance frequency f_{res} started to increase above a pump power of −25 dBm. An asymmetric detuning measurement was therefore performed from $f_c = 1033.55\,\mathrm{MHz}$ to 1033.70 MHz in steps of 2 kHz with both pump-tone powers at −23 dBm. The corresponding measurement is shown in figure 4.9 for three selected traces of the resonance curves. The traces show the three scenarios, in which the centre frequency

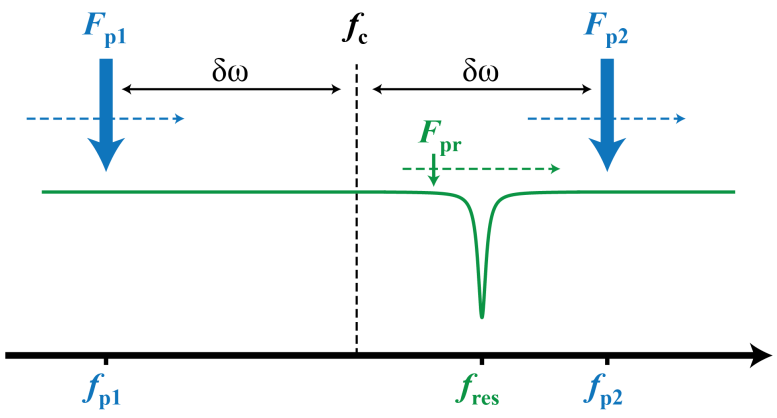

Figure 4.8: Schematic illustration of the asymmetric arrangement for the detuning measurement with two pump-tones. The pump frequencies are simultaneously increased between the individual measurements of the resonators response.

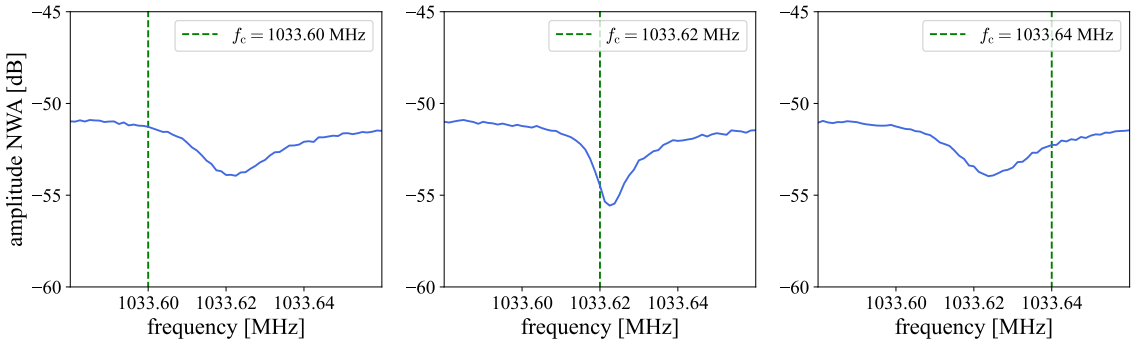

Figure 4.9: Three exemplary traces of the asymmetric detuning measurement with both pump powers at −23 dBm. The resonance curves show three scenarios, for which f_c is smaller (**left**), approximately equal (**middle**) and above (**right**) the resonance frequency f_{res}. For $f_c \approx f_{res}$ the resonance frequency is shifted slightly and the quality factor is increased approximately by a factor of two.

is smaller (left), approximately equal (middle) and above (right) the resonance frequency f_{res}. At the beginning of the measurement and for all centre frequencies below 1033.60 MHz, the resonance curve remains unchanged under the variation of f_c. In the frequency range, where $f_c \approx f_{res}$ holds true, the resonance frequency is slightly shifted to higher values and the quality factor is increased approximately by a factor of two. With increasing centre frequency the resonance returns to its previous position and restores the former quality factor.
The entire asymmetric detuning measurement is depicted in figure 4.10 in a two-dimensional colour plot. The individual traces of the NWA are shown in dependence of the centre frequency f_c. The amplitude of the NWA signal is represented by the colour legend on the right. Each vertical slice in figure 4.10 therefore corresponds to a single trace of the resonators transmission signal. Three of those slices were shown in figure 4.9. The horizontal blue area represents the notch-type resonance around a frequency of approximately 1033.62 MHz. The green solid line illustrates the centre frequency of the two pump signals. In the range, for which the centre frequency is close to the resonance frequency, the narrowing of the resonance curve is visible through the darker shade of blue and the slight constriction of the blue area. In this form of presentation the influence of the two pump-tones on the transmission curve can be estimated to be confined on a frequency range of approximately 10 kHz. It is worth mentioning that the two applied pump-tones are far detuned from the resonance frequency in comparison to the resonators width. The centre frequency is thereby just a constructed value without a corresponding field strength to illustrate the position and the asymmetry of the pumps. The fact that the parameters of the resonator are changed in a small frequency range, however, demonstrates the crucial role of the symmetric pump arrangement. The increase in resonance frequency and

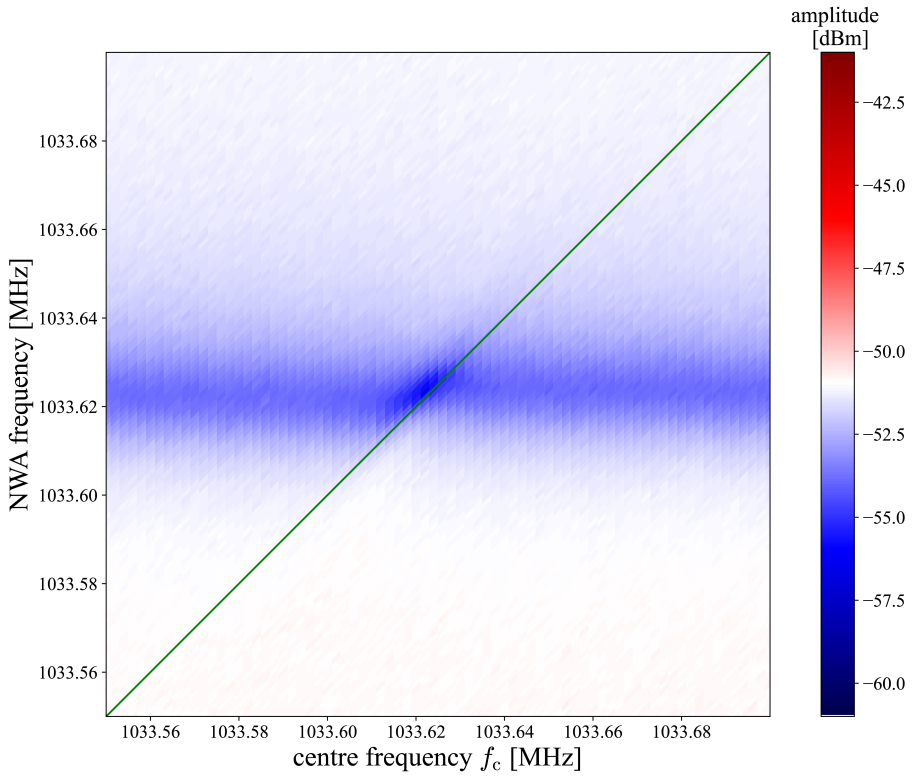

Figure 4.10: Colour plot of the asymmetric detuning measurement with a pump power of $-23\,\mathrm{dBm}$. The centre frequency was varied from $f_c = 1033.55\,\mathrm{MHz}$ to $1033.70\,\mathrm{MHz}$ in steps of $2\,\mathrm{kHz}$ for a detuning of $\delta\omega = 5\,\mathrm{MHz}$. A vertical slice in this style of presentation represents a single NWA-measurement with a specific pump-tone arrangement. The colour code quantifies the observed amplitude with a blue shade for the resonance dip. The position of the centre frequency f_c is represented by the green solid line.

in quality factor could, of course, also be related to a heating effect caused by the applied pump powers, but a frequency selective effect in such a narrow range is quite uncharacteristic.

For the next measurement, the pump power was increased further to $-19\,\mathrm{dBm}$ at the external bias line. The detuning remained unchanged at $\delta\omega = 5\,\mathrm{MHz}$ and the centre frequency was increased from $f_c = 1033.72\,\mathrm{MHz}$ to $1033.78\,\mathrm{MHz}$ in steps of $0.5\,\mathrm{kHz}$. Similar to above, a selection of fifteen NWA-traces from this measurement are shown in figure 4.11 for different values of the centre frequency f_c. Starting below the resonance frequency $f_c \ll f_{res}$ the response function of the resonator is almost unchanged under the influence of the two pump-tones. With increasing values of the centre frequency, but still $f_c < f_{res}$, the resonance frequency is slightly decreased. This behaviour is opposite to the previous measurement and hence makes simple heating effects as the sole explanation more unlikely. The resulting convergence of f_{res} towards f_c caused the resonance response to significantly increase in quality fac-

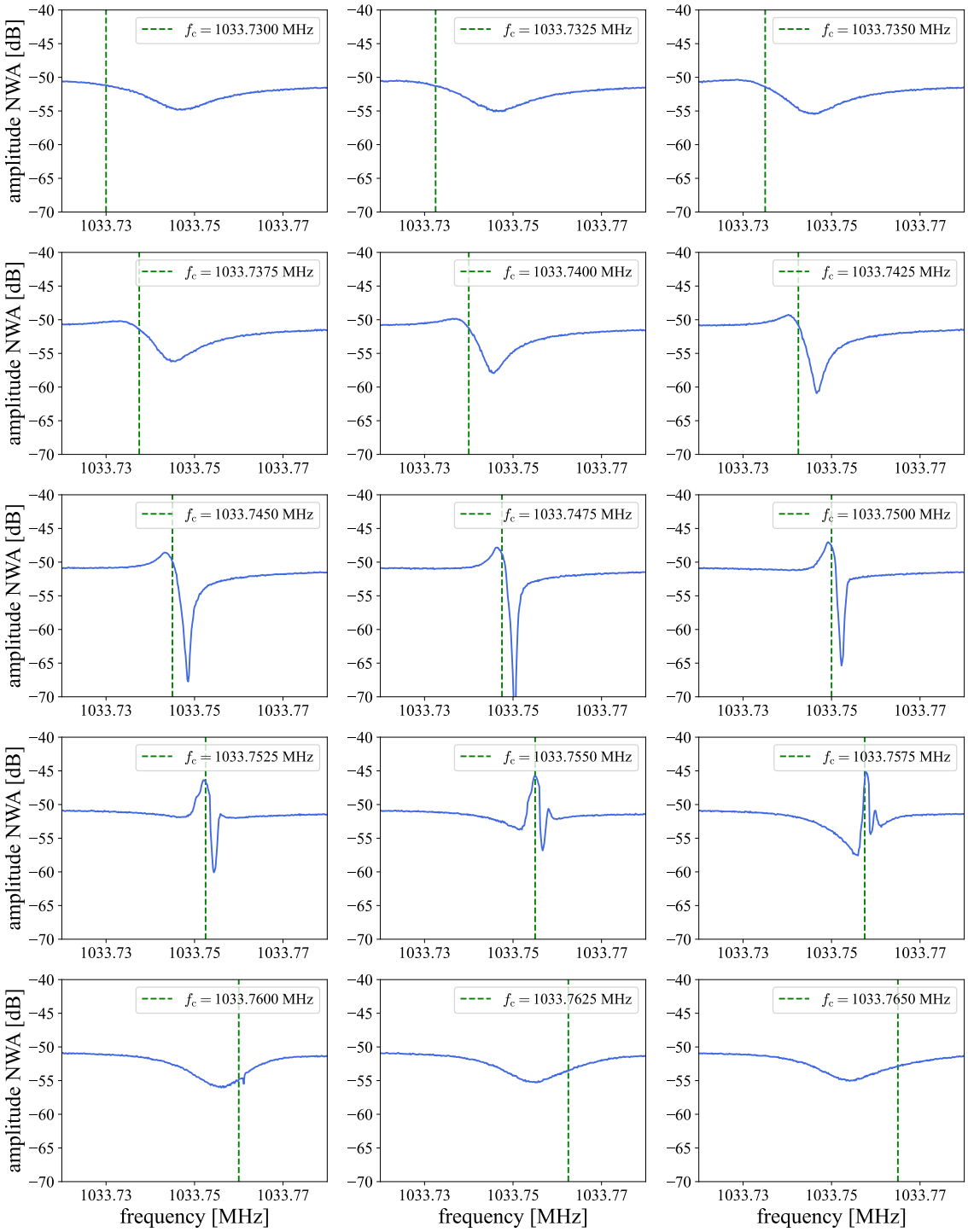

Figure 4.11: Fifteen selected traces of the asymmetric detuning measurement with both pump powers at −19 dBm. The individual plots show the resonators response function under the influence of the two pump-tone arrangement. The green dotted line represents the position of the centre frequency for each measurement.

tor and simultaneously in asymmetry of the curve until $f_c \approx f_{res}$ is reached. For a further increase of the centre frequency $f_c > f_{res}$ the resonators response is not describable by the simple Lorentzian type model and shows multiple extrema before it transitions back into the shape of the unperturbed resonance curve. The corresponding colour plot is depicted in figure 4.12 in dependence of the centre frequency. This representation clearly shows the increase in quality factor by the dark blue shaded area, for which $f_c \approx f_{res}$ is fulfilled. Interestingly, the resonance frequency follows the centre frequency (green solid line) slightly detuned for a while until the unperturbed resonance response is restored. The frequency range, in which f_c influences the asymmetric detuning measurement, is approximately 30 kHz. Compared to figure 4.10 the impact of the centre frequency on the resonance response is clearly visible, which is presumably caused through the application of the stronger pump fields. The resonator mode seems to interact in a specific frequency range with the two pumps,

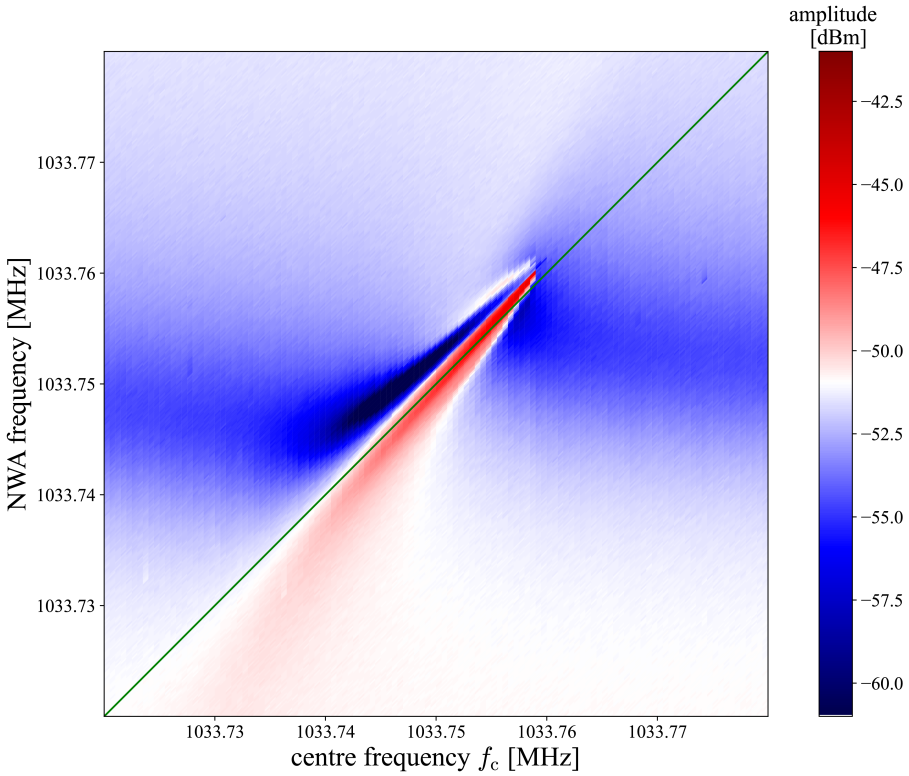

Figure 4.12: Colour plot of the asymmetric detuning measurement with a pump power of −19 dBm. The centre frequency was varied from $f_c = 1033.72$ MHz to 1033.78 MHz in steps of 0.5 kHz for a detuning of $\delta\omega = 5$ MHz. A vertical slice in this style of presentation represents a single NWA-measurement with a specific pump-tone arrangement. The colour code quantifies the observed amplitude with a blue shade for smaller signals than the background (white) respectively a red shade for larger values. The position of the centre frequency f_c is represented by the green solid line.

dependent on the position of the centre frequency f_c. The symmetric arrangement of the pumps around f_{res} thereby plays an important role for the observed effect, but there is still no full explanation on the behaviour of the resonators response to this measurement method. The enhancement of the resonators left flank as shown in figure 4.11 or respectively by the darker red shape in figure 4.12 could be caused by an *image frequency* from the position of the centre frequency f_c. This phenomenon is induced, if a frequency response is mixed with another signal, in this case the centre frequency, to create a mirrored version of the original response. This explanation could only hold true, if somehow a signal with the frequency f_c is produced inside the resonator during the application of the pumps. A spectral investigation in the corresponding frequency range revealed no additional signal at f_c, but this attempt at explanation will become clear in the following section, in which a measurement with further increased pump-tone strength is presented.

Observation of an additional peak

For a further increase of the pump power, the behaviour of the resonators response changed. In this measurement limit a spectral investigation of the resonators frequency range showed the appearance of an additional signal during the f_c-sweep. Figure 4.13 displays the corresponding measurement for an applied pump power of $-15\,\mathrm{dBm}$ as ten selected traces each for the network analysers (left column) respectively the spectrum analysers amplitude (right column). It is worth mentioning, that during the measurement with the spectrum analyser only the output port of the transmission line was investigated, while no signal was applied to the input port. At the beginning of the measurement, the NWA-trace displays a similar behaviour when the centre frequency approaches the resonance frequency, but in contrast to the lower pump powers f_{res} starts to increase so that the condition $f_c \approx f_{res}$ can not be fulfilled any more. The amplitude of the NWA thereby shows an additional signal at the centre frequency f_c. In this limit the sweep continues over a wider frequency range of approximately 200 kHz until the resonance suddenly jumps back to its original position and the additional signal disappears. This behaviour is similar to the response of a non-linear Duffing-type resonator with an additionally applied pump-tone signal as presented in section 2.6.3. The strong excitation modifies the resonance frequency of the system, which can be measured with a weak probe field. An increase of the pump-tone frequency causes the resonance frequency to be pushed to higher values as long as the pump-tone increased according to the non-linear response function. If the pump-tone exceeds the jumping point, the resonance frequency returns to the unperturbed position.
The corresponding spectra draw a similar picture. If the condition $f_c \approx f_{res}$ is met during the sweep, an additional very narrow line appears at the frequency value of f_c.

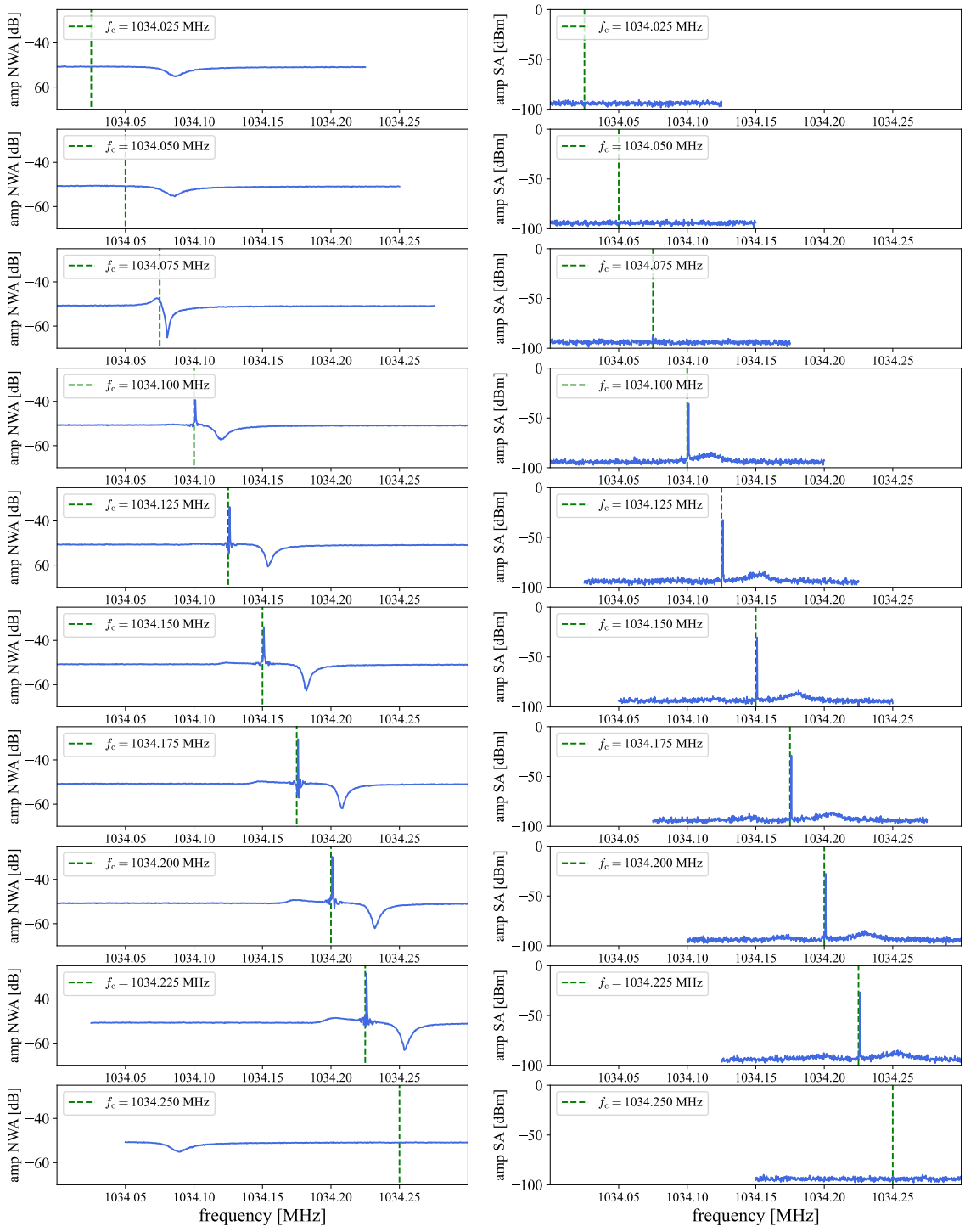

Figure 4.13: Ten selected traces each for the network analyser (left) respectively the spectrum analyser (right) of the asymmetric detuning measurement with both pump powers at −15 dBm. The individual plots show the resonators response function and the corresponding spectrum under the influence of the two pump-tone arrangement.

This signal remains until the resonator response jumps back to its original position. The trace of the spectrum analyser also reveals another much broader peak, which corresponds to the position of the resonators response of the NWA-trace. Hence, the resonator is emitting photons into the transmission line in the frequency window of the resonance even if the only active external signals are the two far detuned pump-tones. An illustration of the full spectrum with the excitation pulses will be shown in a following section. Another even smaller peak arises during the f_c-sweep at lower frequencies for the NWA-traces as well as for the SA-traces. This effect will become clear in the following paragraphs as an image of the resonators response induced by the mixing with the strong emission signal at f_c.
The entire measurement was performed from $f_c = 1034.00\,\text{MHz}$ to $1034.30\,\text{MHz}$ in steps of $1\,\text{kHz}$ and is depicted in figure 4.14 as a colour plot. A single vertical slice represents the individual NWA-traces exemplary shown in the left column of figure 4.13.

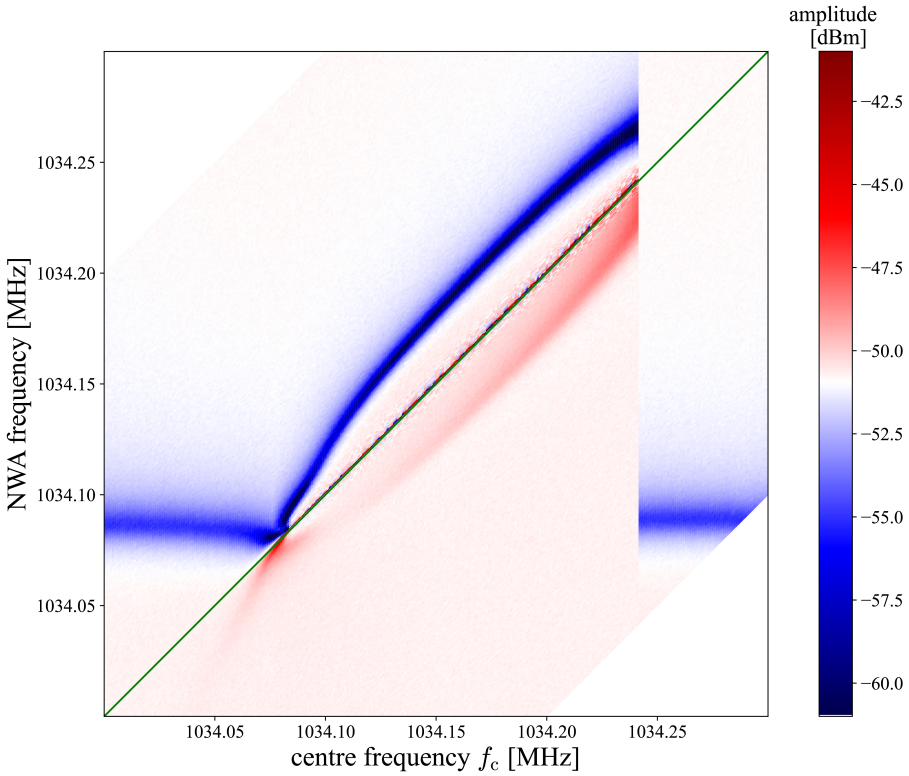

Figure 4.14: Colour plot of the asymmetric detuning measurement with a pump power of $-15\,\text{dBm}$. The centre frequency was varied from $f_c = 1034.00\,\text{MHz}$ to $1034.30\,\text{MHz}$ in steps of $1\,\text{kHz}$ for a detuning of $\delta\omega = 5\,\text{MHz}$. A vertical slice in this style of presentation represents a single NWA-measurement with a specific pump-tone arrangement. The colour code quantifies the observed amplitude with a blue shade for smaller signals than the background (white) respectively a red shade for larger values. The position of the centre frequency f_c is represented by the green solid line.

The blue line shows the resonance frequency of the resonator setup and the green solid line the centre frequency of the two pump-tones. This style of presentation shows the decrease in resonance frequency in the beginning of the f_c-sweep until the condition $f_c \approx f_{res}$ is shortly fulfilled around $f_c = f_{res} = 1034.08\,\text{MHz}$. Afterwards, the resonance frequency is increased again and stays above the value of the centre frequency, until it suddenly jumps back into the unperturbed position before the measurement started. The red shape in figure 4.14 can hereby be understood as the *image frequencies* of the blue frequency response line. The additional emission line arises after the condition $f_c \approx f_{res}$ is fulfilled and vanishes after the response jumps back to the unperturbed position. A more precise evaluation of the amplitude will also be given in the following pages. The overall appearance of the additional emission peak is quite interesting since it is a very strong narrow line comparable to the pump-tones from the individual signal generators. This is quite unexpected since the random properties of the TLS-ensemble with the broad distribution of parameters would give rise, if at all, to a very broad emission. This aspect will also be discussed in the following sections, which aim to give a possible explanation for this effect.
The corresponding spectrum analyser measurement is depicted in figure 4.15 as a colour plot. The colour scale was hereby adjusted for a better visualisation of the side maxima, since the narrow emission peak would otherwise be to bright. It displays a similar pattern as figure 4.14, but the spectrum shows no contributions until f_c and f_{res} align for the first time. The arising emission pattern evolves continuously until it is abruptly terminated as soon as the response function jumps back to its original position. The narrow emission peak is thereby always exactly in the middle of the two pump-tone frequencies f_{p1} and f_{p2}. The arising signal almost seems to be clocked by the generator signals. If the two pump-tones are applied directly in the frequency window, in which the emission would be expected to take place (approximately 1034.08 MHz to 1034.24 MHz for the case of the previous experiment), without conducting a full f_c-sweep, the emission would arise either randomly or when an external source (for example the NWA-signal) triggers the effect. This is a further indication for a stimulated emission effect inside the sample material. It is also worth mentioning, that the generation of this intermediate frequency $(f_{p1} + f_{p2})/2$ is also non-trivial for an intermodulation product of two individual rf-signals. Moreover, if simple frequency mixing would cause this effect it should work in a wide frequency domain and not just in a small window of about 200 kHz. The emission line therefore seems to originate from a different mechanism involving the symmetric arrangement of the pump-tones and the resonator setup. The amplitude of the narrow emission peak is depicted in figure 4.16 in dependence of the centre frequency f_c. It resembles the evaluation of the maximal amplitude of the single spectra, which corresponds to the straight line following f_c in figure 4.15. The power values displayed in this plot are the absolute quantities measured by the spectrum analyser at the output

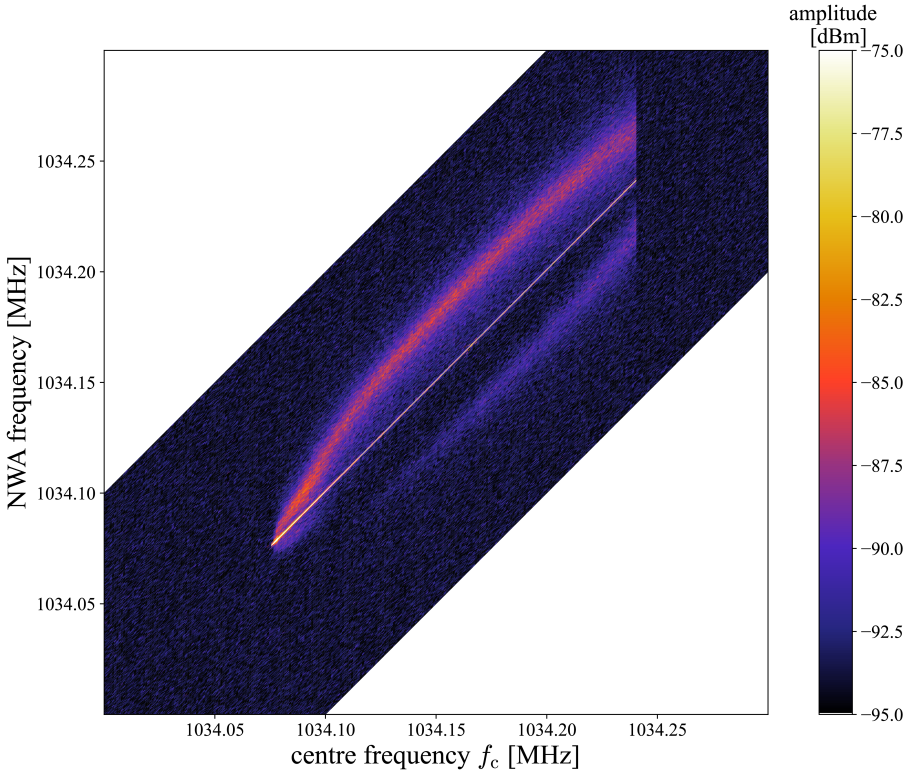

Figure 4.15: Colour plot of the asymmetric detuning measurement with a pump power of $-15\,\mathrm{dBm}$. The centre frequency was varied from $f_c = 1034.00\,\mathrm{MHz}$ to $1034.30\,\mathrm{MHz}$ in steps of $1\,\mathrm{kHz}$ for a detuning of $\delta\omega = 5\,\mathrm{MHz}$. A vertical slice in this style of presentation represents a single SA-measurement with a specific pump-tone arrangement. The colour code quantifies the observed amplitude of the spectrum analyser.

side of the transmission line. It is difficult to calculate a reliable value for the actual field strength since the coupling of the fields to the transmission line ($\approx -50\,\mathrm{dB}$), the quality of the bond connection, the attenuation of the cables ($\approx -7\,\mathrm{dB}$), the additional attenuator ($\approx -3\,\mathrm{dB}$), and the total amplification ($\approx +78\,\mathrm{dB}$) are mostly approximated values. It is important to keep these quantities in mind when describing the occurring effects, but the absolute amplitude resembles a more significant value. Figure 4.16 shows a steep incline of the amplitude during the variation of the centre frequency of a few kHz. As already mentioned, the effect first sets in once the condition $f_c \approx f_{res}$ holds true. Afterwards, the occurring emission seems to get stabilized, while $f_c < f_{res}$, and its amplitude flattens towards higher values of the centre frequency. As soon as the resonance frequency jumps back to its original position, $f_c < f_{res}$ is fulfilled and the emission vanishes. The data can be described by the theory presented in section 2.6.3 for the Duffing oscillator (red solid line). The amplitude of the emission line is thereby characterized by the response amplitude of the non-linear resonator for a strong excitation field of frequency f_c. The occurring

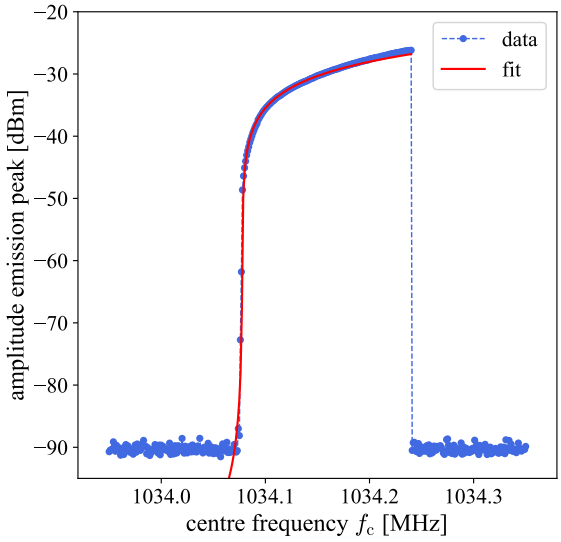

Figure 4.16: Maximal amplitude of the narrow emission peak in dependence of the centre frequency. The data was taken from the individual spectra from the asymmetrical detuning measurement. The fit (red) is derived from the Duffing model with two excitation frequencies.

emission peak hence drives the resonator in the non-linear regime. Since the Duffing model describes the behaviour of the data well, the strength of the underlying emission, which would correspond to the excitation strength γ_1 in section 2.6.3, can be assumed to be approximately constant during the f_c-sweep. The appearing effect caused by the two pump-tones is therefore stable under frequency variation and can be understood as an additional narrow peak at the centre frequency f_c. The dependence of the emission amplitude on f_c as in figure 4.16 is only the result of the response caused by crossing the resonator window.
Under the assumption that the emission peak functions as a strong excitation field and the NWA sweep as a weak probe field, the obtained data from figure 4.14 can be modelled by the theory presented in section 2.6.3. The resonance frequency is thereby shifted due to the arising emission peak following equation 2.134. The modified resonance frequency according to the Duffing model (yellow dotted line) is depicted in figure 4.17 with the emission peak amplitude from figure 4.16 as the response amplitude $z_1(f_c)$, which yields

$$\tilde{f}_{\text{res}} = \sqrt{f_{\text{res}}^2 + \frac{3}{8\pi^2}\beta z_1^2(f_c)}\,. \tag{4.6}$$

At first, the resonance frequency is unchanged, but with increasing values of $z_1(f_c)$ it shows a kink similar to the obtained resonator data visible in blue. At higher values of f_c the curves deviate, since the Duffing theory predicts an approximately linear increase of the resonance frequency at these values. Another effect is thus affecting the position of the resonance and is therefore important to understand the observed behaviour.
If the emission peak is understood as an additional pump as introduced in the theoretical description of the Duffing resonator with two excitation tones in section 2.6.3,

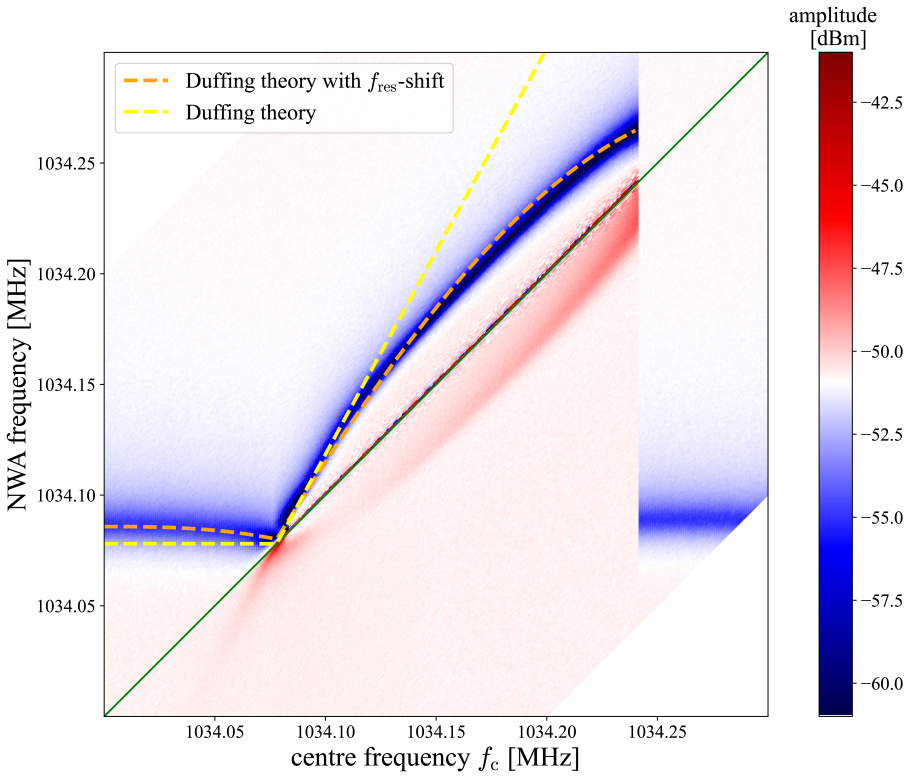

Figure 4.17: Colour plot of the asymmetric detuning measurement with a pump power of −15 dBm. The data is equivalent to figure 4.14 with the theoretical description of the resonance frequency according to the Duffing model (yellow) and the Duffing model with an additional frequency shift caused by the occurring emission line (orange).

the position of the resonance frequency is additionally modified by the corresponding saturation effects. In [Sch18, Cap20, Fre21] it was shown that a single pump-tone can shift the resonance frequency towards the frequency of the pump. The same effect modifies the behaviour of the resonance frequency in this case. To simulate this effect, equation 4.6 for the position of f_{res} from the Duffing theory was replaced by the arbitrary relation

$$f_{res}(f_c) = f_{res,0} - a(f_c - f_{c,i})^b \tag{4.7}$$

to include the shift in resonance frequency for a pump at lower frequencies. The dependence on f_c hereby corresponds to the increasing frequency of the emission peak during the measurement, which pulls the resonance more and more towards the position of the centre frequency. The parameter a is a scaling factor, b the exponential factor, $f_{res,0}$ is the unperturbed value of the resonance frequency and $f_{c,i}$ the starting value of the f_c-sweep for the measurement. With this extension, equation 4.6 describes the behaviour of the resonator rather well as depicted in figure 4.17 by the orange dotted line. The slight decrease at the beginning of the measurement, the

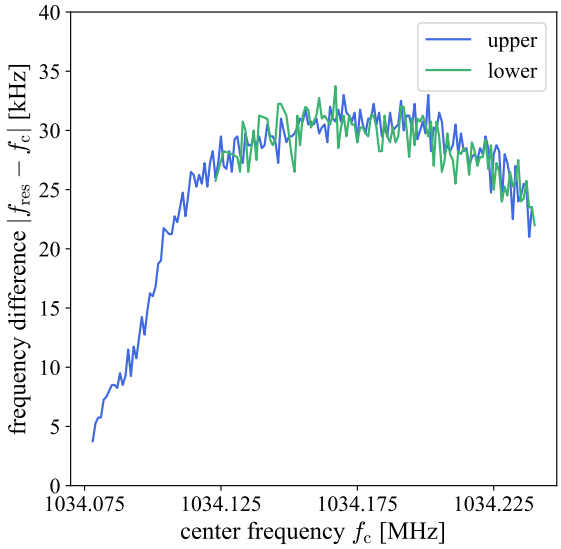

Figure 4.18: Frequency difference between the position of the upper, respectively the lower, side maxima in comparison to the narrow emission peak in dependence of the centre frequency. The evaluation was done for each individual spectrum of the asymmetric detuning measurement

emerging kink where the emission peak arises and the curvature at higher values of f_c are in good agreement with the data. It is worth mentioning, that the applied approximation is just an arbitrary function for the well know property of shifting resonance frequencies due to a strong pump-tone. The derivation of a physically more justified expression would require more knowledge of the system parameters in order to integrate over the entire distribution of TLSs to extract the corresponding dependence. The phenomenological approach with an arbitrary function was therefore more straightforward in this case for the description of the underlying behaviour. Figure 4.14 showed an additional feature for frequencies below f_c, which was visible in this style of presentation as a shadow (red) of the original resonator response (blue). This effect also appeared in the spectral measurement shown in figure 4.15 as a signal with smaller amplitude than the resonators emission. The appearance of this second response can be explained by the intermodulation product of the resonators response with the narrow emission peak. These *image frequencies* are visible in the spectrum as well as in the response of the NWA measurement. In order to prove this, figure 4.18 compares the distance of the upper and the lower position of the broad side peaks for each spectrum in dependence of the centre frequency. The two curves align perfectly since the lower maxima are the mirrored version of the upper resonator response. That is also why the lower maxima are smaller and only visible for stronger amplitudes of the emission peak. The observed effect can therefore be understood as the direct interaction of the additionally occurring emission with the resonator field.

All measurements so far were conducted for the same detuning of $\delta\omega = 5\,\mathrm{MHz}$. Figure 4.19 shows the asymmetric detuning measurement for different values of the detuning parameter from $\delta\omega = 1\,\mathrm{MHz}$ up to $20\,\mathrm{MHz}$. The obtained spectra were evaluated for the amplitude of the narrow emission peak (left), the amplitude of the

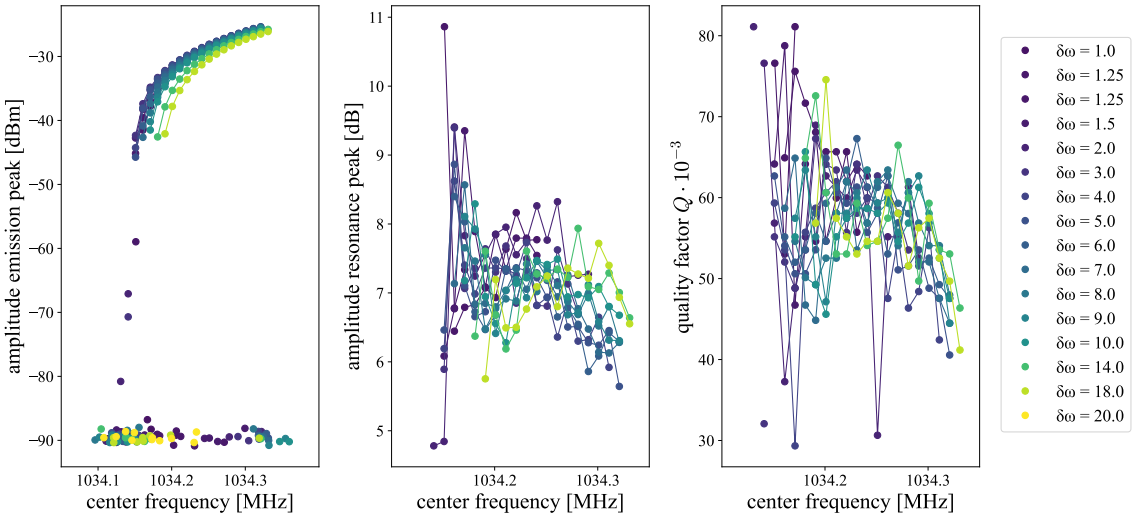

Figure 4.19: Different f_c-sweeps in dependence of the detuning $\delta\omega$ in MHz. The plot shows the amplitude of the emission peak (**left**), the amplitude of the resonator peak (**middle**) and the thereto related quality factor Q of the resonator (**right**).

resonance peak (middle) and the quality factor of the resonance peak (right) all in dependence of the centre frequency. The amplitude of the emission peak shows a similar behaviour for all adjusted values. Only the frequency, for which the emission emerges, increases slightly for higher detuning. This is a consequence of the different positions of the resonance for a changing pump-tone arrangement. For a detuning smaller than 1 MHz or higher than 20 MHz this limit could not be found again. This is interesting, since the amplitude of the emission peak seems to be rather independent on the applied detuning, but the underlying mechanism occurs only in a defined parameter space. A more detailed evaluation of the limiting parameters is given in section 4.6. The amplitude and the quality factor of the spectral resonance appear to be almost constant during the f_c-sweep with a drop of to higher values. The evaluation in the beginning is thereby difficult due to the fact that the emission peak aligns with the resonance. This causes both quantities to fluctuate strongly in the beginning. The average quality factor of about $6 \cdot 10^4$ is thereby comparable to the values obtained in the symmetric detuning measurements from figure 4.6. This indicates that the intrinsic loss is vanishingly small during the f_c-sweep and the remaining width of the resonance is dominated by the coupling quality factor.

4.5 Non-linear resonator characteristic

In order to understand the mechanisms that lead to the generation of the additional emission line, another important feature needs to be understood. By applying the two pump-tones to the resonator system the difference frequency

$$\Delta f = |f_{\mathrm{p1}} - f_{\mathrm{p2}}| \tag{4.8}$$

can be found in the lower frequency spectrum. This behaviour substantiates the non-linear characteristics of the resonator setup, since the mixing of frequencies is caused by higher order terms in the amplitude response of the corresponding differential equation. A frequency spectrum including the regions of interest is depicted in figure 4.20 a) for the lower frequency part of Δf and the frequency range of the pump-tones. The two large peaks thereby correspond to the externally applied pump fields and the smaller peak in between to the additional peak in the limit of emission. The enlarged version of the lower frequency range (b) respectively the frequency

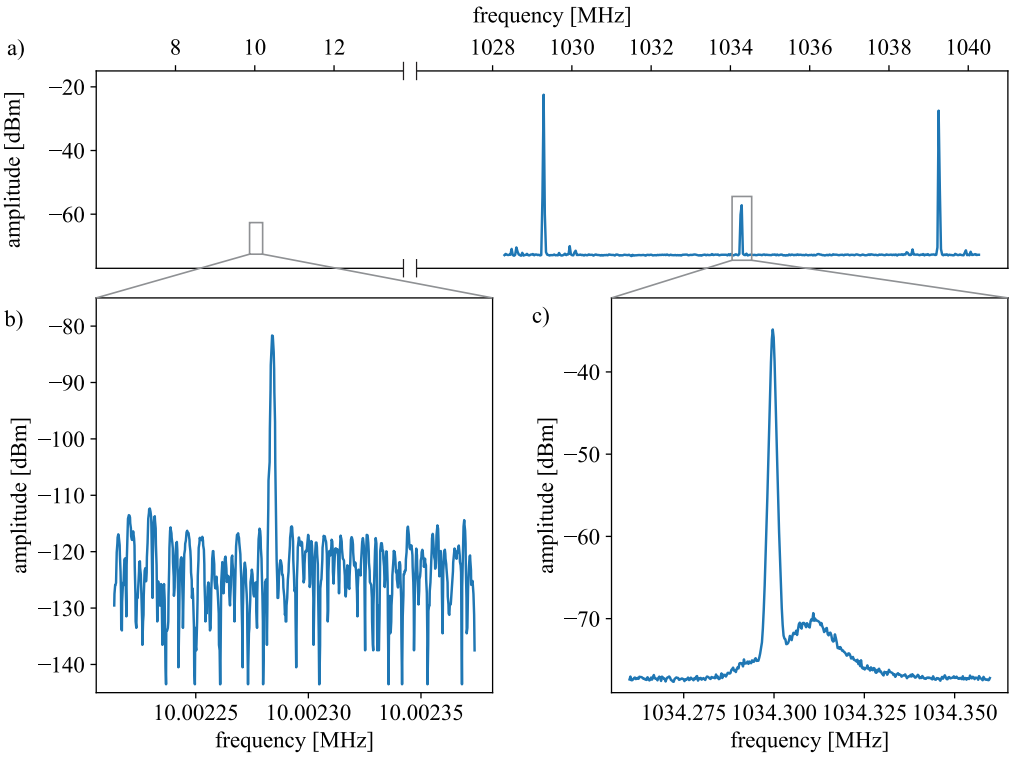

Figure 4.20: Frequency spectra during the emission limit. The spectrum (a) shows the regions of interest with the lower and higher frequency window. The enlarged versions depict the range of the difference frequency Δf (b) and the emission peak (c) in more detail. The measurement was conducted with a pump power of $-10\,\mathrm{dBm}$ and a detuning of $\delta\omega = 5\,\mathrm{MHz}$ at a temperature of $35\,\mathrm{mK}$.

window of the resonator (c) with the emission peak and the underlying resonator response are also shown. The difference frequency is very weak in comparison to the pump-tones and the emission line, but since the experimental setup is optimized for rf-fields the additional attenuation at lower frequencies mainly causes this deviation, as presented in section 3.2.4.
The strength of the difference peak is directly dependent on the power of the applied pump-tones. Figure 4.21 shows this dependency for a detuning of $\delta\omega = 5\,\mathrm{MHz}$ at a temperature of 35 mK. With higher pump power P the strength of the difference frequency peak increases. A linear fit of the form

$$f(x) = a + b \cdot x \tag{4.9}$$

for the obtained data of the difference peak amplitude reveals a relating factor of $b = 2.05$, which directly corresponds to the associated exponential factor of the non-linearity. The effect can therefore be related to a first order non-linearity. The measurement was repeated for different values of detuning from 1 MHz to 36 MHz to verify this observation and showed no deviation from the quadratic behaviour. Only the offset parameter a varies slightly for different detuning, which is also a result of the changing attenuation of the cable for the transmission of low frequency signals. This non-linearity is unchanged under temperature variation up to a few Kelvin. Simulations in [Mün21] showed that the difference frequency can be generated by an ensemble of tunneling systems through their intrinsic non-linearity. This frequency mixing process is also independent of the occupation number and still active for a fully saturated TLS-ensemble. The corresponding higher frequency mixing terms could also be found at approximately 2 GHz as a result of mixing, which creates frequencies at $2f_{\mathrm{p1}}$, $2f_{\mathrm{p2}}$ and $f_{\mathrm{p1}} + f_{\mathrm{p2}}$. The appearance of the difference frequency Δf could therefore be a result of the non-linear properties of the tunneling systems.

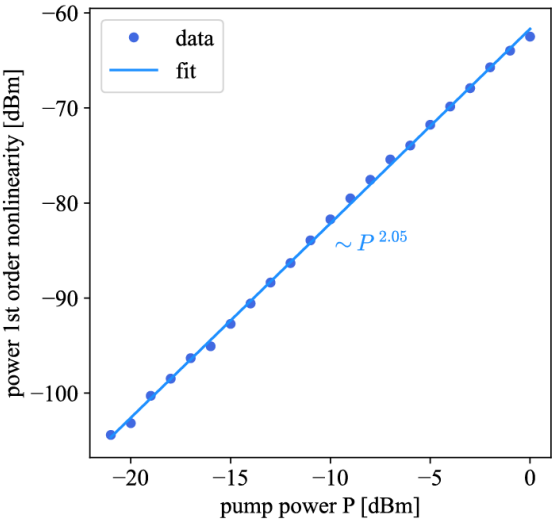

Figure 4.21: Dependency of the difference frequency peak power on the applied pump-tone power. The detuning was set to $\delta\omega = 5\,\mathrm{MHz}$ and the temperature of the cryostat was at 35 mK. A linear fit yielded a corresponding exponential factor of approximately 2.05, which corresponds to a first order non-linearity.

Moreover, the low frequency contributions of Δf can be understood as an additional field in the resonator setup. With sufficient strength the difference frequency could thus modify the energy splitting of individual tunneling systems as a bias field according to the Landau-Zener theory. This self-induced bias effect would then cause transitions of the TLSs into an excited state for a passage of a pump-tone. For the right conditions, this could lead to a population inversion in the frequency window of the resonator and a thereby associated stimulated emission effect. The presence of an additional bias field could also explain the enhanced quality factor in the symmetric detuning measurements of section 4.4.2. A continuously modulated energy splitting could broaden the arising *burned hole* due to the constantly shifting tunneling systems. The resonator therefore experiences the effect of the saturated systems over a wider frequency range, which leads to a higher quality factor. The idea of a self induced bias field outlines the investigation of the observed effect for the emission limit in the following sections.

4.6 Parameter space of the emission limit

In order to understand this phenomenon better, the emission limit was investigated for a variation of measurement parameters. The detuning of the pump-tones $\delta\omega$ and their strength P_p thereby seemed to influence the appearance of the effect the most. Several f_c-sweep measurements were performed to determine, if the emission limit emerged for a certain configuration of detuning $\delta\omega$ and pump-tone strength P_p. These measurements are depicted in figure 4.22 for different temperatures from 20 mK to 300 mK. The coloured area thereby represents the region, in which an emission limit was found in the frequency spectrum independent of its strength. The pump-tone strength covers values from −20 dBm to 0 dBm for the applied power outside the cryostat. The lower temperatures showed heating effects visible in the base temperature of the cryostat for increasing pump-tone field strengths. This mainly concerns the measurements at 20 mK and 45 mK, which were therefore interrupted as soon as the deviation was noticed. Higher temperatures showed no direct increase during the measurement but the heat input caused by the application of the two pump-tones remains present. The area, for which the emission limit can be observed, opens up after a certain threshold value of the pump-tone strength P_p

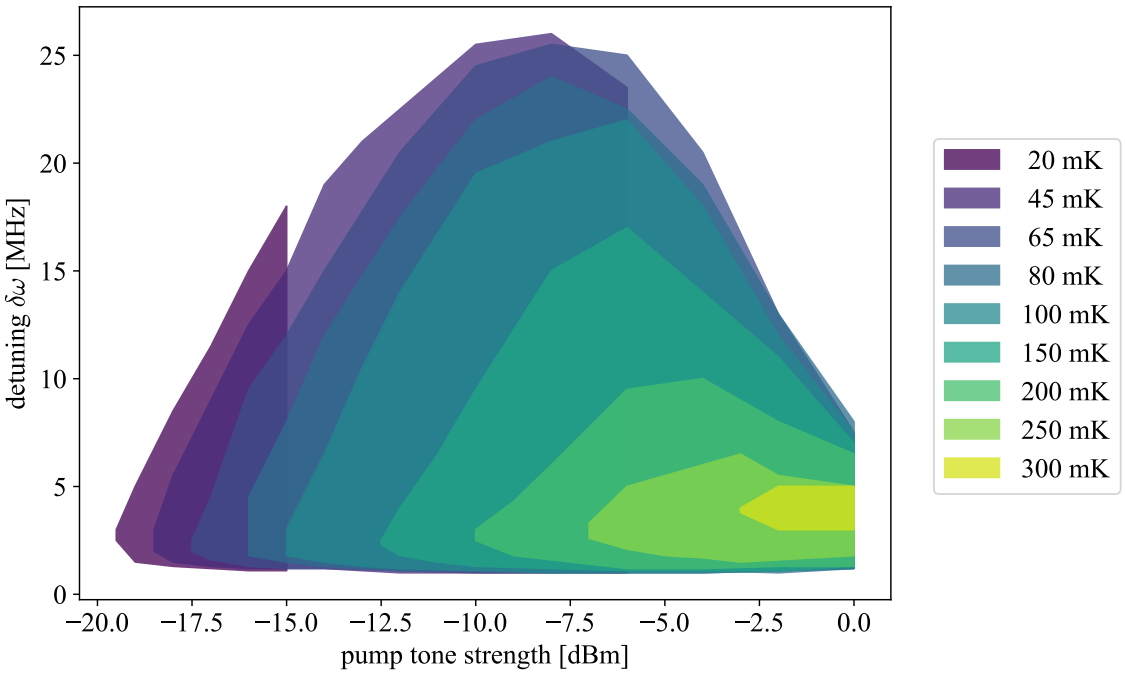

Figure 4.22: Illustration of the parameter space, for which the emission limit can be found. Several f_c-sweep measurements were performed to determine the limit borders of the observed effect in dependence of the detuning $\delta\omega$, the pump-tone power P_p and the temperature.

for each temperature. The range of possible detuning values widens with increasing power P_p. For values above $-10\,\mathrm{dBm}$ the detuning range is reduced again up to the highest applied pump-tone strength of $0\,\mathrm{dBm}$. The largest possible detuning for all measurements was approximately $25\,\mathrm{MHz}$. For small detuning values the emission vanishes mostly below $1\,\mathrm{MHz}$. The area is surrounded by a small belt of approximately $0.5\,\mathrm{MHz}$ respectively $1\,\mathrm{dB}$, in which the resonance is altered by the occurring interactions similar to figure 4.12, but no emission can be found in the frequency spectrum. The parameter space of the emission limit is therefore bound to a certain set of conditions dependent on the detuning $\delta\omega$ and the pump-tone strength P_p. A simple frequency mixing due to an electric non-linearity is hence fairly unlikely, which would not be bound to a particular frequency window in order to occur. Additionally, higher temperatures reduce the area of possible parameter space in figure 4.22 significantly. The absolute amplitude is thereby also reduced, which is depicted in figure 4.23 for a measurement with a detuning of $\delta\omega = 5\,\mathrm{MHz}$ and a pump power of $-10\,\mathrm{dBm}$ in direct dependence on temperature. The quantity represents the strength of the emission peak outside the cryostat measured with the spectrum analyser. The amplitude of the emission peak decreases with increasing temperatures until it completely vanishes above $175\,\mathrm{mK}$. This suggests that the occurring phenomenon might be related to the interactions of the pump-tones with the resonator through the TLS-ensemble in the frequency domain of $1\,\mathrm{GHz}$. In thermal equilibrium (see equation 2.21) the TLSs of these frequencies would start to saturate for temperatures above $50\,\mathrm{mK}$. Under the assumption of a dynamical process through the occurrence of a self biasing effect, this could additionally modify this critical temperature value. The consequential saturation of tunneling systems with increasing temperature would thereby reduce the occurring emission, until it vanishes above a few hundred mK. This dependency is therefore a further indication for the involvement of TLSs to the observed effect.

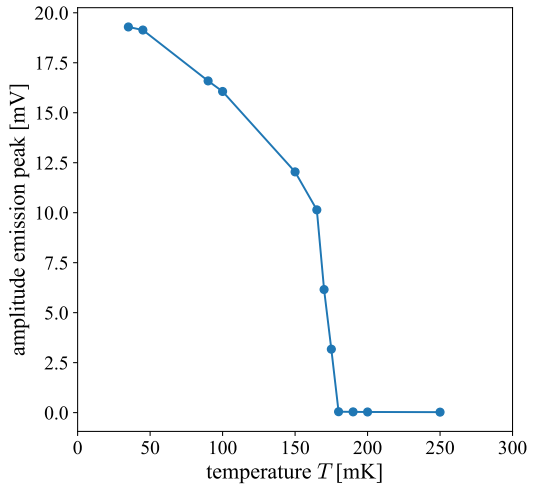

Figure 4.23: Measurement of the amplitude of the emission peak in dependence on temperature for a detuning of $\delta\omega$=5 MHz and a pump power of $-10\,\mathrm{dBm}$. The emission limit can only be found for temperatures below $180\,\mathrm{mK}$. A decrease in temperature then causes a sharp increase in the emission amplitude towards lower temperatures.

4.6.1 Theoretical derivation of the boundary conditions

Following the previous measurement, this section defines the basic conditions in order to explain the set of possible parameters for the appearance of the emission limit. This approach assumes that the effect is caused by the Landau-Zener dynamic of an ensemble of tunneling systems interacting with the two pump-tones and the LC-resonator field. The basic idea was already outlined in section 2.7 and requires the contributing systems to be inverted into their excited state during the adiabatic passage of the pump-tone field caused by a bias field sweep. Afterwards, the excited state has to be preserved until the tunneling systems reach the frequency window of the resonator. The ground state can then be recovered by the stimulated emission of a photon at resonance frequency.
In order to derive the first boundary condition equation 2.84 from section 2.3.7 was used, which expressed the probability for an adiabatic transition of the two-level systems

$$P_{\mathrm{g}\to\mathrm{e}} = 1 - \exp\left(-\frac{\pi\Omega_{\mathrm{R,p}}^2}{\nu}\right). \tag{4.10}$$

This defines an upper limit $\nu_{\max} \approx \Omega_{\mathrm{R,p}}^2$ for the sweeping rate, which yields

$$\boxed{\dot{F}_{\mathrm{b}} < \frac{\hbar}{p}\Omega_{\mathrm{R,p}}^2 = \dot{F}_{\mathrm{b,max}}} \tag{4.11}$$

for the dependency of the bias rate. Otherwise, the transition from the ground state into the excited state is suppressed due to the rapid passage of the energy levels.
The lower limit is a result of the relaxation time τ_1. During the time of its transition the system has to be unaffected by relaxation effects to remain in the excited state. The available time to invert a TLS ($t_{\mathrm{inv}} \propto \Omega_{\mathrm{R,p}}/\nu$) is proportional to the width of the pump and to the inverse of the sweeping rate. This time scale consequently needs to be shorter than the relaxation time τ_1, so that the excited state does not directly decay. In addition, the sweeping rate has to be large enough to overcome the detuning $\delta\omega$ to reach the resonator window in the excited state. The lower limit can therefore be calculated by adding the two rates, which yields

$$\boxed{\dot{F}_{\mathrm{b}} > \frac{\hbar}{p}\frac{(\Omega_{\mathrm{R,p}} + \delta\omega)}{\tau_1} = \dot{F}_{\mathrm{b,min}}.} \tag{4.12}$$

For the case of a self induced bias effect as described above the value of the bias field strength F_{b} is no longer arbitrarily selectable. The strength is in this case determined by the pump-tone field F_{p} and the non-linearity of the system. The sweeping rate can hence be expressed as

$$\nu(F_{\mathrm{p}}) = 2\,\frac{p\dot{F}_{\mathrm{b}}(t, F_{\mathrm{p}})}{\hbar}\frac{\Delta}{E}. \tag{4.13}$$

The bias field strength is also important for the absolute shift in energy. The resonance window and at least one pump-tone have to be accessible for the corresponding systems via the bias sweep. Otherwise, the system can not contribute to the effect via inversion at the site of the pump and stimulated emission inside the resonator. For a given detuning $\delta\omega$ the approximation for an additional lower limit of the bias field strength is therefore

$$\delta\omega < \frac{pF_\mathrm{b}}{\hbar}. \tag{4.14}$$

For symmetric tunneling systems the bias field strength has to be even higher since the change in energy is much smaller compared to asymmetric TLSs. With an approximation for the derivative of the bias field

$$|\dot{F}_\mathrm{b}(t)| \approx \omega_\mathrm{b} F_\mathrm{b} = 2\delta\omega\, F_\mathrm{b} \tag{4.15}$$

and the relation for the bias voltage $V_\mathrm{b}(V_\mathrm{p}) = F_\mathrm{b}(V_\mathrm{p}) \cdot d$, equation 4.14 can be written as an additional upper limit for the case of a self induced bias effect

$$\boxed{\dot{F}_\mathrm{b} < 2\,\frac{p}{\hbar}\left(\frac{V_\mathrm{b}(V_\mathrm{p})}{d}\right)^2 = \dot{F}^{(\mathrm{nl})}_{\mathrm{b,max}}.} \tag{4.16}$$

The finite spectral width of the resonator also defines an additional lower limit due the fact that the pump-tones can not be arranged arbitrarily close together. If the pump-tone frequencies are near f_res, the resonator can be excited directly by the pump fields. The lower limit for an appropriate detuning is therefore defined by a factor $\Delta\omega_\mathrm{res}$ proportional to the spectral width of the resonator

$$\Delta\omega_\mathrm{res} < \delta\omega \tag{4.17}$$

The lower limit for the sweeping rate can hence be expressed by

$$\boxed{\dot{F}_\mathrm{b} > 2\,\Delta\omega_\mathrm{res}\,\frac{V_\mathrm{b}(V_\mathrm{p})}{d} = \dot{F}^{(\mathrm{nl})}_{\mathrm{b,min}}.} \tag{4.18}$$

This boundary is more of an experimental limit caused by the self induced bias effect and the thereby accessible bias rates. The emission limit can still occur for lower values of the bias rate, but the direct excitation of the resonator by the pump fields without the interaction through the TLS-ensemble would presumably prevail the arising effect.

4.6.2 Emission limit map

The derived conditions from section 4.6.1 can be used to formulate a theoretical description for the observed combination of system parameters that lead to the emission effect as depicted by figure 4.22. This was realized by a Monte Carlo simulation on an ensemble of 10000 TLS with random parameters of Δ and Δ_0 according to the distribution function of the standard tunneling model from equation 2.15. The conditions were checked for the individual systems and their contributions are added for every combination of bias rate $\dot{F}_\mathrm{b}$ and pump voltage V_p. This value also includes the factors for the thermal saturation and TLS coupling to the electric field. The lower limit, which is proportional to the spectral width of the resonator from the relation 4.18, was hereby excluded since this condition only defines an experimental

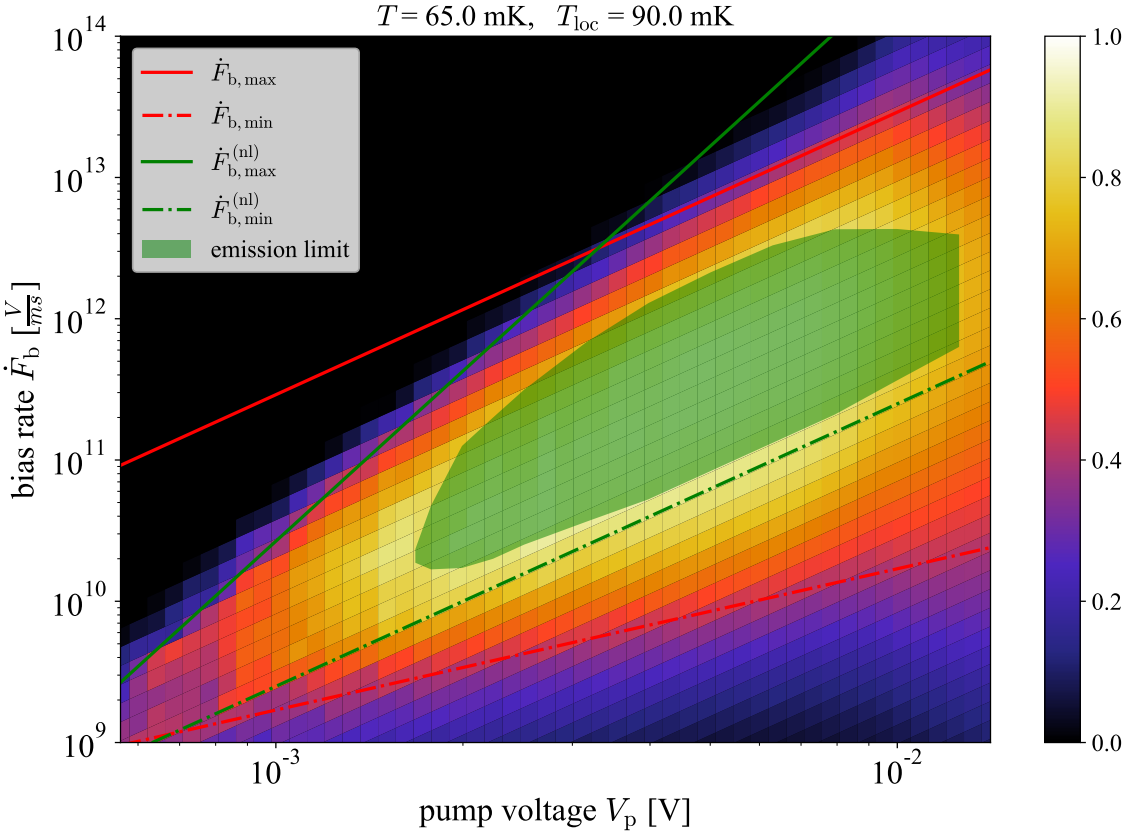

Figure 4.24: Illustration of the results from the Monte Carlo simulation for 65 mK. The colour bar shows the sum of all TLS contributions normalized to all systems, which are near the resonance during the bias sweep, for better comparison. Green and red lines represent the different boundaries for an average TLS with $\Delta_0/E \approx 0.6$ to contribute to the stimulated emission limit. The experimentally observed borders (green area) are depicted by converting the applied detuning to the corresponding bias rate.

boundary. The corresponding value for the entire ensemble is afterwards normalized to the number of systems, which pass the resonance frequency during the bias sweep. The resulting quantity represents the amount of TLSs, which contribute to the proposed mechanism instead of the total loss. The obtained value can therefore be used as a measure for the occurrence of the emission effect. Figure 4.24 shows the result of this simulation as a colour plot for a temperature of 65 mK. The colour bar thereby represents the arbitrary value for the contribution to the emission effect. It is normalized to the maximal value for better comparability. The green area is the experimentally observed region for which the emission effect could be found and the coloured lines represent the upper and lower limits derived in section 4.6.1 for an average TLS with $\Delta_0/E \approx 0.6$. The non-linearity is described by equation 4.9 with an exponential factor of $\tilde{b} = 2$ to meet the determined value in section 4.5 and an offset parameter $\tilde{a} = -25\,\mathrm{dB}$ to quantify the strength of the non-linearity on the chip in dependence on the applied pump power. The offset parameter $\tilde{a}$ was thereby varied to adjust the underlying theory to the experimental data. An additional parameter Q was used to describe the attenuation of the bias line including the cables, the bond connection and the coupling to the capacitor. The corresponding parameters are also shown in table 4.2.

The underlying theory is in very good agreement with the experimentally observed area of the emission limit. The shape is mainly determined by the derived limits of section 4.6.1 but for large values of the pump voltage V_p the area is reduced due to the small contributions of asymmetric TLSs. Large bias fields enable these systems to contribute according to the limits but their associated coupling to the electric field is much smaller than that of symmetric systems. The ratio of the total contribution to the number of accessible systems is therefore reduced. Measurements for the lowest temperatures showed heating effects with increasing pump-tone strength. This indicates that the local temperature of the sample is presumably higher compared to the adjusted temperature of the cryostat during the application of the pump-tones especially for the lowest temperatures. This local temperature T_loc can hence be decoupled from the temperature of the mixing chamber during the measurement.

p	d	$\tau_{1,\mathrm{min}} \coth(\frac{E}{2k_\mathrm{B}T})$	$\delta\omega_\mathrm{res}$	N_TLS	$\tilde{a}$	Q
4 D	300 nm	1 µs	0.3 MHz	10000	−25 dB	−25 dB

Table 4.2: Overview of the used parameters for the Monte Carlo simulation. The quantities are: dipole moment p, the distance of the capacitor plates d, the minimal relaxation time scale $\tau_{1,\mathrm{min}}$ in dependence of temperature, the spectral width of the resonator $\delta\omega_\mathrm{res}$, the number of simulated TLSs N_TLS, the offset parameter for the non-linearity $\tilde{a}$ and the attenuation of the bias line Q.

The local temperature would therefore also increase for higher pump-tone strengths. This would lead to an additional reduction of the accessible bias rates towards larger pump voltages. Moreover, the high amount of saturation from the two pump-tones and the dynamics of the TLS ensemble due to the active bias field makes it difficult to assign a certain temperature to the sample. In the frequency regime of f_{p1}, f_{p2} and f_{res} the ensemble can therefore appear locally hotter due to the additional saturation as in figure 4.7. To fully understand the dynamic behaviour of the individual systems and the entire ensemble it would be important to perform a full analysis with the systems' Hamiltonian. The Monte Carlo simulation at hand is just a proof of principle that this effect can be described by the simple assumptions from section 4.6.1 above.
The dependence on temperature, as already shown in the experimental investigation of the parameter space of figure 4.22, is a direct result of the thermal saturation factor and the lower limit $\dot{F}_{\mathrm{b,min}}$. The thermal saturation thereby decreases the total contribution and the lower limit is increased due to the dependence of the relaxation rate on temperature. Hence the contribution of the lower bias rates are reduced first and the effective area is shifted to higher values of the pump-tone strength. Figure 4.25 shows this behaviour for the different temperatures. The individual plots thereby use a local temperature T_{loc} to account for the decoupling of temperature and the effective heating of the pump-tones at lowest temperatures. All other parameters were kept constant for the simulation of the data in figure 4.25 as depicted in table 4.2. The minimal relaxation time scale $\tau_{1,\mathrm{min}}$ was set to 1 µs, which is a value comparable to the observations in [Kha14, Ros16] for a Si_3N_4 film type setup. The simulation thereby describes the overall behaviour of the obtained area for the emission limit well but for higher temperatures the calculated area deviates from the experimental values. This discrepancy can have different causes. The simulation assumes full contribution of the systems, if the corresponding limits are fulfilled, but for a continuous AC-bias field the individual systems additionally accumulate a phase factor. This leads to constructive or destructive interference of different Landau-Zener transitions [She10, Iva22]. The resulting restraint would affect the contributions of the individual systems and only a sub-ensemble of TLSs takes part in the effect. This aspect will be covered in the following section in more detail.
Furthermore, the pumps are presumably not equally strong due to the different transmission of the cables for the various frequencies similar to the transmission measurement in figure 3.11. For larger detuning $\delta\omega$ this issue would have an even bigger effect. This would hence influence the strength of the generated bias field in dependence of the applied detuning. The transmission for lower frequencies would also require different values for the offset parameter $\tilde{a}$ as already mentioned for the non-linearity measurements of section 4.5. The offset parameter $\tilde{a}$ is therefore also dependent on the detuning $\delta\omega$. The parameters $\tilde{a}$ and Q can consequently only be

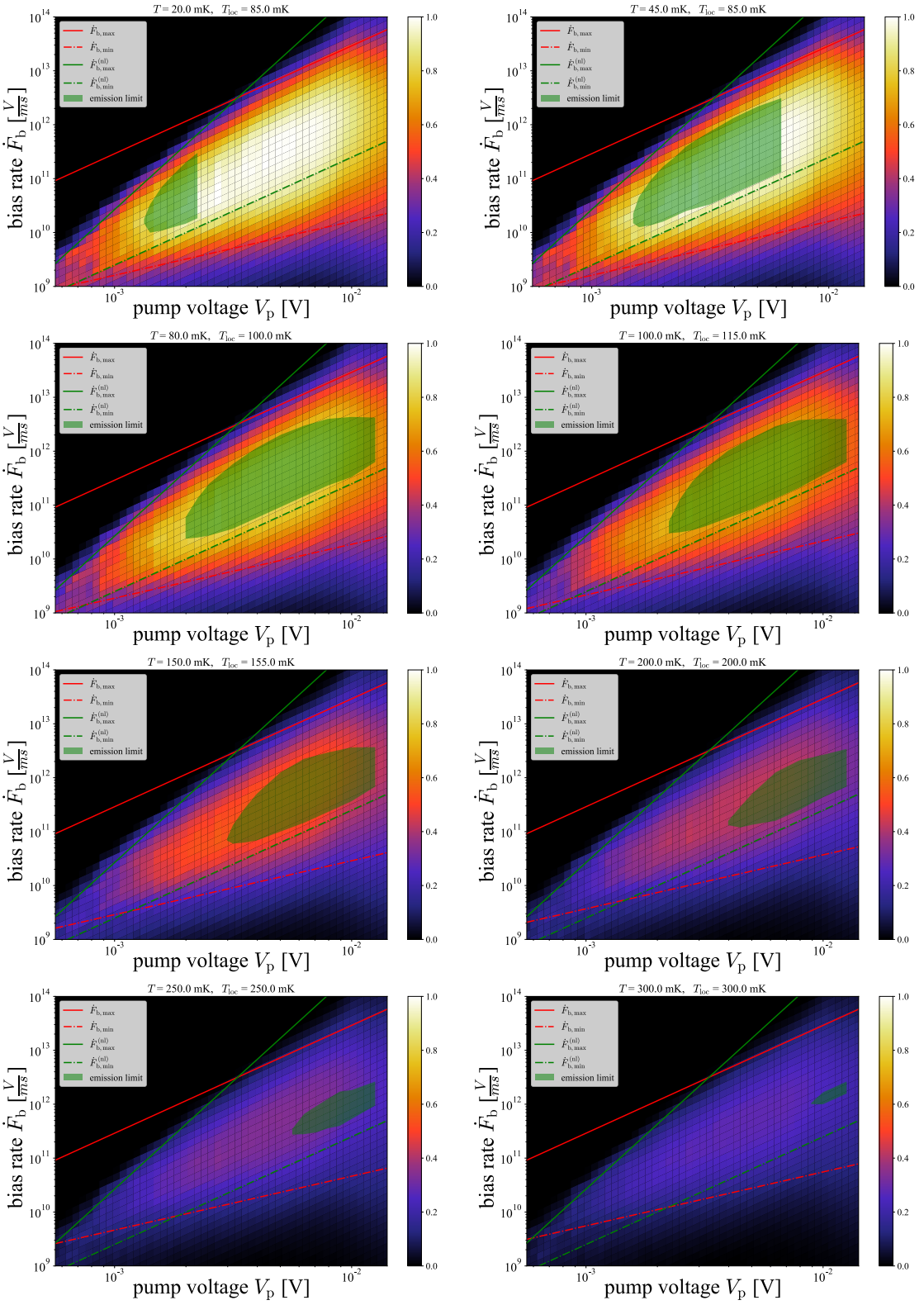

Figure 4.25: Illustration of the results from the Monte Carlo simulation for temperatures between 20 mK and 300 mK. The corresponding parameters are shown in table 4.2.

understood as an averaged approximation for the examined system. The simulation also neglects the influence of a possible heating effect due to the strong pump fields as already mentioned above. This comparatively simple extension could easily be realized by a dependence of the local temperature on the pump voltage V_p but was left out for simplicity. The additional thermal saturation for large pump powers would additionally restrict the total contribution in dependence of V_p.
Overall, this simulation approach used rather simple assumptions to describe the experimental observations in the context of a self biased stimulated emission effect on an amorphous material. The resulting theoretical model is in good agreement with the data and the corresponding parameters are in the expected order of magnitude for the present system. This suggests that the assumption of a self biasing effect with the consequential occurrence of stimulation emission is a justified approach for the description of the additional peak.

Emission limit with coherent transition boundaries

So far, the description of the emission limit assumed TLSs in the single passage limit, in which a system carries the photon energy of the pump to the frequency window of the resonator. For a continuous biasing, as for the suggested self-biasing effect, this is not the full picture for the corresponding ensemble, since phases are important to consider especially when the biasing rate exceeds the relaxation rate as described in section 2.5.4. In this case only certain systems fulfil the resonance condition, while the other systems can not contribute due to the destructive interference.
The obtained data is therefore compared with the derived critical bias limits ξ_1, ξ_2 and ξ_3. The corresponding bias rate dependencies (blue lines) are shown in figure 4.26 together with the area of the emission limit (green) for a temperature of 65 mK. The parameters from table 4.2 remained unchanged with the additional value of $\tau_2 = 1\,\mu\mathrm{s}$. The emission limit is in good agreement with the critical limits and falls into the coherent regime.
In this picture the emission limit could be understood as the first order ($k = 1$) photon resonance with a bias frequency of $f_\mathrm{b} = \delta\omega$. This would mean that not the difference frequency Δf is the relevant quantity for biasing, but rather $\frac{\Delta f}{2}$, which corresponds to the detuning $\delta\omega$ for the symmetric pump arrangement. All bias rates for the emission limit in figure 4.26 were therefore calculated using $f_\mathrm{b} = \frac{\Delta f}{2}$. This coincides with the experimental observations that the emission limit could be induced for the symmetric pump arrangement by a weak signal at resonance frequency for example by the NWA-scan. This would create the right bias frequency ($|f_\mathrm{res} - f_\mathrm{p1}| = |f_\mathrm{res} - f_\mathrm{p2}| = \delta\omega$) from the intermodulation of the individual pumps, to generate the k-photon resonance ($k = 1$) and hence excited TLSs in the frequency window of the resonator. If this excitation is then converted into an emission, the effect

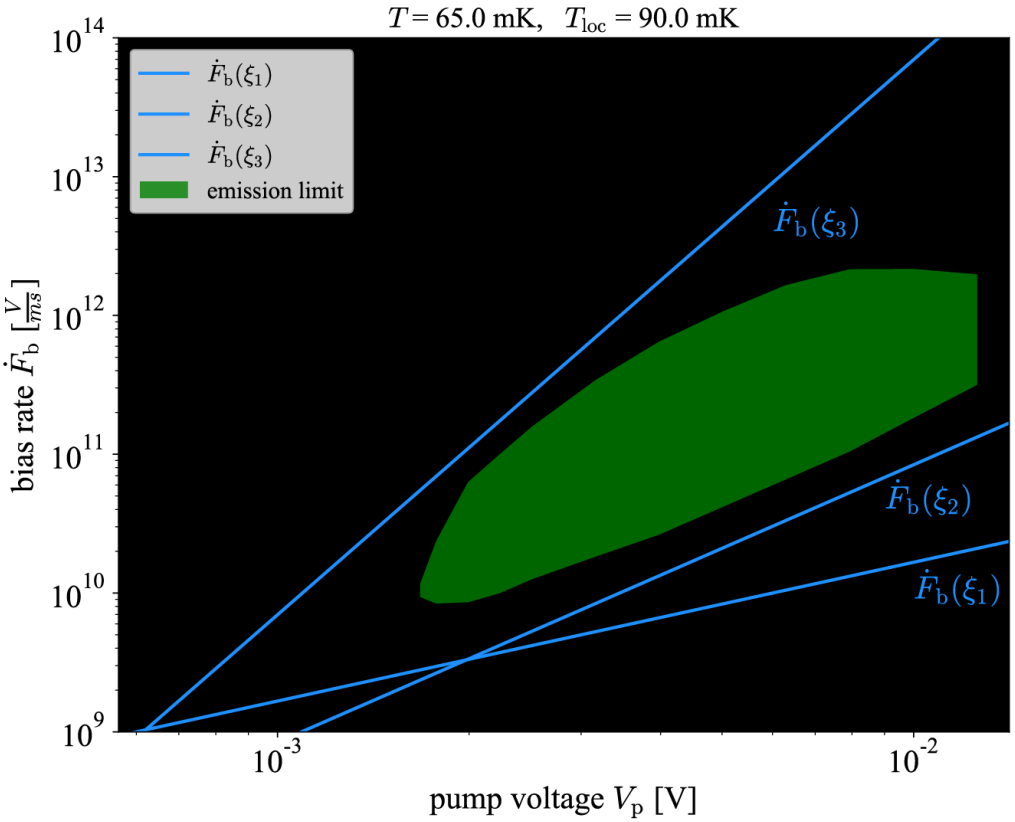

Figure 4.26: Comparison between the critical bias limits ξ_1, ξ_2 and ξ_3 for continuous biasing and the experimentally obtained data for the emission limit at 65 mK.

would also be self-sustaining since the corresponding frequency at f_{res} can generate the matching bias signal according to $f_{\mathrm{b}} = |f_{\mathrm{res}} - f_{\mathrm{p1}}| = |f_{\mathrm{res}} - f_{\mathrm{p2}}|$. This treatment therefore suggests that the emission limit is only achievable in the coherent regime when $1/f_{\mathrm{b}} \gg \tau_1$ holds. A detailed simulation of the emission limit map for this scenario would require the full evaluation of the TLS-Hamiltonian for the entire ensemble and also each pump configuration. The evaluation within this thesis was therefore restricted to the ensemble contributions in the single sweep limit, which was sufficient to describe the boundaries of the observed limit and showed similar results as the continuous treatment.

5. Summary

Within the thesis at hand, dielectric measurements on an ensemble of two-level systems were performed at low temperatures. This included the application of two pump-tones, which revealed an unexpected behaviour of the dielectric loss and the appearance of an emission peak within a specific set of parameters. The response of the resonator could thereby be attributed to a set of equations characteristic for a Duffing oscillator and the boundaries of the novel limit were described by theoretical conditions following the Landau-Zener dynamics for the corresponding systems. These observations are therefore a further addition to the bigger picture in understanding the occurring properties, when TLSs are present in an experimental setup.

The measurements were conducted in a ^{3}He/^{4}He dilution refrigerator on a newly developed LC-resonator design between 20 mK and 6.5 K. The Wheatstone-bridge-like arrangement of the capacitors thereby created an additional electrical branch, which could be used to apply excitation fields onto the sample without interfering with the readout chain of the experiment. Each individual capacitance was realized as a plate capacitor to achieve an homogeneous field distribution and higher field strengths due to the 200 nm thin film separating the plates. With this design a sample variation could easily be achieved depending on the possible materials, which can be sputter deposited in the cleanroom. Furthermore, the experimental setup was improved by installing a HEMT-amplifier at the 4K-stage of the cryostat. This created the foundation to perform measurements at low temperatures with an improved signal to noise ratio.
First measurements on this device were dedicated to ensure a sufficient thermalisation of the microstructured sample material. It showed an almost instant adaptation to a temperature change of the cryostat, which is why the thermalisation time could be approximated to be much shorter than the 15 min measurement time of a single data point. This excluded issues in the following experiments regarding a possible poor thermal coupling of the sample to the experimental platform or an intrinsic heat leak.
The saturation measurement, which is usually performed in order to ascertain the low-power limit, showed an unexpected behaviour indicating a non-linear characteristic resulting in a deviation from the predicted F_{ac}^{-1}-dependency. For temperatures below 150 mK the measurements display a critical phenomenon with a sudden decrease in the dielectric loss by more than one order of magnitude. This behaviour could not be explained by the usual description but instead points towards a collec-

tive or correlated dynamic of the TLSs, which reduces the dielectric loss drastically, comparable to a spontaneous synchronisation effect.
The temperature dependency of the sample, on the other hand, showed the characteristic behaviour of an amorphous material at low temperatures. Thereby, the real part agreed well with the prediction of the standard tunneling model including dipole-dipole interactions of individual systems. The loss deviated especially for low temperatures, but this effect could be attributed to a slight saturation of the TLS-ensemble by the probe-tone. This resulted from the high coupling quality factor of the resonator, which was intended by design but made measurements at very small probe fields difficult. In a nutshell, the thin film SiO_2 behaved as expected for the temperature dependency of an amorphous sample.
The application of two additional symmetric pump-tones during a temperature dependency measurement showed the expected saturation in the loss but no change in the corresponding real part. This was an important result to exclude trivial heating effects caused by the strong field of the pumps.
The following detuning measurement was dedicated to further investigate the saturation behaviour of the ensemble for different detuning values at a constant temperature. This revealed the enhancement of the observed quality factor for the resonator compared to the simple assumption of two independently burned holes in the distribution function. This enhancement seemed to grow with increasing field strength of the pumps and resulted in the occurrence of a new limit, in which the resonator started to emit at the intermediate frequency.
The transition to this limit was investigated by a measurement technique with asymmetric pump-tone arrangement. The corresponding response of the resonator showed the characteristic features of a non-linear Duffing-type oscillator driven by an additional strong field. If this field was attributed to the occurring emission peak, the behaviour of the resonator setup agreed well with the derived equations for the Duffing oscillator. This included the description of the emission amplitude in dependence on the intermediate frequency of the pumps. The observed response of the device could therefore be well described, but the underlying mechanism for the occurrence of the emission peak was still missing.
This gave rise to a further investigation of the non-linear characteristics of the device and revealed the appearance of the intermediate frequency of the pumps in the MHz-regime. For an adequate field strength this frequency can function as the bias signal for the TLS-ensemble. The appearance of a bias field could hereby also explain the enhanced quality factor for the detuning measurements since a modulation of the TLSs energy splitting could widen the *burned holes* of the individual pumps. The corresponding effect was hence referenced as self-biasing. Moreover, previous numerical simulations [Mün21] showed that these intermodulation frequencies can be caused by the non-linear properties of the TLSs themselves.

Furthermore, the emission limit was only observed in a specific set of parameters mainly dependent on the detuning and the field strength of the pump-tones, but also on the temperature of the cryostat. The boundaries of the effect were therefore determined for different temperatures and compared to simple theoretical limits from the Landau-Zener description [Ros16] of a single sweep. They were complemented by introducing an additional boundary, which included the necessary minimal modulation for a single TLS to contribute to the emission in the resonator. A simple Monte-Carlo simulation including these boundaries was therefore performed to add up the individual contributions of the ensemble to a total value for a potential emission effect. This description already showed good agreement with the measured data, even though it did not include the effect of continuous biasing. This can be understood since the corresponding description, including the phase of the individual systems, yields similar limits for the contributions. However, the associated picture is different since the emission limit can then be interpreted as the k-photon ($k = 1$) resonance of each pump-tone with a bias frequency of $f_\mathrm{b} = \frac{1}{2}|f_\mathrm{p1} - f_\mathrm{p2}|$. The corresponding frequency was also observed in the MHz-regime for the non-linearity measurements. Assuming this formalism, the observed emission would arise in the coherent regime, for which the bias rate exceeds the relaxation time scale. To describe this scenario in more detail similar to the Monte-Carlo approach, a full time evolution for the individual TLSs Hamiltonians of the ensemble would be necessary for each set of experimental parameters. This was not part of the work within this thesis but would be an interesting addition in the understanding of the observed effect.

To summarize, the field of low temperature physics repeatedly offers new insights in complex many-body systems. Especially simulation approaches are thereby increasingly important to understand the connections related thereto. Previous works on this topic within our group [Fre21, Mün21, Din22, Bli22] contributed significantly to the understanding of the observed properties of the setup. The hereby occurring emission effect is an interesting feature, which can be explained in the context of the two-level system description. This makes it a possible approach for further investigations techniques.

Bibliography

[And72] P. W. Anderson, B. I. Halperin, and C. Varma, Anomalous low-temperature thermal properties of glasses and spin glasses, *Philosophical Magazine*, **25**(1), 1–9, 1972.

[Ang07] D. V. Anghel, T. Kühn, Y. M. Galperin, and M. Manninen, Interaction of two-level systems in amorphous materials with arbitrary phonon fields, *Phys. Rev. B*, **75**(064202), 2007.

[Arn75] W. Arnold and S. Hunklinger, Experimental evidence for the direct interaction between two-level systems in glasses at very low temperatures, *Sol. St. Comm.*, **17**, 883–886, 1975.

[Arn78] W. Arnold, C. Martinon, and S. Hunklinger, Direct experimental observation of spectral diffusion in vitreous silica at low temperatures, *J. Physique Coll.*, **39**(C6), 961–962, 1978.

[Ash09] S. Ashhab, J. R. Johansson, A. M. Zagoskin, and F. Nori, Single-artificial-atom lasing using a voltage-biased superconducting charge qubit, *New J. Phys.*, **11**(023030), 2009.

[Ast07] O. Astafiev, K. Inomata, A. O. Niskanen, T. Yamamoto, Y. A. Pashkin, Y. Nakamura, and J. S. Tsai, Single artificial-atom lasing, *Nature*, **449**, 588590, 2007.

[Bal96] N. H. Balshaw, Practical Cryogenics, Oxford Instruments, 3rd edition, 1996.

[Bar13] M. Bartkowiak, M. Bazrafshan, C. Fischer, A. Fleischmann, and C. Enss, Novel isotope effects observed in polarization echo experiments in glasses,, *Phys. Rev. Lett.*, **110**, 205502, 2013.

[Baz08] M. Bazrafshan, Investigation of the microscopic nature of tunnelling systems in amorphous glycerol by two-pulse polarisation echo experiments, PhD Thesis, university Heidelberg, 2008.

[Bla77] J. L. Black and B. I. Halperin, Spectral diffusion, phonon echoes, and saturation recovery in glasses at low temperatures, *Phys. Rev. B*, **16**(6), 2879–2895, 1977.

[Bli22] J. Blickberndt, The Influence of Continuous Electric Bias Fields on the Dielectric Loss of Atomic Tunneling Systems, Master Thesis, university Heidelberg, 2022.

[Blo46] F. Bloch, Nuclear induction, *Phys. Rev.*, **70**(7), 460–474, 1946.

[Boy20] R. W. Boyd, Nonlinar Optics, Academic Press, 4th edition, 2020.

[Bre17] J. D. Brehm, A. Bilmes, G. Weiss, A. V. Ustinov, and J. Lisenfeld, Transmission-line resonators for the study of individual two-level tunneling systems, *Appl Phys. Lett*, **111**(112601), 1–4, 2017.

[Bri26] L. Brillouin, La mécanique ondulatoire de Schrödinger: une méthode générale de resolution par approximations successives, *Compt. Rend.*, **183**, 24–26, 1926.

[Bur95] A. L. Burin, Dipole gap effects in low energy excitation spectrum of amorphous solids. Theory for dielectric relaxation, *J. Low Temp. Phys.*, **100**(3), 309–337, 1995.

[Bur98] A. L. Burin, D. Natelson, D. D. Osheroff, and Y. Kagan, Interactions between tunneling defects in amorphous solids, Volume 1 in *Tunneling Systems in Amorphous and Crystalline Solids*, Springer, 1998.

[Bur14a] A. L. Burin, A. O. Maksymov, and K. D. Osborn, Quantum coherent manipulation of two-level systems in superconducting circuits, *Supercond. Sci. Technol.*, **24**(8), 2014.

[Bur14b] J. Burnett, L. Faoro, I. Wisby, V. L. Gurtovoi, A. V. Chernykh, G. M. Mikhailov, V. A. Tulin, R. Shaikhaidarov, V. Antonov, P. J. Meeson, A. Y. Tzalenchuk, and T. Lindström, Evidence for interacting two-level systems from the 1/f noise of a superconducting resonator, *Nat. Comm.*, **5**(4119), 2014.

[Bur18] A. L. Burin and A. O. Maksymov, Theory of nonlinear microwave absorption by interacting two-level systems, *Phys. Rev. B*, **97**(214208), 2018.

[Cap20] T. Capelle, E. Flurin, E. Ivanov, J. Palomo, M. Rosticher, S. Chua, T. Briant, P. Cohadon, A. H. T. Jacqmin, and S. Deléglise, Probing a two-level system bath via the frequency shift of an off-resonantly driven cavity, *Phys. Rev. App.*, **13**(034022), 2020.

[Car94] H. M. Carruzzo, Nonequilibrium dielectric behavior in glasses at low temperatures: Evidence for interacting defects, *Phys. Rev. B*, **50**(10), 6685–6695, 1994.

[Che14] F. Chen, J. Li, A. D. Armour, E. Brahimi, J. Stettenheim, A. J. Sirois, R. W. Simmonds, M. P. Blencowe, and A. J. Rimberg, Realization of a single-cooper-pair josephson laser, *Phys. Rev. B*, **90**(020506), 2014.

[Deb12] P. Debye, Zur Theorie der spezifischen Wärmen, *Ann. Phys*, **344**(12), 789–839, 1912.

[Deb13] P. Debye, On the theory of anomalous dispersion in the region of long-wave electromagnetic radiation, *Verh. Deut. Phys. Gesell.*, **15**, 777–793, 1913.

[Din22] M. Dinger, Three-Tone Spectroscopy of Non-linear Two-Level Atomic Tunnelling Systems in Non-Equilibrium, Master Thesis, university Heidelberg, 2022.

[Dir27] P. A. M. Dirac, The quantum theory of the emission and absorption of radiation, *Proc. R. Soc. Lond. A*, **114**(767), 1927.

[Dou80] P. Doussineau, C. Frnois, R. G. Leisure, A. Levelut, and J.-Y. Prieur, Amorphous-like acoustical properties of Na doped $\beta - Al_2O_3$, *J. Physique*, **41**(10), 1193–1211, 1980.

[Duf18] G. Duffing, Erzwungene Schwingungen bei veränderlicher Eigenfrequenz und ihre technische Bedeutung, *Sammlung Vieweg*, **41/42**, 1918.

[Ens89] C. Enss, C. Bechinger, and M. von Schickfus, Dynamics of tunneling states in borosilicate glass, *Phonons 89*, 474–479, 1989.

[Ens97] C. Enss and S. Hunklinger, Incoherent tunneling in glasses at very low temperatures, *Phys. Rev. Lett.*, **79**(15), 2831–2834, 1997.

[Ens05] C. Enss and S. Hunklinger, Low-Temperature Physics, Springer, 2005.

[Esq98] P. Esquinazi, Tunneling Systems in Amorphous and Crystalline Solids, Springer, 1998.

[Fre16] B. Frey, Entwicklung mikrostrukturierter supraleitender Resonatoren zur breitbandigen Untersuchung dielektrischer Eigenschaften zwischen 37MHz und 1 GHz bei tiefen Temperaturen, Master Thesis, university Heidelberg, 2016.

[Fre17] H. Freund, Controlling silica in its crystalline and amorphous states: a problem in surface science, *Acc. Chem. Res.*, **50**(3), 446–449, 2017.

[Fre21] B. Frey, Landau-Zener spectroscopy of bulk glasses, PhD Thesis, university Heidelberg, 2021.

[Fri44] H. T. Friis, Noise figures of radio receivers, *Proc. of the IRE*, **32**(7), 419–422, 1944.

[Fro92] G. Frosatti, Experimental techniques: Methods for cooling below 300 mK, *J. Low Temp. Phys.*, **87**(3-4), 595–633, 1992.

[Gao07] J. Gaoa, J. Zmuidzinas, B. A. Mazin, H. G. LeDuc, and P. K. Day, Noise properties of superconducting coplanar waveguide microwave resonators, *App. Phys. Lett.*, **90**(102507), 2007.

[Gol73] B. Golding, J. E. Graebner, B. I. Halperin, and R. J. Schutz, Nonlinear phonon propagation in fused silica below 1 K, *Phys. Rev. Lett.*, **30**(6), 223–227, 1973.

[Guc86] J. Guckenheimer and P. J. Holmes, Nonlinear oscillations, dynamical systems, and bifurcations of vector fields, Springer, 2nd edition, 1986.

[Hau08] J. Hauss, A. Fedorov, C. Hutter, A. Shnirman, and G. Schön, Single-qubit lasing and cooling at the rabi frequency, *Phys. Rev. Lett.*, **100**(037003), 2008.

[Hua12] P. Y. Huang, S. Kurasch, A. Srivastava, V. Skakalova, J. Kotakoski, A. V. Krasheninnikov, R. Hovden, Q. Mao, J. C. Meyer, J. Smet, D. A. Muller, and U. Kaiser, Direct imaging of a two-dimensional silica glass on graphene, *Nano Lett.*, **12**(2), 1081–1086, 2012.

[Hun72] S. Hunklinger, W. Arnold, S. Stein, R. Nava, and K.Dransfeld, Saturation of the ultrasonic absorption in vitreous silica at low temperatures, *Physics Letters A*, **42**(3), 253–255, 1972.

[Hun73] S. Hunklinger, W. Arnold, and S. Stein, Anomalous ultrasonic attenuation in vitreous silica at low temperatures, *Physics Letters A*, **45**(4), 311–312, 1973.

[Hun76] S. Hunklinger and W. Arnold, Chapter 3: Ultrasonic Properties of Glasses at Low Temperatures, Volume 12 in *Phys. Acoust.*, Academic Press, 1976.

[Hun82] S. Hunklinger, Phonons in amorphous materials, *J. Physique*, **43**(12), 461–474, 1982.

[Hun22] C. Hung, L. Y. N. Foroozani, S. Fritz, D. Gerthsen, and K. D. Osborn, Probing hundreds of individual quantum defects in polycrystalline and amorphous alumina, *Phys. Rev. Applied*, **17**(034025), 2022.

[Iva22] O. V. Ivakhnenko, S. N. Shevchenko, and F. Nori, Nonadiabatic Landau-Zener-Stückelberg-Majorana transitions, dynamics, and interference, *arXiv*, (2203.16348), 1–100, 2022.

[Jäc72] J. Jäckle, On the ultrasonic attenuation in glasses at low temperatures, *Z. Phys. A*, **257**(3), 1972.

[Jor07] D. W. Jordan and P. Smith, Nonlinear Ordinary Differential Equations, Oxford University Press, 4th edition, 2007.

[Kar83] V. G. Karpov, M. I. Klinger, and F. N. Ignat'ev, Theory of the low-temperature anomalies in the thermal properties of amorphous structures, *Sov. Phys. JETP*, **84**, 760–775, 1983.

[Kar87] V. G. Karpov, M. A. Il'in, and D. A. Parshin, Parameters of soft atomic potentials in glasses, *Sov. Phys. JETP*, **92**, 291–296, 1987.

[Kha12] M. S. Khalil, M. J. A. Stoutimore, F. C. Wellstood, and K. D. Osborn, An analysis method for asymmetric resonator transmission applied to superconducting devices, *J. Appl. Phys.*, **111**(5), 16, 2012.

[Kha13] M. S. Khalil, A study of two-level system defects in dielectric films using superconducting resonantors, PhD Thesis, university of Maryland, 2013.

[Kha14] M. S. Khalil, S. Gladchenko, M. J. A. Stoutimore, F. C. Wellstood, A. L. Burin, and K. D. Osborn, Landau-Zener population control and dipole measurement of a two-level-system bath, *Phys. Rev. B*, **90**(100201), 2014.

[Kir17] N. Kirsh, E. Svetitsky, A. Burin, M. Schechter, and N. Katz, Revealing the nonlinear response of a tunneling two-level system ensemble using coupled modes, *Phys. Rev. Mat.*, **1**(012601(R)), 2017.

[Kla62] J. R. Klauder and P. W. Anderson, Spectral diffusion decay in spin resonance experiments, *Phys. Rev.*, **125**(3), 912–932, 1962.

[Kra26] H. A. Kramers, Wellenmechanik und halbzahlige Quantisierung, *Z. Phys.*, **39**, 828–840, 1926.

[Kri19] S. Krinner, S.Storz, P. Kurpiers, P. Magnard, J. Heinsoo, R. Keller, J. Lütolf, C. Eichler, and A. Wallraf, Engineering cryogenic setups for 100-qubit scale superconducting circuit systems, *EPJ Quantum Technol.*, **6**(2), 1–29, 2019.

[Ku05] L.-C. Ku and C. C. Yu, Decoherence of a josephson qubit due to coupling to two-level systems, *Phys. Rev. B*, **72**(024526), 2005.

[Laf15] B. Lafuente, R. T. Downs, H. Yang, and N. Stone, The power of databases: the RRUFF project, Volume 1 in *Highlights in Mineralogical Crystallography*, De Gruyter, 2015.

[Lan32] L. Landau, On the theory of transfer of energy at collisions II, *Phys. Z. Sowjetunion*, **2**(46), 1932.

[Las75] J. C. Lasjaunias, A. Ravex, M. Vandorpe, and S. Hunklinger, The density of low energy states in vitreous silica: specific heat and thermal conductivity down to 25 mK, *Solid State Commun.*, **17**(9), 10451049, 1975.

[Lic12] L. Lichtenstein, M. Heyde, and H. J. Freund, Atomic arrangement in two-dimensional silica: From crystalline to vitreous structures, *J. Phys. Chem. C*, **16**(38), 2042620432, 2012.

[Lis15] J. Lisenfeld, G. J. Grabovskij, C. Müller, J. H. Cole, G. Weiss, and A. V. Ustinov, Observation of directly interacting coherent two-level systems in an amorphous material, *Nat. Comm.*, **6**, 2015.

[Lis19] J. Lisenfeld, A. Bilmes, A. Megrant, R. Barends, J. Kelly, P. Klimov, G. Weiss, J. M. Martinis, and A. V. Ustinov, Electric field spectroscopy of material defects in transmon qubits, *Npj Quantum Inf.*, **5**(105), 2019.

[Low13] Low Noise Factory, Data sheet, LNF-LNC1 12A s/n 313B 1-12 GHz Cryogenic Low Noise Amplifier, 2013.

[Lud02] S. Ludwig, C. Enss, P. Strehlow, and S. Hunklinger, Direct coupling of magnetic fields to tunneling systems in glasses, *Phys. Rev. Lett.*, **88**(7), 075501, 2002.

[Lud03] S. Ludwig, P. Nagel, S. Hunklinger, and C. Enss, Magnetic field dependent coherent polarization echoes in glasses, *J. Low Temp. Phys.*, **131**(1/2), 89–111, 2003.

[Mai16] S. Maier, B. A. J. Lechner, G. A. Somorjai, and M. Salmeron, Growth and structure of the first layers of ice on Ru(0001) and Pt(111), *J. Am. Chem. Soc.*, **138**(9), 31453151, 2016.

[Mar05] J. M. Martinis, K. B. Cooper, R. McDermott, M. Steffen, M. Ansmann, K. D. Osborn, K. Cicak, S. Oh, D. P. Pappas, R. W. Simmonds, and C. C. Yu, Decoherence in josephson qubits from dielectric loss, *Phys. Rev. Lett.*, **95**(210503), 2005.

[Mat63] B. T. Matthias, T. H. Geballe, and V. B. Compton, Superconductivity, *Rev. Mod. Phys.*, (35), 1–22, 1963.

[Mat19] S. Matityahu, H. Schmidt, A. Bilmes, A. Shnirman, G. Weiss, A. V. Ustinov, M. Schechter, and J. Lisenfeld, Dynamical decoupling of quantum two-level systems by coherent multiple Landau-Zener transitions, *npj Quantum Inf.*, **5**(114), 2019.

[McR20] C. McRae, H. Wang, J. Gao, M. Vissers, T. Brecht, A. Dunsworth, D. Pappas, and J. Mutus, Materials loss measurements using superconducting microwave resonators, *arXiv*, (2006.04718v2), 1–23, 2020.

[Mül19] C. Müller, J. H. Cole, and J. Lisenfeld, Towards understanding two-level-systems in amorphous solids - insights from quantum circuits, *Rep. Prog. Phys.*, **82**(124501), 2019.

[Mün21] L. Münch, Simulations of the Non-linear Behavior of Two-Level Atomic Tunneling Systems, Master Thesis, university Heidelberg, 2021.

[Nag04] P. Nagel, A. Fleischmann, S. Hunklinger, and C. Enss, Novel isotope effects observed in polarization echo experiments in glasses, *Phys. Rev. Lett.*, **92**(24), 245511, 2004.

[Nat17] P. Natzkin, Superconducting Microwave Resonator Designs for Electron Spin Resonance Applications, Master Thesis, TU München, 2017.

[Nay95] A. H. Nayfeh and D. T. Mook, Nonlinear Oscillations, Wiley Classics Library, 1st edition, 1995.

[Nei13] C. Neill, A. Megrant, R. Barends, Y. Chen, B. Chiaro, J. Kelly, J. Y. Mutus, P. J. J. OMalley, D. Sank, J. Wenner, T. C. White, Y. Yin, A. N. Cleland, and J. M. Martinis, Fluctuations from edge defects in superconducting resonators, *App. Phys. Lett.*, **103**(072601), 2013.

[Nol13] W. Nolting, Grundkurs Theoretische Physik 5/1, Springer, 8. Auflage, 2013.

[Pal14] E. Paladino, Y. M. Galperin, G. Falci, and B. L. Altshuler, $1/f$ noise: Implications for solid-state quantum information, *Rev. Mod. Phys.*, **86**, 361–418, 2014.

[Par93] D. A. Parshin, Soft potential model and universal properties of glasses, *Phys. Scr.*, **T49**, 180–185, 1993.

[Pea06] V. Peano and M.Thorwart, Dynamics of the quantum duffing oscillator in the driving induced bistable regime, *Chem. Phys.*, **322**, 135–143, 2006.

[Phi72] W. A. Phillips, Tunneling states in amorphous solids, *Journal of Low Temperature Physics*, **7**(3/4), 351–360, 1972.

[Phi81] W. A. Philips, Amorphous solids - 1. Introduction, Volume 24 in *Topics in current physics*, Springer, 1981.

[Phi87] W. A. Phillips, Two-level states in glasses, *Rep. Prog. Phys*, **50**, 1657–1708, 1987.

[Pob07] F. Pobell, Matter and methods at low temperatures, Springer, 3rd edition, 2007.

[Pri93] J. Y. Prieur, R. Höhler, J. Joffin, and M. Devaud, Sound amplification by stimulated emission of radiation in an amorphous compound, *Europhys. Lett.*, **24**(5), 1993.

[Pro15] S. Probst, F. B. Song, P. A. Bushev, A. V. Ustinov, and M. Weides, Efficient and robust analysis of complex scattering data under noise in microwave resonators, *Rev. Sci. Instrum*, **86**(2), 17, 2015.

[Rei17] A. Reifenberger, Spezifische Wärme von supraleitenden metallischen Gläsern bei tiefen Temperaturen, PhD Thesis, university Heidelberg, 2017.

[Ros16] Y. J. Rosen, M. S. Khalil, A. L. Burin, and K. D. Osborn, Random-defect laser: Manipulating lossy two-level systems to produce a circuit with coherent gain, *Phys. Rev. Lett.*, **116**(163601), 2016.

[Sar16] B. Sarabi, A. N. Ramanayaka, A. L. Burin, F. C. Wellstood, and K. D. Osborn, Projected dipole moments of individual two-level defects extracted using circuit quantum electrodynamics, *Phys. Rev. Lett.*, **116**, 2016.

[Sch18] H. Schmidt, Superconducting Resonators for the Study of Tunneling Systems, Master Thesis, Karlsruhe Institute of Technology, 2018.

[She10] S. N. Shevchenko, S. Ashhab, and F. Nori, Landau-Zener-Stückelberg interferometry, *Phys. Rept.*, **492**(1), 2010.

[Son18] Sonnet Software, Inc., 126 N. Salina St., Syracuse, NY 13202, Sonnet Users Guide, 2018.

[Str98] P. Strehlow, C. Enss, and S. Hunklinger, Evidence for a phase transition in glasses at very low temperature: A macroscopic quantum state of tunneling systems?, *Phys. Rev. Lett.*, **80**(24), 5361–5364, 1998.

[Stü32] E. C. G. Stückelberg, Theory of inelastic collisions between atoms, *Helvetica Physica Acta*, **5**, 369–423, 1932.

[Vog92] W. Vogel, Glaschemie, Springer, 3rd edition, 1992.

[vS77] M. von Schickfus and S. Hunklinger, Saturation of the dielectric absorption of vitreous silica at low temperatures, *Physics Letters A*, **64**(1), 144–146, 1977.

[War33] B. E. Warren, X-ray diffraction of vitreous silica, *Z. Krist.*, **86**(1-6), 349–358, 1933.

[War34] B. E. Warren, The diffraction of x-rays in glass, *Phys. Rev.*, **45**(10), 657–661, 1934.

[Wen26] G. Wentzel, Eine Verallgemeinerung der Quantenbedingungen für die Zwecke der Wellenmechanik, *Z. Phys.*, **38**, 518–529, 1926.

[Woh01] M. Wohlfahrt, Untersuchung der dielektrischen Tieftemperaturanomalien von Mehrkomponentengläsern in Magnetfeldern, PhD Thesis, university Heidelberg, 2001.

[Wür02] A. Würger, A. Fleischmann, and C. Enss, Dephasing of atomic tunneling by nuclear quadrupoles, *Phys. Rev. Lett.*, **89**(23), 237601, 2002.

[Yan11] F. Yang, Y. Choi, P. Liu, D. S. J. Hrbek, and J. A. Rodriguez, Identification of 57 defects in a copper oxide surface, *J. Am. Chem. Soc.*, **133**(30), 11474–11477, 2011.

[Zac32] W. H. Zachariasen, The atomic arrangement in glass, *J. Am. Chem. Soc.*, **54**(10), 38413851, 1932.

[Zel71] R. C. Zeller and R. Pohl, Thermal conductivity and specific heat of noncrystaline solids, *Physical Review B*, **4**(6), 2029–2041, 1971.

[Zen32] C. Zener and R. H. Fowler, Non-adiabatic crossing of energy levels, *Proc. R. Soc. London*, **137**(833), 696–702, 1932.

[Zer27] F. Zernike and J. A. Prins, Die Beugung von Röntgenstrahlen in Flüssigkeiten als Effekt der Molekülanordnung, *Z. Phys. A*, **41**, 184–194, 1927.

Acknowledgements

Zuletzt wollte ich noch ein paar Worte an die Menschen richten, die ein Gelingen dieser Arbeit überhaupt möglich gemacht haben. Mein Dank gilt dabei besonders:

Prof. Christian Enss für die Möglichkeit an diesem interessanten Thema arbeiten zu dürfen und die gesamte Zeit, die mir immer viel Spaß gemacht hat.

Prof. Heinz Horner für das Interesse an diesem Thema und die Bereitschaft das zweite Gutachten zu schreiben.

Prof. Reiner Dahint und Prof. Martijn Kemerink für das Übernehmen der Rolle als weitere Prüfer.

Der HGSFP für sämtliche organisatorische Unterstützung während meiner Zeit als Doktorand und in der finalen Phase der Arbeit.

Dr. Andreas Reiser für jegliche Unterstützung im Labor und für alle physikalischen Exkurse die über den Tellerand hinaus gingen.

Dr. Andreas Fleischmann für anregende Diskussionen und neue Blickwinkel auf das Thema.

Prof. Sebastian Kempf, Dr. Andreas Reifenberger, Hr. Wolf und dem Reinraumteam für die Fertigung der mikrostrukturierten Resonatoren.

Rudi Eitel für die Versorgung mit Helium während der Experimente und mit Nusszopf in den Kaffeepausen.

Der Elektronik, der Werkstatt und der EDV für die Unterstützung beim Aufbau des Experiments und der Bereitstellung der nötigen Infrastruktur.

Meinen aktuellen und ehemaligen Bürokolleg(inn)en Andreas Schaller, Benedikt Frey, Christian Ständer, Jan Blickberndt und Nathalie Probst für die tolle Zeit zusammen und viele lustige Gespräche.

dabei besonders Andreas Schaller, Benedikt Frey und Christian Ständer für die schöne Zeit in Klosters und ebenso Andreas Reifenberger, Arnulf Barth und Matthew Herbst für die lustige Zeit in Košice.

Außerdem Mareike Dinger für die tolle und bereichernde Zusammenarbeit, Lukas Münch für viele hilfreiche Diskussionen als erweiterter Bürokollege und allen anderen aktuellen und ehemaligen F345lern für die schöne Zeit.

Meiner Familie und meinen Freunden, dabei ganz besonders meinen Eltern und meiner Freundin für die Unterstützung während dieser Zeit.